Time domain THz spectroscopy of semiconductors

Cluff, Julian

Award date:
2000

Awarding institution:
University of Bath

Time Domain THz Spectroscopy of Semiconductors

submitted by Julian Cluff
for the degree of PhD
of the University of Bath
2000 A. D.

ProQuest LLC
789 East Eisenhower Parkway
P.O. Box 1346
Ann Arbor, MI 48106-1346

TO MY FAMILY

Acknowledgements

There are many people I would like to thank in recognition of their help during the writing of this thesis. In particular my supervisor, Dr. Steve Andrews, deserves thanks for his continued guidance and support. For their generous assistance and advice in the laboratory I would like to thank Dr. Peter Huggard, Mr. Christopher Shaw and Mr. Graeme Moore and for their help with my English, Mr. Mark Acres and Dr. Adam Armitage. I would also like to thank my C. A. S. E. supervisor Dr. Don Arnone and the Cambridge Research Laboratory (formerly Toshiba Cambridge Research Centre) for advice and financial support and Dr. David Ritchie and Dr. Edmund Linfield at the Cavendish Laboratory for supplying the MBE structures studied. My family must be thanked for their patience and enthusiasm during my writing up. Certain inmates of the department of physics and the mountaineering and motorcycle fraternities, in particular Gary Dickson, I thank for their continued moral support, if not guidance. Finally Mr P. Pycksi and Mr C. Ylf, without whose help none of the experiments would have been possible.

Julian Cluff (April 2000)

Contents

Abstract

Time Resolved THz Spectroscopy of Semiconductors

A state of the art time domain THz spectrometer has been used to study various aspects of charge transport in semiconductors under moderate magnetic fields and temperatures. The recent realisation of optoelectronic techniques for the generation and detection of sub-picosecond, freely propagating electromagnetic transients has provided access to the THz region of the electromagnetic spectrum which had previously been hampered by the lack of suitable tools.

Throughout the period leading up to this volume (1995-2000) an increase in spectrometer sensitivity of concentrations up to 10^{18} cm^{-3}. Cyclotron absorption measurements in a Si/SiGe quantum well sample display an extended scattering time when compared with transport data and approach a non-zero offset at zero field. More than the classical cyclotron resonance picture is required and the results may be explained in terms of antidot like states. The dual pulse source is additionally used to impulsively drive and coherently control cyclotron oscillations in a two dimensional electron gas (2DEG) by varying two orders of magnitude has been achieved by excitation beam line focusing and polarisation selection and use of SiOSi as a receiver material. In addition the development of a single chip dual pulse source for THz interferometry is described.

The ability of far infrared optical constants to be predicted from transport measurements is investigated by amplitude transmission and THz Hall measurements of GaAs epilayers with carrier the temporal separation between the pulses. This is the first demonstration of the coherent intraband control of electron motion. Finally, the first time domain observation of coherent cold 2DEG plasma oscillations is described together with an unexplained broadening of the cyclotron resonance in magnetoplasmon measurements. Interband excitation displays no signs of screening by the photo-injected carriers.

1 Overview

The field of far-infrared (FIR) spectroscopy has been reinvigorated by the recent development of time domain THz spectroscopy, enabling detailed investigation of phenomena in the THz part of the electromagnetic spectrum which had previously been hampered by the lack of suitable tools. The method builds on Hertz's experiments[1] in which large electric potentials created between the arms of a dipole transmitter ionised the intermediate air allowing a transient electrical current (spark) to pass between the arms (figure 1.1a). The transient current generated ~ 100 MHz bandwidth radio waves which were detected by a similar dipole arrangement several metres away as a spark between two metal points. The modern development of these spark gap transmitters and receivers are microfabricated, dipole antennas bridged by ultrafast photoconducting switches (figure 1.1b) as first developed by Auston *et al.*[2].

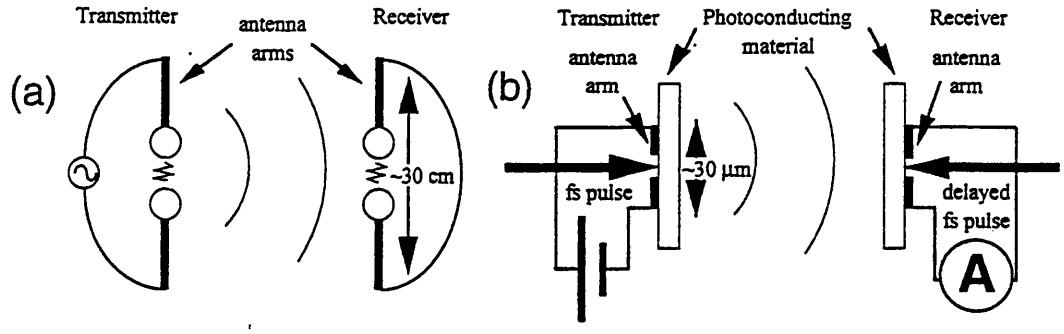

Figure 1.1: (a) Schematic of a spark gap transmitter/receiver combination. The energy to create the spark in the receiver comes from the transmitted electromagnetic pulse. (b) Schematic of an Auston type transmitter and receiver. To obtain high response speeds fast photoconducting switches, illuminated by subpicosecond optical pulses, are used. The transmitter is dc biased and the receiver, which is connected to a low-noise amplifier, receives its bias from the electromagnetic pulse.

This approach offers sub-picosecond time resolution, high spectral brightness in transmission measurements, sensitivity to average powers of order 20 aW, room temperature, background free operation and coherent detection (i.e. measurement of electric field amplitude and phase). The FIR properties of materials as wide ranging as semiconductors[3], dielectrics[3], superconductors[4], liquids and gases[5] have been investigated by time domain THz spectroscopy. Recent applications have been to the study of coherent wavepacket dynamics in atoms and condensed matter[6], phonons[7], plasmons[8], cyclotron resonance (CR)[9], THz Hall measurements[10], scattering problems e.g. scale pulsed radar simulations[11], intermolecular interactions[12], plasma diagnostics[13], FIR imaging[14] and tomography[15].

Conventional FIR spectroscopy based on thermal sources such as glow bars and mercury arc lamps is hampered by a lack of spectral brightness and time resolution. FIR lasers are generally restricted to discrete frequencies, are of limited brightness and not developed as ultrafast sources. Two colour photomixing of lasers in nonlinear crystals can produce THz frequency radiation with a higher degree of tunability, e.g. 0.2-2.5 THz[16] but also does not offer the sophisticated pulse capabilities available in the near infrared. Swept frequency synthesisers, e.g. frequency tripled Gunn diodes are limited to below a few hundred GHz[17], with higher frequencies only available using discrete frequency sources. Tuneable FIR lasers based on cyclotron emission from cryogenically cooled p-type germanium cover part of the THz spectrum but are very difficult to make and use[18]. Whilst all these sources have provided a wealth of information regarding the steady-state behaviour of the aforementioned phenomena, their temporal resolution has been limited at best to the nanosecond range. The free electron laser is a notable exception to some of these constraints, generating high power, tuneable, picosecond THz pulses, but is large, expensive and only available at special facilities. With the exception of electronic sources, the associated detectors such as bolometers, are incoherent, i.e. they measure power as opposed to electric field.

The development of ultrafast millimetre and sub-millimetre wave measurements began in 1981, with the realisation of photoconductive materials with

sub-picosecond carrier recombination times[19]. This lead to the construction of photoconductive devices with switching speeds of a few picoseconds[20] together with microstriplines to carry the signals[21]. From the beginning, ultrafast lasers were necessary to activate and probe these devices as their speed outstripped the capabilities of most conventional electronic characterisation methods. The research in this area was motivated by its potential as a tool for physical studies as well as applications in the areas of ultrafast semiconductor devices and telecommunications. Subsequent research concentrated on the development and studies of the intrinsic physics of the building blocks of THz frequency systems such as switches, microstriplines and antennas[22,23,24]. Picosecond electrical pulses are commonly used to probe fast electrical circuits[25] but their propagation on the interconnects leads to distortion and attenuation of the pulse. To preserve the broad frequency content, Auston constructed photoconductive dipole antennas, excited by femtosecond visible or near infrared laser pulses, in order to radiate the electrical pulses into free space[26]. A delayed portion of the laser beam was used to sample the free space transients by gating a similar photoconductive dipole connected to a current amplifier. The current, proportional to detected electric field, was then recorded as a function of delay. The freely propagating transient technique is inherently time-domain and the final result of an experiment is an optoelectronically reconstructed time-domain signal. Fourier analysis is used to convert from the time domain to the frequency domain. This opened the way to transmission spectroscopy and in a series of papers Fattinger and Grischkowsky[27] described improvements to the method culminating in a spectroscopy capability with unrivalled sensitivity over the range 0.1-3 THz.

Parallel development of all optical THz generation and detection techniques took place using electro-optic (EO) crystals. By the physical process of optical rectification, an optical pulse travelling through an EO crystal will create an associated polarisation wave. Due to the second-order nonlinear polarisation of the crystal this wave will contain components at the sum and difference frequencies of the pulse. If the optical pulse is very short (fs or ps duration), this time-varying polarisation wave will radiate components in the THz frequency range[28,29]. In order for the difference wave, generated along the path of the pulse in the crystal, to

interfere constructively the material must either be phase matched or short compared with the difference wavelength. Phase matching requires that the refractive index of the media for the generation pulse and difference frequencies be similar. All optical detection can be achieved by measuring the rotation of a probe beam caused by the electric field of a THz transient passing through an EO crystal[28,30]. In order to optimise the time resolution the probe beam must pass through the EO crystal, co-linear with the transient.

The dipole and all optical devices each offer their own advantages and disadvantages and different combinations can be chosen to fulfil particular requirements. The photo-gated transmitters produce more power than the faster all optical transmitters and the dipole receivers are more sensitive than the EO crystals but over a narrower bandwidth[31]. In addition, the dipole receivers are exceptionally stable, well matched to the dipole transmitter bandwidth and are not subject to the spurious structure typically added to all optical receiver signals by phonon absorption and surface reflections. Supplementary capabilities are also available: by varying the periodicity of the bias voltage applied to photoconducting antenna arrays, it is possible to vary the frequency[32] and direction[33] of the emitted radiation or by using an optically chirped pulse in an electro-optic detection system a spatio-temporal distribution of a single THz pulse can be imaged without the need to sweep the delay of the probe beam[34]. Other forms of detection include direct measurement of the magnetic field component of the transient[35] and bolometers have also been used[36]. The bolometer's response time is much longer than the width of the THz transient and so interferometric techniques must be employed to recover frequency information.

This thesis describes some developments of THz spectroscopy and its application to the study of aspects of the coherent dynamics of charge carriers in semiconductors. The spectrometer used is based on Auston switches and chapter 2 contains a fuller description of the experimental apparatus and techniques used in THz spectroscopy. Investigations into optimising the sensitivity and bandwidth of the spectrometer are also described.

Chapter 3 concerns the determination of FIR optical constants of heavily doped GaAs epilayers by two methods: complex amplitude transmission and the Hall effect.

The response of GaAs/AlGaAs and Si/SiGe two dimensional electron gases (2DEGs) to incident THz transients in a magnetic field is discussed in Chapter 4. The observation of cyclotron oscillations permits a determination of the carrier effective mass and dephasing time and their dependence on carrier density and temperature. The first example of coherent control of an intraband process, cyclotron motion, is also described.

In Chapter 5 the first time domain observation of coherent cold 2DEG plasma oscillations is described. The carrier density and magnetic field dependence of these oscillations is explored. Impulsive interband excitation of 2D plasmons is also described. Conclusions and some indications of directions for further research are outlined in Chapter 6.

References

(1) "Heinrich Hertz", Ed. P. Hertz, San Francisco Press Inc. (1977)

(2) D. H. Auston, K. P. Cheung and P. R. Smith, Appl. Phys. Lett. **45**, 284, (1984)

(3) D. Grischkowsky, S. R. Keiding, M. van Exter and Ch. Fattinger, J. Opt. Soc. Am. **B 7**, 2006 (1990); N. Katzenellenbogen and D. Grischkowsky, Appl. Phys. Lett. **61**, 840 (1992)

(4) M. C. Nuss, K. W. Goosen, J. P. Gordon, P. M. Makiewich, M. L. O'Malley and M. Bhushan, J. Appl. Phys. **70**, 2238 (1991)

(5) M. van Exter, Ch. Fattinger and D. Grischkowsky, Opt. Lett. **14**, 1128 (1989)

(6) H. G. Roskos, M. C. Nuss, J. Shah, K. Leo, D. A. B. Miller, A. M. Fox, S. Schmitt-Rink and K. Köhler, Phys. Rev. Lett. **68**, 2216 (1992)

(7) C. Waschke, H. Roskos, R. Schwedler, K. Leo, H. Kurz and K. Kohler, Phys. Rev. Lett. **70** 3319 (1993)

(8) W. Sha, A. L. Smith and W. F. Tseng, Phys. Rev. Lett. **74**, 4273 (1995)

(9) D. Some and A. V. Nurmikko, Appl. Phys. Lett. **65**, 3377 (1994)

(10) W. J. Waleki, D. Some, A. V. Nurmikko, Appl. Phys. Lett. **63**, 1809 (1903); D. M. Mittleman, J. Cunningham, M. C. Nuss, M. Geva, Appl. Phys. Lett. **71**, 16 (1997)

(11) R. A. Cheville, D. Grischkowsky, Phys. Rev. **E 50**, 1336 (1994)

(12) B. N. Flanders, R. A. Cheville, D. Grischkowsky, N. F. Scherer, J. Phys. Chem. **100**, 11824 (1996)

(13) R. A. Cheville, D. Grischkowsky, Appl. Phys. Lett. **67**, 1960 (1995)

(14) D. M. Mittleman, R. H. Jacobsen and M. C. Nuss, IEEE Journal of Selected Topics in Quantum Electronics **2**, 679 (1996)

(15) D. M. Mittleman, S. Hunsche, L. Boivin and M. C. Nuss, Opt. Lett. **22**, 904 (1997)

(16) S. Verghese, K. A. McIntosh and E. R. Brown, Appl. Phys. Lett. **71**, 2743 (1997)

(17) "Low-Dimensional Semiconductors," M. J. Kelly, Clarendon Press, Oxford (1995) p. 393
"Semiconductor Devices: Physics and Technology", M. Sze, Wiley, New York (1985) p. 222

(18) P. Pfeffer, W. Zawadzki, K. Unterrainer, C. Kremser, C. Wurzer, E. Gornik, B. Murdin and C. R. Pidgeon, Phys. Rev. **B 47**, 4522 (1993)

(19) P. R. Smith, D. H. Auston, A. M. Johnson and W. M. Augustyniak, Appl. Phys. Lett. **38**, 47 (1981)

(20) "Picosecond Optoelectronic Devices", D. H. Auston, Academic Press, London (1984), p. 73

(21) M. B. Ketchen, D. Grischkowsky, T. C. Chen, C. C. Chi, I. N. Duling, N. J. Halas J. M. Halbout, J. A. Kash and G. P. Li, Appl. Phys. Lett. **48**, 751 (1986)

(22) M. van Exter and D. Grischkowsky, IEEE Transactions on Microwave Theory and Technique **38**, 1684, (1990)

(23) J. T. Darrow, X.-C. Zhang, D. H. Auston and J. D. Morse, IEEE Journal of Quantum Electronics **28**, 1607 (1992)

(24) W. H. Knox, Appl. Phys. A **53**, 503 (1991)

(25) "Optoelectronic Techniques for Microwave and Millimetre-wave Engineering" W. M. Robertson, Artech House Inc, Norwood (1995), p 140

(26) D. H. Auston, K. P. Cheung and P. R. Smith, Appl. Phys. Lett. **45**, 284 (1984)

(27) Ch. Fattinger and D. Grishkowsky, Appl. Phys. Lett. **53**, 1480 (1988); Ch. Fattinger and D. Grishkowsky, Appl. Phys. Lett. **54**, 490 (1989); M. van Exter, Ch. Fattinger and D. Grishkowsky, Appl. Phys. Lett. **55**, 337 (1989)

(28) D. H. Auston, Appl. Phys. Lett. **43**, 713 (1983)

(29) X.-C. Zhang, B. B. Hu, J. T. Darrow and D. H. Auston, Appl. Phys Lett. **56**, 1011 (1990)

(30) P. Uhd Jepsen, C. Winnewisser, M. Schall, V. Schyja, S.R. Keiding and H. Helm Phys. Rev. **E 53**, R3052 (1996)

(31) Y. Cai, I. Brener, J. Lopata, J. Wynn, L. Pfeiffer, J. B. Stark, Q. Wu and X. -C. Zhang and J. F. Federici, Appl. Phys. Lett. **73**, 444 (1998)

(32) B. B. Hu, N. Froberg, M. Mack, X.-C. Zhang and D. H. Auston, Appl. Phys. Lett. **58** 1369 (1991)

(33) N. Froberg, M. Mack, B. B. Hu, X.-C. Zhang and D. H. Auston, Appl. Phys. Lett. **58** 446 (1991)

(34) Zhiping Jiang and X.-C.Zhang, Appl. Phys. Lett. **72**, 1114 (1998)

(35) J.A. Riordan, F. G. Sun, Z. G. Lu and X.-C. Zhang, Appl. Phys. Lett. **71**, 1452 (1997)

(36) S. E. Ralph and D. Grischkowsky, Appl. Phys. Lett. **60**, 1070 (1992)

2 Experimental Techniques

2.1 Introduction

The following section (2.2) covers the rudimentary basics of the spectrometer in order that details in subsequent chapters may be clearer. The apparatus and method described for the generation and detection of quasi-single cycle electromagnetic transients in the THz region of the spectrum is essentially the same as that developed by van Exter and Grischkowsky[1]. The continuing utility of the time domain THz technique has provided the impetus behind numerous advances in THz spectrometer bandwidth and sensitivity. Alternative electrode design, such as singular electric field[2] and logarithmic periodic antennas[3], and substrate choices, including superconductors[4], silicon on oxide on silicon (SiOSi)[5] and low temperature grown GaAs (LT GaAs)[2], have been demonstrated for emitters and receivers. Increased sensitivity and bandwidth are desirable both for improving signal to noise ratios in transmission spectroscopy and for observing relatively weak emission. Throughout the period leading up to this thesis alternative transmitter and receiver designs have been implemented to improve the spectrometer. Section 2.3 will cover the study of four enhancements that have been evaluated: singular electric field electrodes, excitation beam line focusing and polarisation selection and use of SiOSi as a receiver material. Section 2.4 deals with the characterisation of the THz pulse's frequency content and response of the dipole receiver through interferometric techniques.

2.2 The Time Domain THz Spectrometer

2.2.1 Near Infrared Pulse Generation and Optics

At the heart of the spectrometer is the mode locked titanium doped sapphire laser which generates approximately 70 femtosecond pulses of tuneable laser light from 740 nm to 830 nm at a repetition rate of 82 MHz. In transmission mode the laser is typically tuned to 765±5 nm, well above the bandgap of GaAs and Si. The Ti:Sapphire laser output is approximately 800 mW average power at 765 nm (~ 140 kW peak power, ~ 10 nJ per pulse). On exiting the laser cavity the beam is double passed through a pair of prisms. The beam is refracted through the tip of the first prism and spatially split into its spectral components and is then refracted through the tip of a second prism such that the collimated beam is reflected from the surface of a mirror to retrace its path through the prisms. Due to refraction by the prisms the path length is greater for longer wavelengths introducing a negative chirp to compensate for the positive chirp introduced by the dispersion of the laser output coupler and other visible optics. The beam is next split in two via a beamsplitter and the separate beams passed to THz receiver and transmitter respectively (figure 2.1). An autocorrelator is used at the transmitter end of the beam to calibrate the temporal width of the laser pulses, however for normal operation the width is determined qualitatively with an optical spectrum analyser monitoring the output of the laser (a short pulse in the time domain necessarily has a large spectral bandwidth). A rapid scanning delay line inserted in the transmitter beam allows the time delay between the two beams to be varied by up to 150 ps at frequencies up to 10 Hz. This enables the temporal field profiles of the THz pulses to be reconstructed on an oscilloscope in real time, greatly improving the ease with which the system can be aligned. Because the time domain terahertz spectrometer (TDTS) measures electric field amplitude, with n successive averages the noise signal approaches zero in proportion to $n^{-1/2}$. This reduces the primary source of noise, power fluctuations of the laser (~ 0.1% rms). In addition, since averages are taken over whole scans, fluctuations caused by average laser power drift (~ 1%/hour) are also minimised. Typically 500

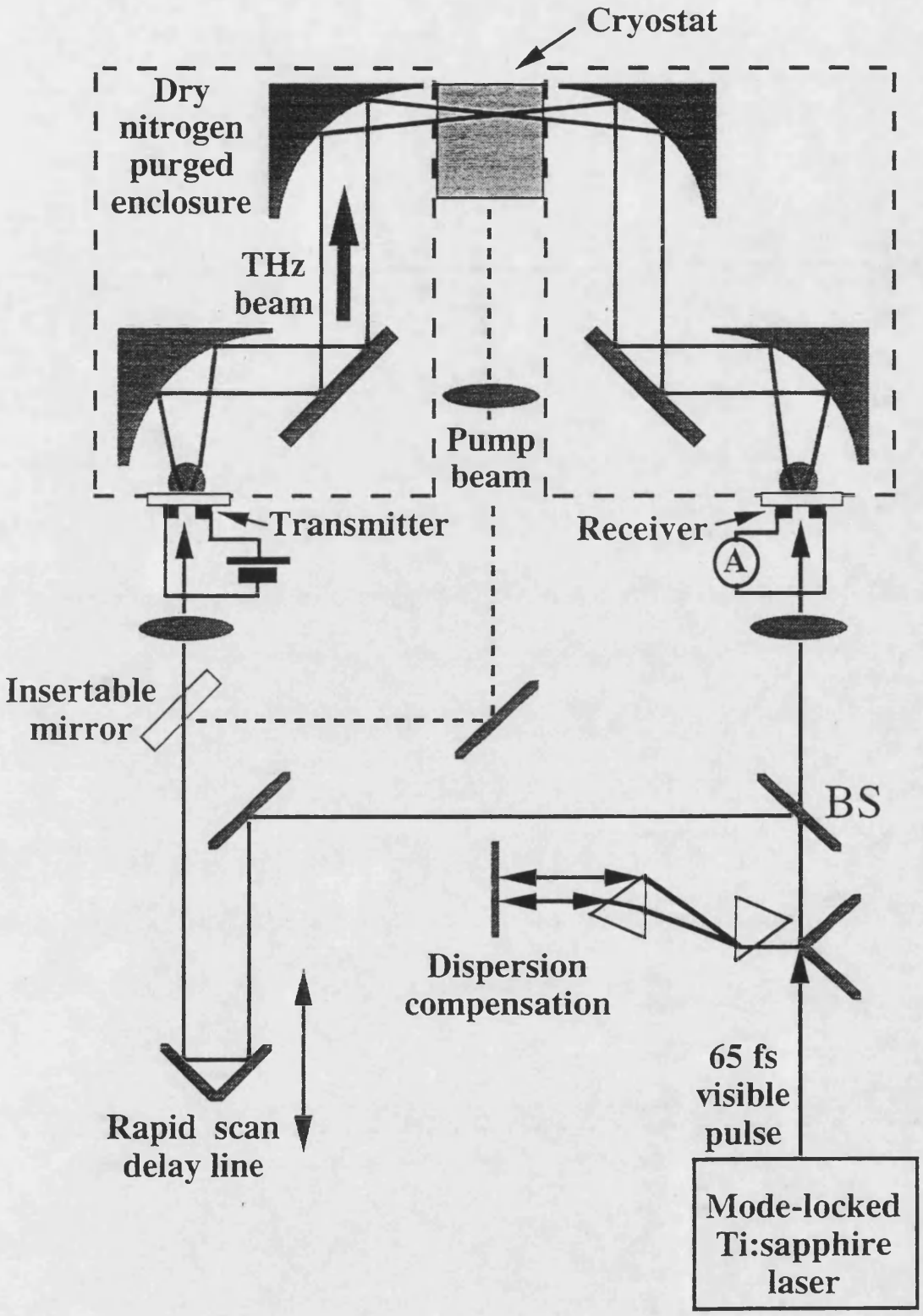

Figure 2.1: Schematic drawing of the coherent time-domain THz spectrometer.

scans are averaged, thus improving the signal to noise ratio by a factor of 22, assuming the noise to be random.

2.2.2 Generation of THz Transients

The TDTS may be implemented in several different ways, the two most common of which are the transmission and emission modes of operation. The transmission approach uses femtosecond visible or near infrared laser pulses to generate quasi single cycle electric field transients. A delayed portion of the laser beam is used to sample the THz transient after passing through the test object, this probe beam signal is then recorded as a function of delay. In emission mode the test sample itself is directly excited by sub picosecond near infrared laser pulses and is the source of any coherent generated THz emission which can be detected by the receiver. Visible pump-THz probe measurements are also possible[6]. Both transmitter and receiver assemblies of the spectrometer are the subject of continuous refinement, aimed at improved bandwidth and sensitivity and such improvements will be discussed in section 2.3. However, the fundamental mechanisms behind each remain the same and therefore the following details of a commonly used transmitter and receiver pair is intended only as a general description.

The coplanar stripline (CPS) transmitter depicted in figure 2.2a consists of two 150 nm thick, 25 mm long and 10 μm wide Ti/Au tracks, separated by a gap of 50 or 80 μm and deposited on semi-insulating (SI) GaAs. This design of transmitter was found by Katzenellenbogen and Grischkowsky[7] to radiate faster and more powerful transients than the original silicon Auston switches (very similar to dipole receiver design, figure 2.2b). They found that focusing the excitation beam close to the positive track lead to the strongest THz emission, possibly because of the presence of traps in the SI GaAs[8] and the different mobilities of electrons and holes[9]. As the transmitter substrate, GaAs's high resistivity and mobility allows for faster and larger transients than materials such as silicon.

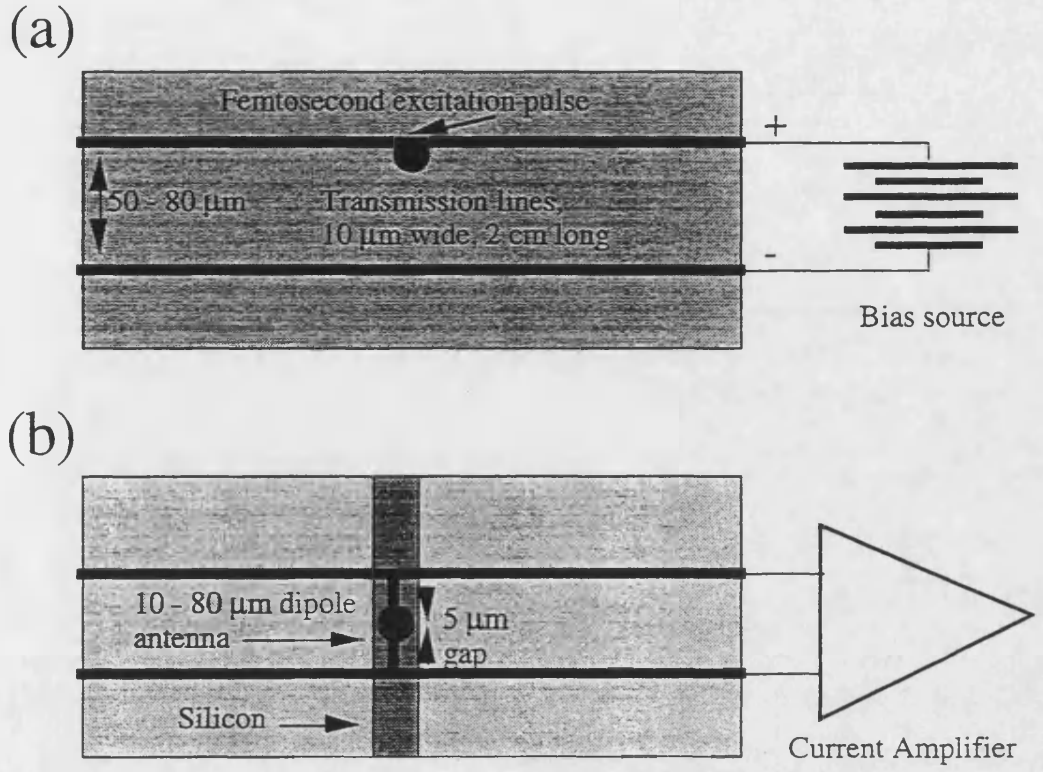

Figure 2.2: Simplified structures of typical (a) GaAs coplanar stripline transmitter and (b) silicon on sapphire dipole receiver chips.

With an external electrical bias of around 60 V applied between the tracks, the excitation beam from the Ti-Sapphire laser is brought to a focal spot ~ 5 µm in diameter next to the anode by means of a ×20 microscope objective. The typical average power in the excitation beam is around 30 mW, beyond which the radiated THz amplitude begins to saturate. Above 60 mW (300 kW/cm^2 fluence) permanent thermal damage can occur[10]. The above band gap excitation beam generates electron-hole pairs within a few microns of the surface which are subsequently accelerated by the imposed electrical field until they reach drift velocity. The electric field of the excitation beam is polarised perpendicular to the axis of the metal tracks since this increases the amplitude of the emitted THz radiation four-fold over the opposite

polarisation of the excitation beam. This is believed to arise from the optical field distribution at the edge of the metal track and will be discussed in section 2.3.1. Cumulative screening effects are avoided as the carriers recombine or traverse the gap on a time scale shorter than the Ti:Sapphire repetition period (~ 12 ns). As with Hertz's spark gap, the transient current, j(t), has an associated transient electric field,

$$E(t) \propto \frac{dj}{dt} = \left(\frac{dn}{dt}\right) ev(t) + n(t)e\left(\frac{dv}{dt}\right) \qquad (2.1)$$

where n is the number of carriers, v the average velocity and e the fundamental electronic charge. During illumination, equation 2.1 is dominated by the dn/dt displacement current term. Post illumination, the photogenerated carriers continue to accelerate in the applied field until they reach drift velocity or the field is screened as holes and electrons spatially separate. Using such a model, Keiding *et al.*[10] have successfully reproduced the qualitative shape of THz transients from biased coplanar striplines. Due to the refractive index mismatch at the SI GaAs/air interface the radiation is preferentially emitted into the chip and coupled into a high resistivity, hyper-hemispherical, silicon lens attached to the opposing face of the chip, which partially collimates the emitted radiation.

To change the spectrometer to emission mode one inserts the mirror in figure 2.1 and the excitation beam is redirected through one of the fused quartz windows of the cryostat so as to illuminate the sample. The tunability of the laser permits access to energies above and below the bandgap of GaAs both at room and cryogenic temperatures. An average laser power of up to 450 mW is available at the cryostat window. Such femtosecond, above bandgap illumination has been shown to result in the emission of coherent THz radiation from certain semiconductor structures. Examples include the acceleration of optically injected carriers by surface fields[11], optical rectification[12], coherent optical phonons[13], bulk[14] and two dimensional plasmons[20] and charge oscillations associated with quantum beats in asymmetric coupled quantum wells[15]. The illumination of a surface by a plane wavefront at an angle results in an ensemble of excited dipoles out of phase with each other as a result of the path difference between points on the oblique surface.

Hence only emission directions which recover equal path lengths will constructively interfere. Consequently THz emission occurs along the paths of transmission and reflection of the excitation laser beam. Emission is measured along the reflection path (the transmission path is avoided because it would mean relocating the THz optics) which is detected with the dipole receiver and optics in the same manner as that for transmission measurements. The reflection of the visible excitation beam is prevented from reaching the receiver by the silicon window of the cryostat.

2.2.3 Coherent detection of THz Transients

The transmitters and receivers share many common features, as with Hertz's early work (figure 2.2) and detection of the FIR transient is similar in many ways to generation. A silicon, hyper-hemispherical lens couples the free space radiation into the dipole receiver, typically an ion implanted, silicon on sapphire (SOS) chip. In all optical receivers, the need for the probe beam to pass through the EO crystal, co-linear with the transient, precludes the use of a visibly opaque silicon lens which greatly enhances the sensitivity of the dipole antenna. In our receiver the 430 μm thick $(1\bar{1}02)$ sapphire substrate is grown to achieve an appropriate match with the lattice constant of the 0.6 μm thick, epitaxially grown (100) silicon. On the opposite face of the chip a pair of Ti/Au tracks is deposited. Although no annealing of the tracks is used the ion implantation facilitates ohmic contact to the silicon layer through defect states generated by the implantation[16]. This gives a lower contact resistance and an increased current for a given voltage between the tracks. The centre of each track extends as an antenna stub terminating at the centre of the chip with a 5 μm gap separating one from the other (figure 2.2b). The stripline structure is oriented to detect THz radiation propagating with minimum dispersion in the sapphire, i.e. with electric field, and antenna stubs, perpendicular to the extraordinary axis[17]. Silicon not immediately surrounding the active 5 μm gap is etched away by SF_6:O_2 plasma reactive ion etching to reduce Johnson noise between the tracks[1]. An anti-reflection coating (1/4 wavelength layer of SiO_2) is sputtered on to the surface of the chip to maximise visible light input and protect it from damage. The receiver

gating beam, delayed with respect to the transmitter excitation beam, is focused to a ~ 5 μm spot in the centre of the silicon gap. The average laser power is limited to ~ 20 mW to avoid thermal damage to the receiver[10]. In the absence of the gating beam, the 5 μm silicon gap presents an impedance of ~ 100 kΩ but becomes ~ 0.1 Ω for the duration of illumination effectively shorting out the resistive gap. Hence the coincidence of an electric field transient at the antenna stubs together with a laser pulse shorting out the resistive gap between the stubs results in a current proportional to the instantaneous field strength. A low noise, current amplifier with a 20 kHz bandwidth limit then converts this current to a voltage with a typical gain of 10^8 V/A. The electric field of the transient is mapped out as a function of delay of the receiver gating beam, temporally resolving the transient on a sub picosecond scale in real time on a storage oscilloscope. The data can then be Fourier transformed to obtain an amplitude spectrum. Signal to noise ratios exceeding 10^5 in the amplitude spectrum (10^{10} in power) are possible, as the coherent detection of field overcomes the problem of the thermal background, to which all power detectors are subject.

The practical bandwidth of the receiver is determined by the dimensions of the antenna stubs. The efficiency of the antenna drops as the frequency rises and the wavelength in the silicon approaches the size of the dipole. The ultimate upper frequency limit is dependent on the carrier lifetime[18]. Figure 2.3 displays the temporal response and bandwidths of 3 different sized antennas from 10 to 80 μm. A useful point of reference when considering the bandwidth is the upper frequency at which the amplitude has decreased to one tenth of the maximum (10^{-2} in power), designated $f_{0.1}$. The widest bandwidth is obtained from the smallest, 10 μm, antenna which typically yields an amplitude spectrum peaking at 1 THz, with $f_{0.1}$ at 3.3 THz. The silicon layer of the receiver is implanted with 100 and 200 keV oxygen ions to give an even spread of damage with depth at a total dose of 10^{15} cm^{-2}. This resulted in a reduction of the free carrier lifetime from ~ 1 μs to ~ 600 fs, in agreement with previous results[19], the latter value was estimated by time dependent reflectivity. The silicon resistivity initially increased with implantation dose from the unimplanted value of 100 Ωcm, reaching a peak of 6.10^4 Ωcm at a dose of 10^{13} cm^{-2}. Further

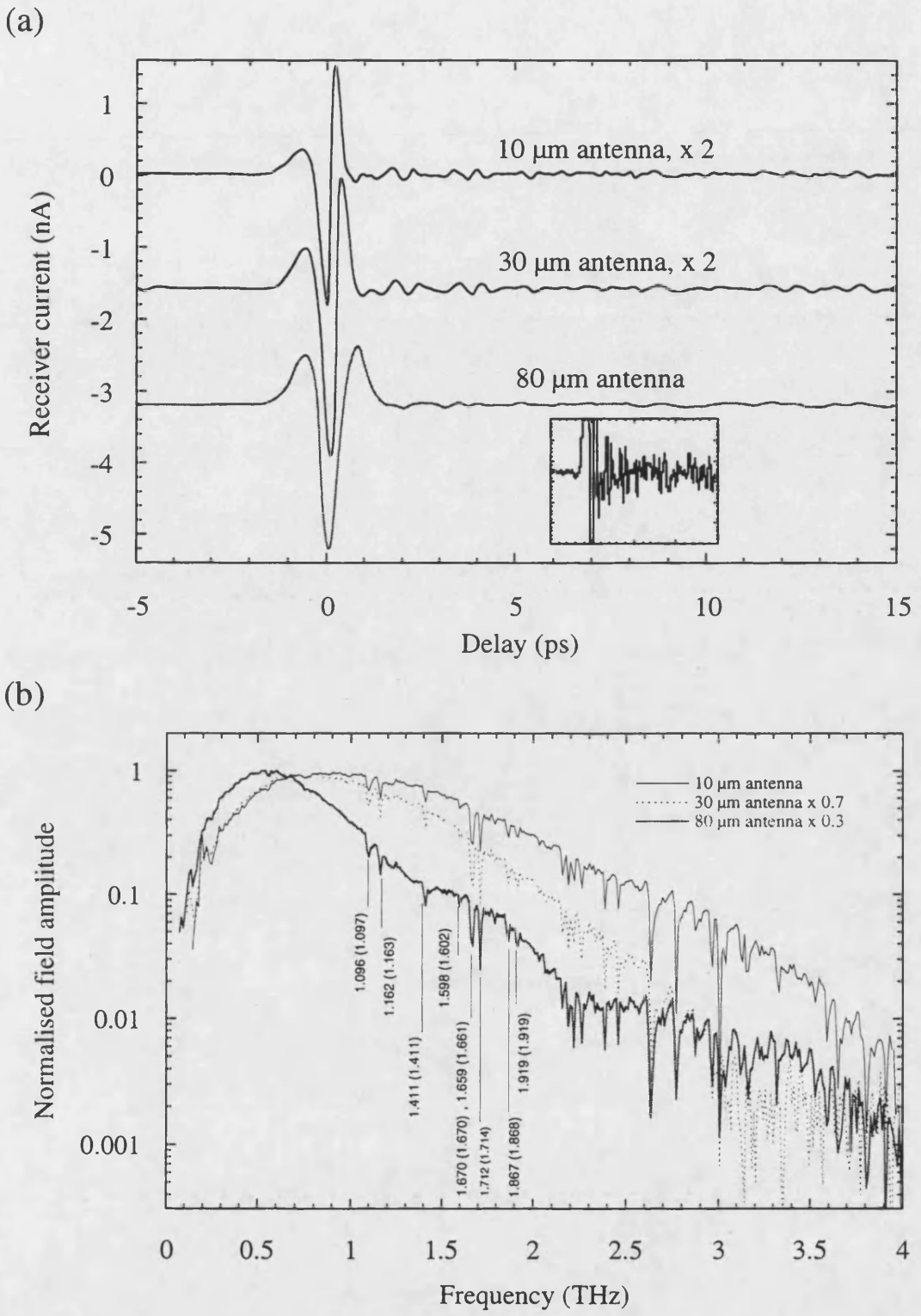

Figure 2.3: Examples of quasi single cycle pulses (a) and their associated spectra (b) produced by a GaAs CPS transmitter and detected by SOS dipole receivers of three different dipole lengths: 10 µm, 30 µm and 80 µm. A close up of the 10 µm trace just after the main transient is shown in the inset of (a). Arrows in (b) give the positions and measured frequencies of water absorption lines, literature values[19] are given in parenthesis. The time domain traces have been offset to aid clarity.

implantation reduces the resistivity and a value of 5 kΩcm at a dose of 10^{15} cm^{-2} was measured. Hence a reduction in the carrier lifetime leading to an increased upper frequency limit whilst maintaining a reasonable mobility for high sensitivity was achieved.

2.2.4 THz Optics

In transmission mode the FIR radiation is quasi-collimated and then brought to a 3 mm focal spot by a combination of hyper-hemispherical silicon lens and off-axis parabolic mirrors after generation inside the transmitter chip (figure 2.1). A similar optical system recollimates and focuses the transient onto the silicon-on-sapphire dipole receiver. The essential aim of the THz optical system is to focus the FIR beam to a diffraction-limited focal spot at the point where the sample is inserted and to do this with minimal power loss and dispersion.

The first component of the THz optics encountered by the transient is the high resistivity silicon lens (figure 2.4). The back of the transmitter chip is separated from the lens by a thin film of paraffin oil to reduce reflection losses at the interface and to provide lubrication for adjusting the lens position. Despite the slight refractive index mismatch with the GaAs transmitter, silicon does not result in significant reflection losses at the interface and was chosen for its low dispersion and absorption qualities in the FIR[1].

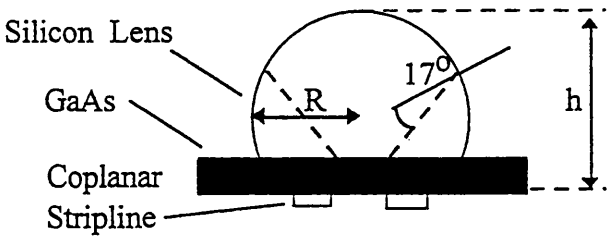

Figure 2.4: Schematic diagram of a silicon lens and transmitter chip assembly

The hyper-hemispherical lens design is such that, ignoring diffraction, radiation from the transmitter is collimated when the antenna is located at a distance h from the tip of the lens given by

$$h = \frac{Rn}{n-1} \qquad (2.2)$$

where R is the radius of the lens (4.75 mm) and n is the refractive index of silicon. Light incident at angles larger than 17° to the lens-air interface surface normal are lost due to total internal reflection, thus determining the width of the lens' THz exit pupil (figure 2.4)[1]. The diameter of the THz beam at the lens air interface (~ 9.5 mm) is a significant number of wavelengths across (λ = 0.6 mm at 0.5 THz) and hence the beam diverges through diffraction limitations. Coupling efficiency and bandwidth are critically sensitive to the lens position relative to the laser focus on the CPS on a micron scale, indicating the size of the radiating dipole. Hence the lens is held in place against the chip by a soft spring and its location in the plane of the chip is adjustable by micropositioners.

After the hyper-hemispherical lens the divergent wavefront is quasi collimated by an off-axis parabolic mirror with the transmitter approximately at its focus (f_1 = 75 mm). The beam is then passed to a second off-axis parabolic mirror (f_2 = 250 mm), displaced from the first by the sum of their focal lengths to limit the diffraction of the beam[10]. The second mirror refocuses the beam to 3 mm full width half maximum at the centre of a sample space in the bore of a split coil superconducting magnet. An identical set of optics then guides the beam to the dipole receiver.

The FIR cold windows of the cryostat, which seal the helium gas cooled sample space from the outer vacuum jacket, are made from high resistivity silicon in order to minimise absorption and dispersion. The windows are 2 mm thick so that reflections occur approximately 46 ps after the main transient. The outer windows which seal the vacuum jacket are made of mylar which, with a lower refractive index, loose less light than silicon through reflection. However mylar is more absorbing and

dispersive than silicon in the THz region and consequently these windows are only 200 μm thick.

In Fourier transform interferometry (FTIR) it is common to wedge the sample with a shallow angle (3°-5°) in order to reduce the strength of interference fringes from reflections, however this wedge steers the transmitted beam. In FTIR this not an insurmountable problem as the beam requires only an adjustment of the sample angle to rectify. Due to the sensitive nature of the THz focusing optics this is not feasible in the TDTS and in addition the transient would be delayed by differing amounts across the wedge, broadening the pulse. Hence we suffer reflections, typically arriving at the receiver around 10 ps after the main transient for samples ~ 0.5 mm thick. Optically contacting a thick transparent substrate of equal refractive index to the test sample helps to reduce reflections but does not eliminate them completely. Numerical subtraction has been suggested as a method of easing this problem[20], but reflections generally suffer too much dispersion for this technique to be applied.

In order to ensure the beams reaching the sample under test and the receiver are plane polarised free standing wire grid polarisers are placed in both collimated sections of the beam. The polarisers have 40 wires per mm and a wire diameter of 10 μm. Even though such a polarised beam is not always necessary the polarisers are left in place as they do not significantly attenuate the signal because both transmitter and receiver are themselves polarisation sensitive[21,22].

The inset of figure 2.3a shows a close up of the receiver current after the initial transient. Water vapour has several strong pure rotational transitions covering the spectrum of the transient[23] and the sharp absorption lines in the Fourier transform (figure 2.3b) and structure after the pulse (inset figure 2.3a) arise from the free induction decay of water molecules in the beam path. These well known absorption lines provide a useful calibration tool[24] but are otherwise a confusing distraction and can halve the power throughput. To reduce the absorption by water vapour the optics described above, with the exception of the cryostat, are housed in perspex dry boxes purged by dry air.

2.3 Spectrometer Performance Enhancement

2.3.1 Transmitter and Receiver Excitation Beam Polarisation Sensitivity

The THz CPS emitter can be considered as a dipole point source and as such the degree of polarisation of the emitted THz radiation[21] is well known as is the polarisation sensitivity of the receiver[22] to this radiation. In contrast, the dependences of THz generation and detection on the polarisation of the optical pump and probe beams is less well known, although this might be expected to be important because of the electrode-semiconductor interface geometry and the similarity of the relevant length scales to the optical wavelength.

The effect of the optical polarisation direction on the efficiency of GaAs coplanar stripline transmitters and of silicon-on-sapphire (SOS) dipole receivers has thus been investigated. A strong polarisation dependence was found in both, with up to a four-fold difference in radiated field strength from a 50 μm GaAs CPS and a three-fold difference in sensitivity existing between orthogonal exciting polarisations of a 30 μm SOS dipole receiver. The polarisation of the excitation beams was selected using Fresnel rhomb half wave retarders in each beam. For TE (TM) the electric-field vector is parallel (perpendicular) to the direction of the stripline. The combined one order of magnitude difference is of practical importance in optimising the signal-to-noise ratio in time-domain THz spectroscopy.

Considering first the transmitter, the dependence of the emission strength on excitation position and polarisation was studied. For this measurement the hyper-hemispherical lens was positioned to give optimum signal when exciting midway between the anode and cathode. The resulting TE and TM signal amplitudes from a transmitter fabricated on (100) GaAs are displayed in figure 2.5, similar results were obtained from the other transmitters studied, including ones fabricated on differently oriented substrates and ones with annealed contacts. The data shown were obtained at

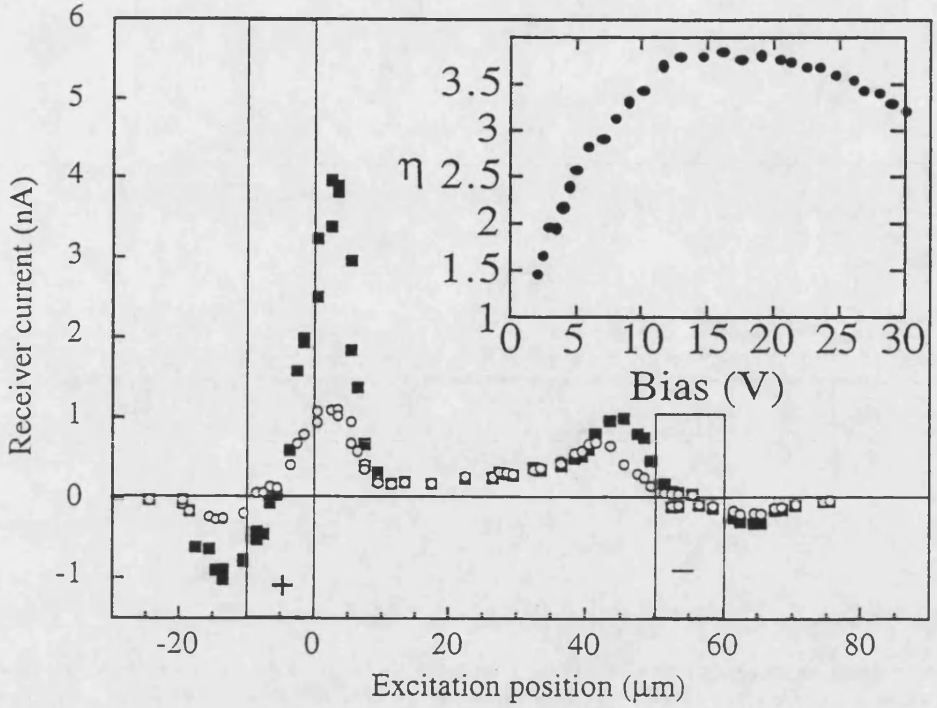

Figure 2.5: Peak signal amplitudes from TE (open circles) and TM (solid squares) polarisations as a function of excitation position for a 50 μm coplanar stripline transmitter. Excitation power was 30 mW with an applied bias of 28 V. The vertical stripes indicate the anode (+) and cathode (-). The inset shows the ratio of THz field strengths $\eta = E_{THz}(TM)/E_{THz}(TE)$ as a function of bias for 28 mW of near-anode illumination.

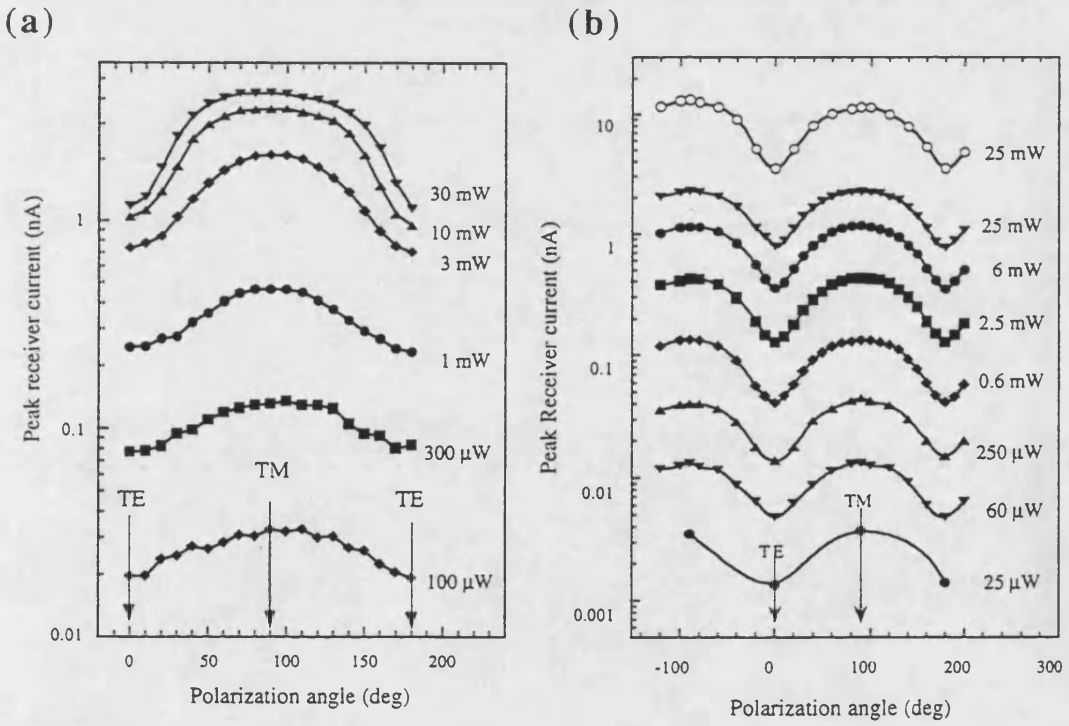

Figure 2.6: Receiver currents as a function of polarisation angle and average power of (a) the GaAs transmitter and (b) SOS receiver excitation. Open symbols indicate the average photocurrent and filled symbols represent the peak amplitude of the THz transients. Lines are drawn as a guide for the eye. The arrows indicate TE and TM excitation.

a bias of 28 V and an incident power of 30 mW. The relative positions of the anode and cathode are also indicated in the plot.

Figure 2.5 shows that the amplitude of the radiated signal, proportional to local electric-field strength, does not depend on the polarisation at distances greater than about 10 μm from the electrodes. The TM signal is ~ 4 times the TE signal at the anode, and about 50% stronger at the cathode. The strong increase close to the electrodes can be partly attributed to a geometrical enhancement of the electrostatic field gradient. The larger signals at the anode may arise from a combination of the presence of traps in the semi-insulating GaAs[8] and the different mobilities of electrons and holes.[9] The dark current-voltage characteristics of the transmitters are similar to those predicted by a simplified model of space-charge currents in an insulator with traps[25]. In this model an initial Ohmic regime gives way, with increasing bias, to a steep trap-filled limit rise in current. With further increasing bias, a space-charge-limited regime with a weaker, approximately quadratic, bias dependence is entered.

Modelling of a similar structure[8] has indicated that when biased above the Ohmic regime most of the applied potential is dropped within about 5 μm of the anode, with the field increasing by about an order of magnitude in the last 1 μm. It is believed that this strong field concentration causes the difference in radiated THz field strengths between polarisations. Two possibilities suggest themselves: a nonlinear optical contribution to the THz field and a polarisation dependence of the overlap between the photocarrier distribution and the high electric-field region. Field-induced $\chi^{(2)}$ processes[26] may be ruled out by symmetry constraints and the fact that identical behaviour is seen in transmitters fabricated on (111) GaAs. Additionally transmitters with sharply pointed electrodes[21] 50 μm apart, rather than parallel tracks, show a much reduced polarisation dependence despite their geometrical field enhancement. A qualitative picture of the spatial distribution of carrier injection may be obtained from calculations of intensity distributions arising from plane-wave illumination of edges in conducting sheets at dielectric interfaces[27]. The principal

result is that for TE excitation the intensity in the surface plane decreases rapidly over a distance of less than approximately one-quarter of the wavelength in air as the metal is approached and is zero at the interface. In contrast, for TM radiation the intensity increases on approaching the conductor. This is a consequence of the continuity of radiation-induced screening currents at the interface: TE currents are directed parallel to the edge, and thus are finite at the interface. TM currents necessarily drop to zero due to the discontinuity, and thus no screening occurs. A higher excitation density is, therefore, achieved in the enhanced field region close to the anode for TM illumination, thus increasing the radiated field strength. The large observed effect implies that the important field-enhanced region for THz generation is confined to a submicron region extending from the track. This is smaller than generally appreciated. To confirm that rotating the polarisation changes only the spatial distribution of the optical field in the semiconductor and not the power absorbed, the reflected light intensity and the photocurrent were measured and found to be independent of the polarisation angle.

Figure 2.6a shows the dependence of the THz signal emitted from the near-anode region on the polarisation angle at 28 V bias for powers in the range 100 μW-30 mW. The ratio of radiated fields $\eta = E_{THz}(TM)/E_{THz}(TE)$ increases from about 1.8 at 100 μW to about 4 for excitation with 30 mW. Clearly, the optically injected carriers change the field distribution and enhance the overlap of the high-field region with the optically injected electron-hole plasma[8]. A typical plot of the bias dependence of η at a fixed excitation intensity is shown in the inset in figure. 2.5. The detailed variation is difficult to explain but the increase in η with bias is consistent with the calculated narrowing of the high-field region[8].

As in the transmitter, TM excitation of the receiver results in maximum signal (figure 2.6b). The increase in η with power is somewhat weaker than in the transmitter, varying from 2.6 to 3.3 as the average power increases from 25 μW to 6 mW. At the highest power utilised, 25 mW, η has dropped slightly to 2.9. The transmission through the gap of a dipole antenna showed no polarisation dependence,

indicating that the total power absorbed is constant. As in the transmitter, for TE polarisation few photocarriers are excited within a few hundred nm of the electrodes. Because of the short recombination time compared with the time taken to transit this region there is a reduction in the photoconducting gain of the antenna. This is confirmed by measurements of the variation in the average receiver photocurrent, shown as open symbols in figure. 2.6b, which shows a similar variation with polarisation to that of the THz signal current. This background photocurrent arises from asymmetries in the silicon/metal interfaces on either side of the photoconductive gap[1]. The TM/TE photocurrent ratio is similar to that reported in a femtosecond study of an interdigitated photoconductor fabricated on low-temperature-grown GaAs with an electrode separation similar to that of the dipole receiver[28]. In contrast, recent CW (continuous wave) studies of interdigitated InGaAs photodetectors[29] have shown variations in sensitivity with polarisation of only 10%. The difference between CW and pulsed illumination is not thought to be of primary importance: a measurement of receiver photocurrent gave a TM/TE ratio of about 3 for CW illumination, compared with approximately 2.5 for pulsed light of the same average power. Instead, differences in the carrier lifetimes may be more significant. If upper limits of 1 ps for the lifetime and 2×10^5 ms^{-1} for the drift velocity[30] are assumed for the low-temperature-grown GaAs and ion-implanted silicon, then the maximum distance travelled by individual carriers before recombination would be about 200 nm. This is similar to the extent of the dark region next to the electrodes for TE excitation, suggesting that a smaller fraction of photocarriers will be collected in this case. For the InGaAs photoconductor, the carrier lifetime of several ps means that variations in their initial spatial distribution can be neglected. A receiver with a dipole width comparable to the laser spot size showed little polarisation dependence.

2.3.2 Geometrical Field Enhancement

In section 2.2 it was noted that the strongest THz transients are produced in the extremely high field region adjacent to the anode of the transmitter. Further enhancement of the field by geometric effects has been investigated by extending

sharp points from the striplines out towards the gap, similar to those in figure 2.7, to concentrate the electric field[21,2]. In particular a record 500 nA peak receiver current from a LT GaAs dipole receiver with 40 mW illumination was obtained using tight focus (2 μm) 70 mW excitation of sharp electrodes of a LT GaAs transmitter[2]. These transients, radiated from near sharp anode features, have the disadvantage that their spectral content peaks at the relatively low frequency of 0.5 THz and then decreases, approximately exponentially with frequency. For the pointed anode emission from LT-GaAs, $f_{0.1}$ ~ 1.25 THz.

In contrast, the most commonly used technique of near anode excitation of SI GaAs stripline transmitters[7] and detection by ion implanted SOS dipole receivers[17] yields peak photocurrents of some nA only. The widest bandwidth transients reported, typically 5 nA in amplitude and peaking at a frequency of about 1 THz, are achieved using 10 μm dipole receivers. Typical $f_{0.1}$ values are about 3 THz in well aligned systems, but may approach 4 THz for optimum adjustment[31].

Using SI GaAs as a substrate three designs of pointed electrode transmitter were fabricated for study as depicted in figure 2.7. The first design, figure 2.7a, incorporates 37° points at the ends of 20 μm wide arms, extending up to 50 μm in length from both electrodes. The anode to cathode, point to point separation varies from 20 μm to 80 μm. The second design, figure 2.7b, uses the same pointed electrodes as design one for the anode with a 20 μm separation from the tip to the plane stripline of the cathode. Design three, figure 2.7c, used bow tie electrodes with an 80 μm separation between the 45° point tips. The excitation polarisation for both transmitter and receiver was set to be parallel to that of the THz field and for the results presented below the receiver was a 10 μm dipole on SOS unless otherwise stated, gated with 25 mW average power. All three transmitter types displayed similar emissions in terms of amplitude and bandwidth. There was a significant increase in peak signal, typically 10 nA to 14 nA peak receiver currents were obtained for 60 V to 80 V transmitter biases. The spectral content (inset figure 2.8) of these transient peaks at 0.35 THz with $f_{0.1}$ at 1.5 THz and is similar in shape to that obtained from pointed emitters on LT GaAs[2]. The apparent enhancement in amplitude appears to come only at the expense of bandwidth with the increase in receiver current restricted

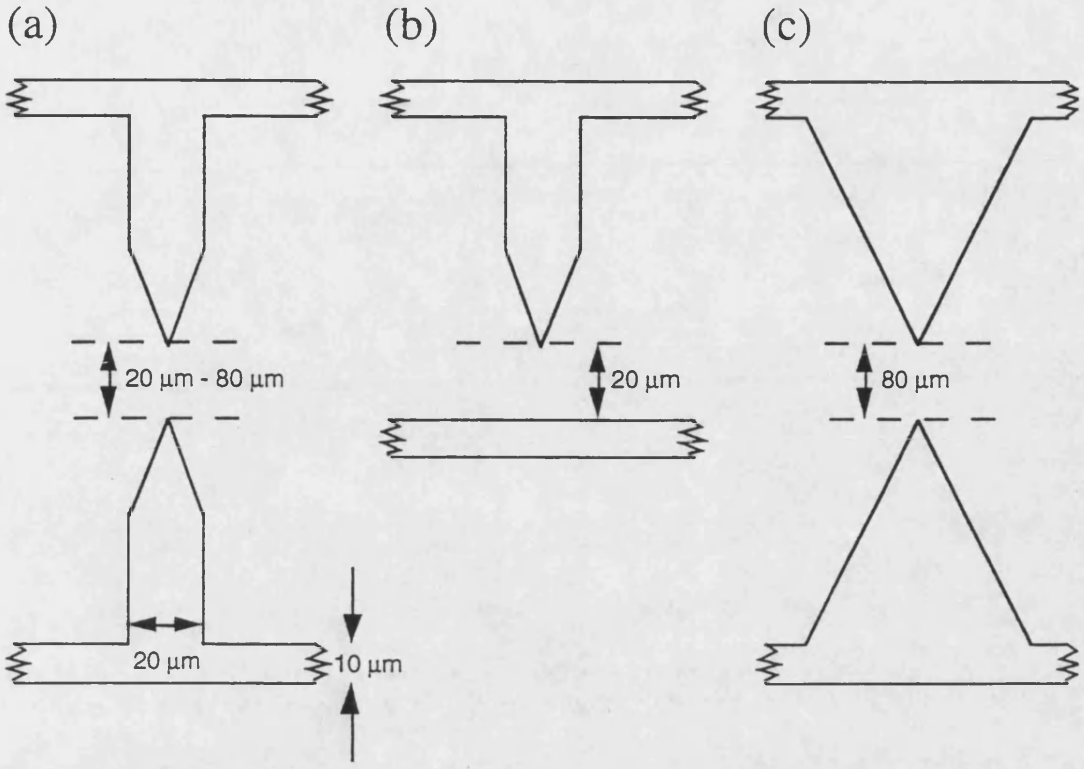

Figure 2.7: Schematic drawings of electrode patterns for various point anode transmitters

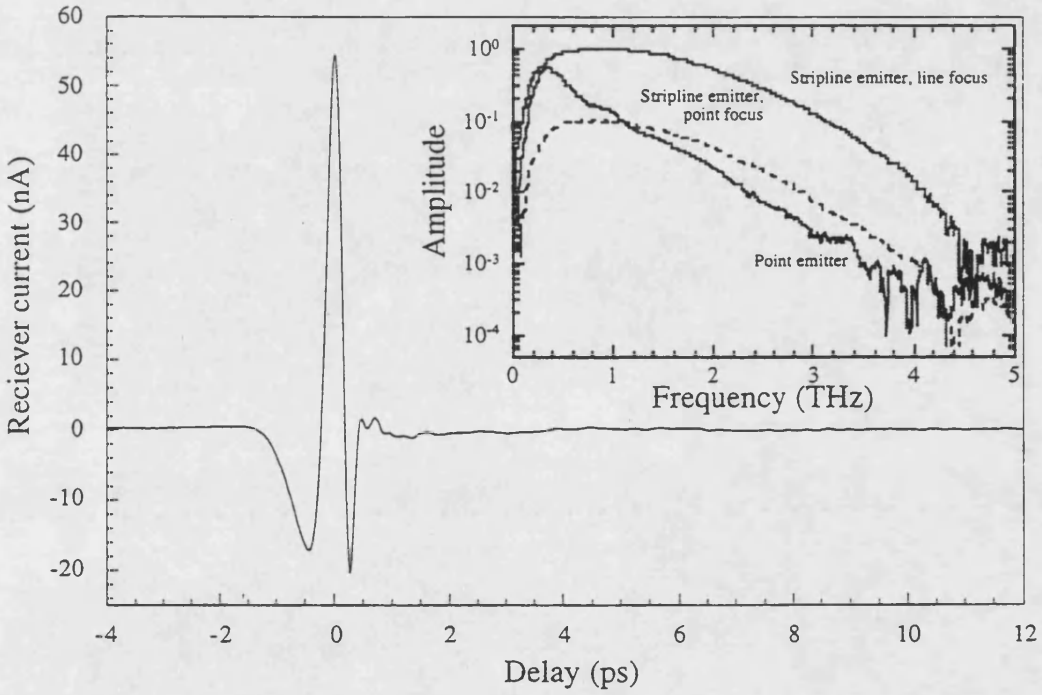

Figure 2.8: THz transient emitted by line focus excitation of a GaAs CPS emitter and detected by a 10 µm silicon on silicon dipole receiver. Transmitter bias is 60 V and incident power 170 mW. Inset shows spectral strengths of various transmitter excitation methods.

to frequencies below 1.1 THz. The peak receiver current could be raised to 22 nA by substituting the 10 μm dipole receiver for an 80 μm dipole. In this case the peak in the spectrum remained at 0.35 THz but with $f_{0.1}$ at 1.0 THz. As with previous LT GaAs studies our strongest emissions emerge from very tight focusing of the excitation beam at the transmitters anode tip. Experiments with tighter focusing using a ×40 microscope objective resulted in similar amplitudes for 14 mW of excitation, but destroyed the transmitter at 22 mW of average power.

2.3.3 Distributed Excitation

In the absence of the excitation beam one can regard the THz emitter as a charged capacitor with stored electrostatic energy equal to $E_s = (1/2)CV^2$, where C is the capacitance of the gap, typically a few fF and V is the applied bias[10]. For a 10 μm spot size, E_s ~ 2 pJ. This is the total amount of energy available to be distributed between carrier kinetic energy and radiation. The idea of attempting to excite a length of the stripline emitter arose from the recognition that the conventional 5 μm point focus used for excitation, inefficiently converts the energy stored in the focal region of the transmitters hyper-hemispherical silicon lens into THz radiation. The insertion of a plano-convex cylindrical lens, f = 5 cm, 50 cm before the microscope objective resulted in the elongation of the excitation focal spot to ~ 100 μm long stripe along the transmitters anode. This ensured relatively uniform illumination within the ~ 50 μm diameter THz focal region of the hyper-hemispherical lens[10]. The emitted THz field amplitude doubled for a given excitation power as a result of the distributed focus without significantly affecting the pulse shape or decreasing the spectral bandwidth (figure 2.9 and inset figure 2.8). Furthermore, reduction of the excitation density raised the excitation power damage threshold. This enabled the average laser power to be raised to 90 mW without risk of damage to the transmitter for a peak receiver current of 17 nA at a bias of 60 V.

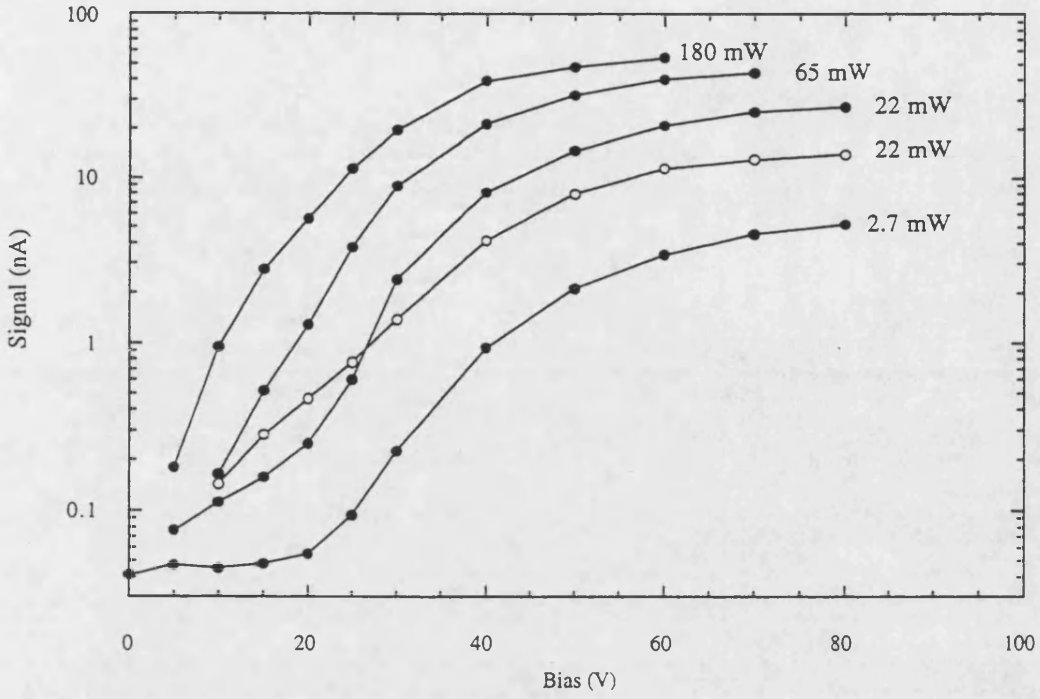

Figure 2.9: Bias dependence of THz signal amplitude detected by a 10 μm SiOSi dipole receiver following point (open symbols) and line (full symbols) focus excitation of a GaAs CPS emitter. Lines are intended as guides to the eye.

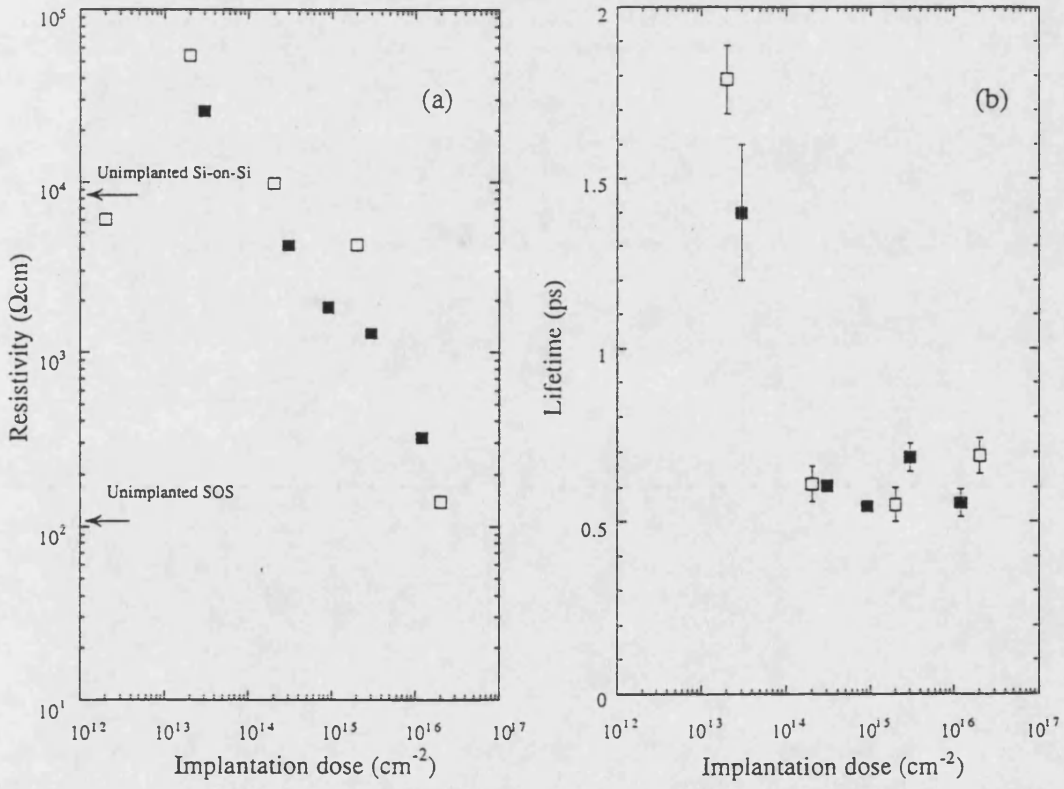

Figure 2.10: (a) Resistivity of oxygen implanted SOS (open symbols) and Si-on-Si (full symbols) as a function of implantation dose. Unimplanted resistivities are indicated by arrows for comparison. (b) Carrier lifetimes as a function of implantation dose.

2.3.4 Silicon on Silicon Dipole Receivers

Recent studies have investigated the effect of material on transient strength and bandwidth[32]. Enhanced efficiency of THz dipole receivers has been reported using LT GaAs photoconductors with their high optical damage thresholds and photoelectron mobility[2]. In addition Katzenellenbogen *et al.*[5] have shown the potential of an ion implanted silicon layer separated by an oxide layer from a silicon substrate (SiOSi) as a receiver photoconductor. The silicon substrate has lower THz dispersion than sapphire[23] and there is the possibility of increasing sensitivity by using a thicker photoconducting layer than available in commercial SOS.

In order to investigate the effect of increased silicon thickness on the THz sensitivity, 1.05 μm of polycrystalline silicon was grown by chemically vapour deposition on 0.6 μm of silicon dioxide, which in turn had been thermally grown on a high resistivity, 1 mm thick, (111) silicon substrate (ρ > 1.4 kΩcm)[33]. The polycrystalline silicon layer was implanted with oxygen ions at energies of 100, 200, 350 and 500 keV in the respective dose ratio 1 : 0.83 : 0.62 : 0.41, to give approximately uniform damage throughout the film thickness. The "as deposited" silicon has a resistivity of nearly 10 kΩcm which is much higher than that of the unimplanted SOS. However, very similar dependencies of resistivity on dose are observed for doses above 10^{13} cm^{-2} (figure 2.10a). Time dependent reflectivity was used to estimate the carrier lifetime in the implanted silicon and required the use of two decaying exponentials to fit the data rather than the single exponential in SOS. The time constant of the first fitted exponential, the fast component, is shown as a function of dose in figure 2.10b and comprises 80% of the observed signal whilst the second exponential has a slower decay time, 10 ± 2 ps over the whole dose range. The first component is from the heavily implanted polycrystalline silicon whilst the second originates from the lightly implanted/undamaged substrate and does not contribute to the receiver current because of the insulator layer. Figure 2.10b shows that a minimum carrier lifetime of 550 ± 50 fs is observed for doses between 5.10^{14} and 10^{16} cm^{-2} which is comparable to if not slightly better than carrier lifetimes observed in implanted SOS. Consequently the SiOSi receiver antennas, fabricated in

the same fashion as the SOS antenna, were implanted with a dose of $10^{15}cm^{-2}$. A 10 μm dipole SiOSi antenna was tested as the receiver. Because of the 0.57 mm increased thickness of the SiOSi substrate over the SOS it was necessary to use a shorter silicon hyper-hemispherical lens such that the dipole remained at its focus. A critical factor for a receiver's performance is the noise level. In the absence of laser illumination the SiOSi chip exhibited a noise current of 100 fA/√Hz in the region from 100 Hz to 10 KHz. This compares with a level of 30 fA/√Hz for the SOS device. Illuminated noise levels were considerably higher and typically were ~ 300 fA/√Hz for both antennas over the same frequency range, reflecting the different noise sources. In the dark thermal (Johnson) noise dominates and under illumination the laser is the primary source of noise[1]. The larger Johnson noise of the SiOSi chip probably reflects the thicker active silicon layer. Under the same line focus transmitter and receiver gating powers as before the detected amplitude rose by a further factor of two when compared with the SOS receiver. A similar increase was found for receivers with 30 μm dipole lengths. In comparison the sensitivity of LT GaAs receivers is estimated as 5 or 6 times that of SOS antennas[34], such antennas appear to be considerably noisier however[2]. Both SiOSi and SOS receivers had been stripped to reduce Johnson noise[1], by SF_6:O_2 plasma etching from all but a 50 μm wide stripe containing the dipole antenna.

2.3.5 Combined Enhancement Measurements

Combining the advances of sections 2.3.1, 2.3.3 and 2.3.4, broad band performance for the spectrometer is obtained with a combination of appropriate excitation beam polarisation, distributed line focus of the stripline transmitter and the use of a 10 μm SiOSi dipole receiver. Figure 2.9 shows a plot of peak receiver current against transmitter electrical bias for just such a combination. A peak receiver current of 45 nA was obtained with 80 mW average beam power and 70 V electrical bias at the transmitter striplines. This rose to 54 nA for 180 mW at 60 V bias (figure 2.8). In both cases the maximum bias was limited to keep the average illuminated current through the transmitter below 3 mA. This somewhat arbitrarily

chosen current resulted in approximately equal optical and electrical thermal loads on the transmitter. The transient strength of 54 nA was believed to be a record at the time of measurement for a SI GaAs stripline emitter and 10 μm dipole receiver. The bandwidth is comparable to that of the point focus excitation and SOS receiver combination, with a peak at 0.9 THz and $f_{0.1}$ at 3.15 THz (inset figure 2.12). This spectral distribution is very little affected by reducing the transmitter power to 2.2 mW or by varying the bias between 5 V and 100 V. This pulse is believed to be comparable in strength, but significantly wider in bandwidth, than the 500 nA transients generated and detected in the all LT GaAs system[2], taking into account the greater sensitivity of the LT GaAs receiver.

The increased amplitude resulting from line excitation allowed the use of a room temperature bolometer to measure the emitted power. A calibrated diamond window Golay cell, assumed to have a uniform responsivity from visible to THz wavelengths[35], was placed in the position of the receiver hyperhemispherical lens. Using 80 mW of distributed transmitter excitation, a signal proportional to the square of the THz field was measured. Scanning the cell revealed that the THz power was distributed in an approximately Gaussian beam, with a $1/e^2$ power radius of 4.5 ± 0.5 mm. When the measured power was corrected for the detector's 3.5 mm window diameter, a total beam power of 16 μW is obtained for a bias of 60 V. This power corresponds to a peak SOS receiver current of 14 nA, and thus to a "sensitivity" of 4 $\mu A/W^{1/2}$. A factor of two error in this quantity is estimated, given the accuracy of the Golay cell calibration, its assumed wavelength independence and the variation between nominally identical SOS receivers[36]. The above relation is thus in reasonable agreement with the estimate of van Exter and Grischkowsky of 15 $\mu A/W^{1/2}$ [1]. Furthermore, the radiated THz power can be increased to 30 μW by raising the transmitter excitation to 170 mW, figure 2.13. In contrast an average power of 2.7 μW from a singular electric field emitter on LT GaAs with 20 mW excitation has been estimated using free space electro-optic sampling[22]. To ensure the signal from the Golay cell was the result of a THz transient and not laser heating of the

transmitter, the Ti:Sapphire laser was operated in CW mode in which case there was no apparent signal above the noise level.

2.4 THz Interferometry

The combined enhancements of section 2.3.5 led to the widest bandwidth so far achieved with our spectrometer. The factor limiting the instrumental bandwidth is the finite response time of the receiver antenna. However, increased bandwidth can be achieved by eliminating the photoconductive dipole receiver and measuring the cross correlation of two similar THz sources with a power detector instead. Ralph & Grischkowsky combined the emission from two GaAs CPS transmitters by using a silicon plate beamsplitter and subsequently detected the THz radiation power with a liquid helium cooled bolometer[37]. The interferogram was generated by varying the delay between the two visible exciting pulses. Single beam powers were up to 20 nW and the spectrum peaked at 1.5 THz with one hundredth of the peak power at frequencies of 0.3 THz and 4.7 THz. As a higher frequency extension of these methods, interferograms of co-linearly propagating ultrashort mid-infrared transients were obtained by Bonvalet *et al.*[38] without the need of a mid-IR beamsplitter. In this case the infrared radiation was emitted when above bandgap 15 fs pulses were focused separately onto a bulk GaAs source and a GaAs/AlGaAs heterostructure along the same radiative axis.

In order to characterise a transmitter and dipole receiver a single chip dual pulse source was used to form an interferometer without the need for a FIR beamsplitter. However, obtaining a strong THz transient from this type of transmitter requires that it is operated in a saturated regime with respect to the incident power. Thus little increase in the single pulse THz strength could be expected from two temporally coincident laser pulses. A partial solution is to excite at separated points along the stripline whilst still remaining within the ~ 50 μm focal region of the THz optical system. An inherent problem is that the first laser pulse partially discharges the transmission line, causing a reduction in the potential seen by the plasma generated by the subsequent pulse. This can be compensated for by appropriate

positioning of the foci with respect to the stripline, allowing stable, delay independent, THz pulse pairs to be generated for one polarity of the delay. However, an exchange of field strength between the transients, accompanied by a distortion in pulse shapes, occurs on passing though the point of zero delay. This crosstalk renders the source unsuitable for use in an interferometer.

Hence a new transmitter design was investigated with the aim of reducing inter-pulse coupling (figure 2.11). Each of the central two conductors could be independently positively biased with respect to the common ground of the outer lines. A Michelson interferometer, with one mirror driven by a stepper motor, was used to create the two 20 mW exciting beams. These were focused to excite ~ 100 μm × 5 μm areas of the high field region next to the outside edges of the two inner conductors. This results in radiated fields of opposite polarity, as the photoelectrons are accelerated in opposite directions.

Figure 2.12 shows THz signals detected by a 10 μm silicon-on-sapphire receiver gated with an average power of 22 mW. The central line shows the almost complete cancellation of the field at the receiver obtained for temporally coincident transmitter excitation. This was achieved by tuning the bias applied to the two centre lines, 40 V and 46 V being the actual potentials used. At these biases average photocurrents were ~ 0.8 mA. In addition an older, 2 electrode stripline transmitter was also tested for comparison (figure 2.11). This transmitter was edge illuminated both above and below the positively biased stripline. The high degree of cancellation can be estimated by summing the squares of the individual data points in each trace, this numerical integration representing the pulse energy incident on the receiver. A ratio of 284±4 to 1 is obtained with the 4 electrode transmitter when the six traces with THz pulse separations ≥ 5 ps are compared to that obtained at zero delay (figure 2.12). The low variation in the ratio also indicates that a constant radiated power can be expected at pulse separations of 5 ps and above. The numerical integration of receiver current from the 2 electrode transmitter resulted in a ratio of 295±25 to 1 under similar conditions. As expected, the 2 electrode design is more susceptible to crosstalk which affects the baseline of the interferogram but the ratio close to zero delay was of 320 to 1. This higher degree of cancellation leads to a

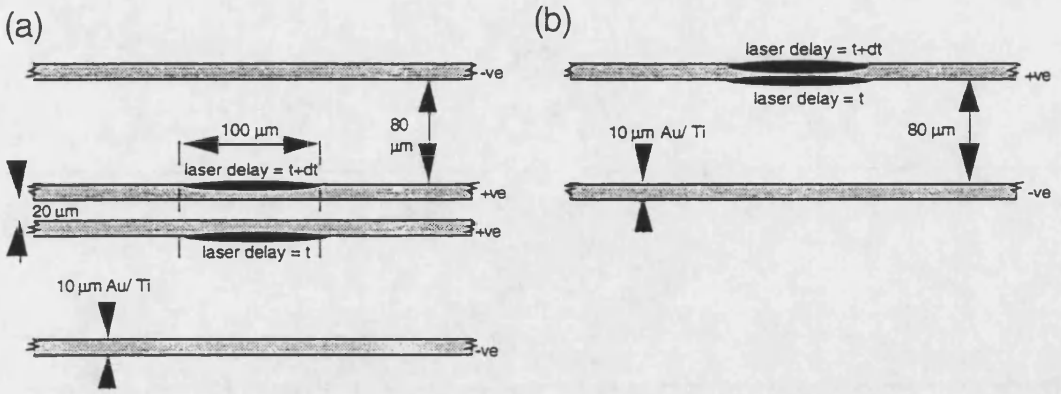

Figure 2.11: Schematic drawing of electrode patterns for dual source using (a) 4 electrode and (b) 2 electrode coplanar stripline transmitters

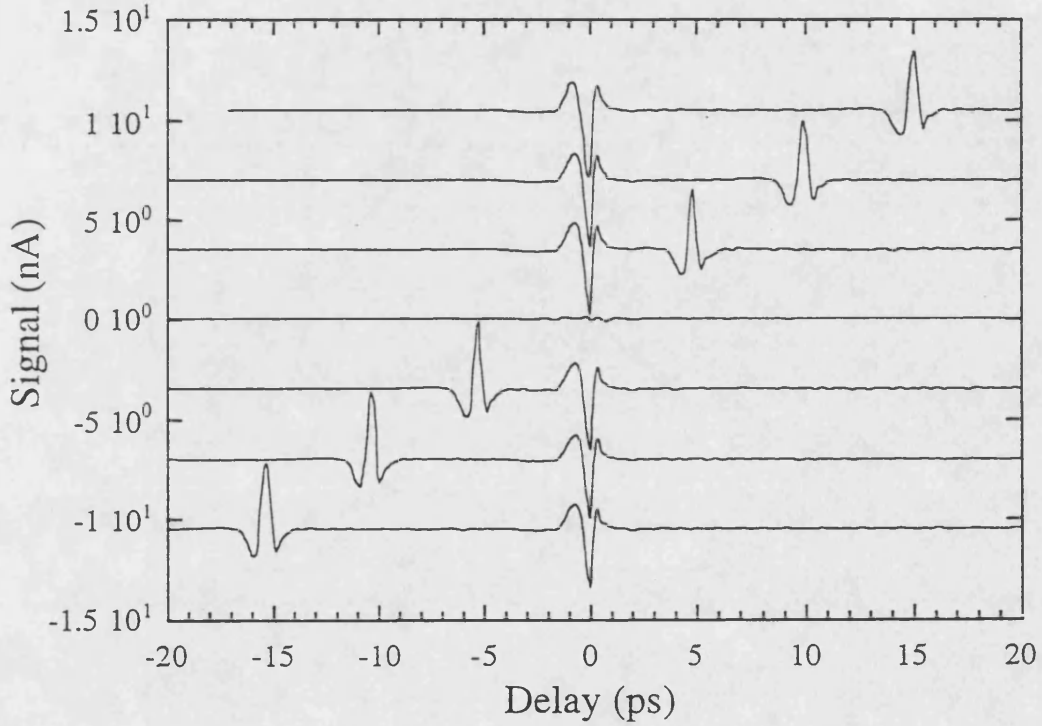

Figure 2.12: THz transients detected by a 10 µm SOS dipole receiver, following dual excitation of a four conductor stripline transmitter with two 70 fs, 765 nm laser pulses. Exciting pulse separations were changed by 5 ps between adjacent traces, which have been separated by 3.5 nA for clarity. The middle trace shows the almost complete cancellation of fields at the receiver position for zero delay between the laser pulses.

sharper interferogram and allows a more accurate determination of the transmitted spectrum. This reflects the systems major limitation in that the mechanical tuning of the pulses (i. e. adjustment of mirrors and lenses) was performed in the time domain with a dipole receiver such that the two pulses were as large and as similar as possible. With the stepper motor driven delay line the interferogram could not be visualised in real time and hence mechanical tuning of the peak could not be performed. Thus although the four electrode transmitter is the superior design by virtue of reduced crosstalk, fulfilling its primary design requirement, it is simple chance that the 2 electrode emitter was better aligned. Consequently the interferometric measurements were made using the 2 electrode emitter.

In order to obtain a power interferogram, a Golay cell was substituted for the receiver and its associated hyper-hemispherical silicon lens. Unfortunately the device has a very limited bandwidth, requiring a low chopping frequency and long integration times. For measurements a frequency of 8.3 Hz with a 0.25 Hz bandwidth were used. An interferogram, obtained by averaging four slow scans of the Michelson delay, is shown in figure 2.13. A peak power of approximately 10 μW was measured, about 1000 times that previously reported for a CPS interferometer[37] which is attributed to the improved line focus transmitter, the absence of a FIR beamsplitter and improved collection of the THz beam with off-axis parabolic mirrors. The noise level on the interferogram base line was primarily determined by laser power fluctuations. The rather high noise on the interferogram baseline arises from the increase in laser fluctuations at low frequencies. A rms noise level of ~ 10 nW was measured from a single scan with the laser blocked.

To obtain the amplitude spectrum in figure 2.14 the base line of the interferogram was first set to zero, Fourier transformed, square rooted and finally normalised. The peak response is at 1.35 THz with $f_{0.1}$ at 4.3 THz. The dipole receiver current depends on the convolution of the THz transient with the receiver's response. To find the receiver's response one divides the transient amplitude spectrum obtained using the dipole receiver with that obtained from the interferogram. The two spectra together with the calculated response are normalised and displayed in figure 2.14. The spectrum from the dipole receiver has a narrower

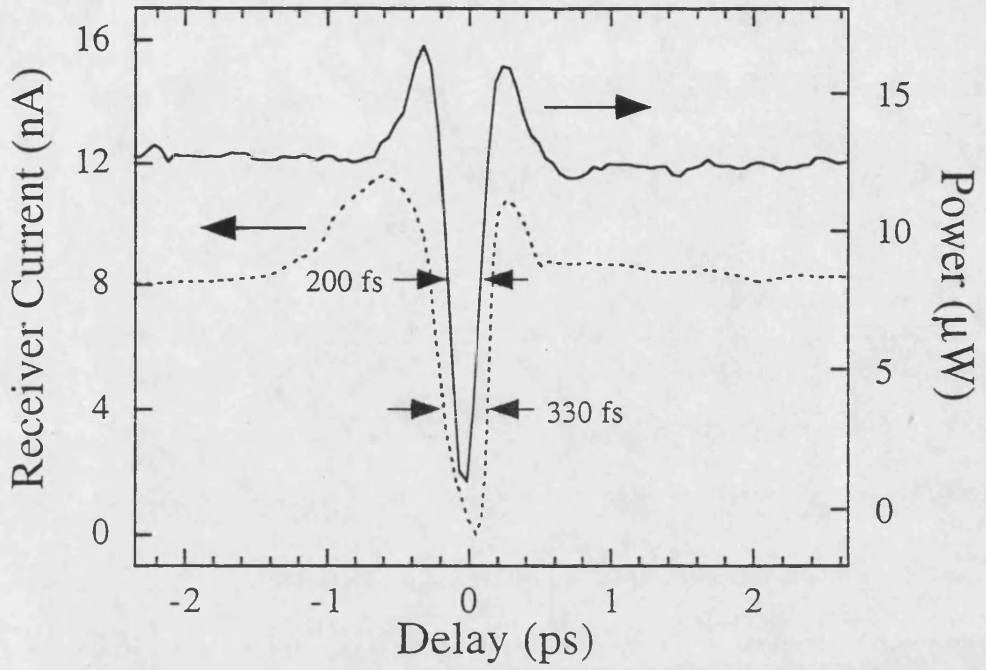

Figure 2.13: Interferogram (solid line) resulting from the bolometric detection of transients, similar to those in figure 2.12, from a two electrode transmitter. An average of four slow scans is displayed. A single transient from the transmitter detected by a 10 μm SOS dipole receiver (dashed line) is shown for comparison.

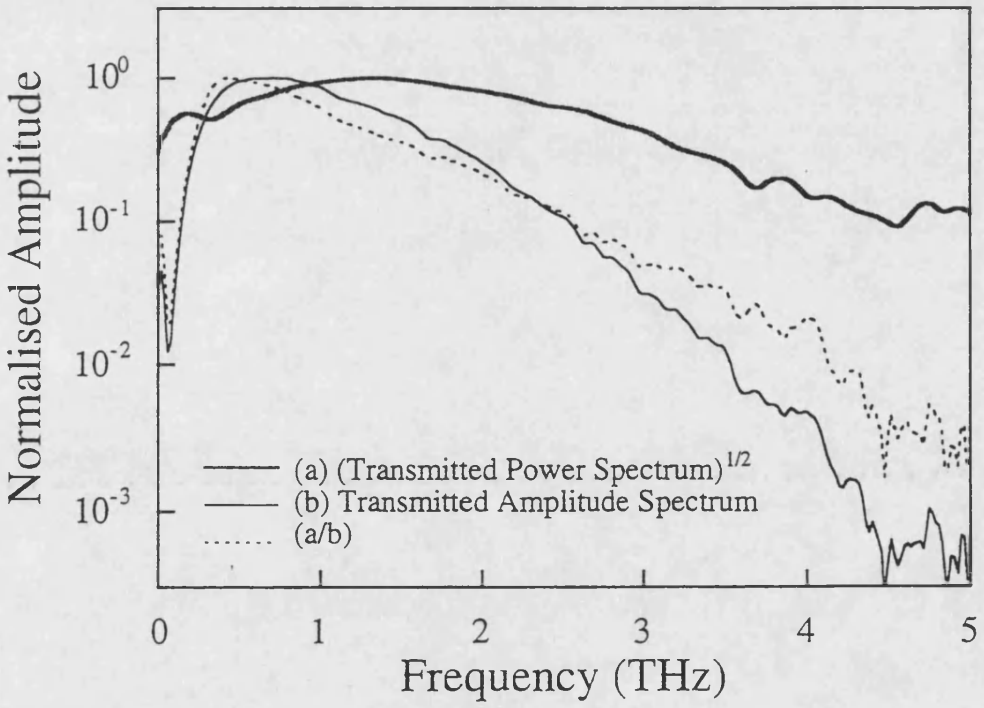

Figure 2.14: Fourier transforms of the traces shown in figure 2.13. The distribution of energy from the interferogram (a) is similar to that obtained using a 10 μm SOS dipole receiver (b) with a peak at 1.35 THz and 1% of peak power at ~ 4.3 THz. The calculated spectral response of the receiver is also shown (a/b).

bandwidth than that obtainable for single transients, a trade off in the alignment to ensure the twin pulses were as alike as possible, with a peak at 0.65 THz and $f_{0.1}$ at 2.0 THz. The response curve maximum is at 0.56 THz with $f_{0.1}$ at 2.58 THz. Thus at the peak strength of the THz transient the dipole antenna is at ~ 45% of its peak efficiency. The distribution of energy from the interferogram is however, roughly similar to that obtained using a 10 μm SOS dipole receiver.

It is believed that the difficulty of alignment using the step and average approach hindered the accuracy of these measurements. In particular, the failure of the main spike to reach zero at zero delay (figure 2.13) indicates that incomplete field cancellation occurred, as was expected from the dipole receiver results. Repeating the experiment with a rapid scanning delay line in the Michelson interferometer and using a faster detector should deliver significantly improved results. Firstly, increased ease of alignment would allow the apparatus to be aligned for minimum interferogram width and hence greatest bandwidth. Secondly, lower baseline noise is obtained using the rapid scan technique.

2.5 Summary

The above investigations have shown that the strength of THz transients emitted from edge illuminated striplines on SI GaAs depend strongly on the polarisation of the excitation beam, with contrast between orthogonal polarisations increasing with illuminated intensity. Silicon-on-sapphire dipole receivers also show a strong dependence of the sensitivity on the excitation polarisation. An explanation based on the initial distribution of photocarriers is proposed in both cases. This also accounts for previously unexplained differences between the polarisation sensitivities of metal/semiconductor/metal photoconductors. The excitation of transmitters with pointed anodes results in an increase in amplitude, but at the expense of bandwidth. However, the use of appropriate excitation beam polarisation together with a distributed line focus of the transmitter allows the creation of THz beams with up to 30 μW of power without any reduction in spectral bandwidth. By using a silicon-on

silicon receiver we have obtained an increase in signal of two orders of magnitude which permits the investigation of samples previously too opaque to study.

The bandwidths of a CPS transmitter and dipole receiver have been characterised with a single chip dual pulse source THz interferometer. Pairs of THz transients were generated from a single coplanar stripline emitter, their separation being determined by the spacing of the near infrared femtosecond laser pulses used to excite the transmitter. A new type of transmitter was developed for this purpose which was less susceptible to crosstalk between the pulses compared with the common CPS design. Average THz powers of ~ 10 μW were measured compared with 30 nW previously reported for a CPS interferometer[37]. The radiated spectrum was found to overlap with the receiver response although their spectra peaks were separated by ~ 0.8 THz. It is believed that considerably better performance would be obtained by using a faster detector and rapidly scanned delay.

References

(1) M. van Exter and D. Grischkowsky, IEEE Trans. Microwave Theory Tech. **38**, 1684 (1990)

(2) I. Brener, D. Dykaar, A. Frommer, L. N. Pfeiffer, J. Lopata, J. Wynn, K. West and M. C. Nuss, Optics Lett. **21**, 1924 (1996)

(3) D. R. Dykaar, B. I. Greene, J. F. Federici, A. F. J. Levi, L. N. Pfeiffer and R. F. Kopf Appl. Phys. Lett. **59**, 262 (1991)

(4) M. Hangyo, S. Tomozawa, Y. Murakami, M. Tonouchi, M. Tani, Z. Wang and K. Sakai IEEE Transactions on Applied Superconductivity **7**, 3730 (1997)

(5) N. Katzenellenbogen, Hoi Chan and D. Grischkowsky, Proc. Ultrafast Electronics and Optoelectronics Conf. (Opt. Soc. Am., Washington, 1993), p. 123

(6) J. Zeilbauer and M. Wegner, Appl. Phys. Lett. **68**, 1223 (1996)

(7) N. Katzenellenbogen and D. Grischkowsky, Appl. Phys. Lett **58**, 222 (1991)

(8) S. E. Ralph and D. Grischkowsky, Appl. Phys. Lett. **59**, 1972 (1991)

(9) U. D. Keil, D. R. Dykaar, R. F. Kopf and S. B. Darack, Appl. Phys. Lett. **64**, 3267 (1994)

(10) P. Uhd Jepsen, R. H. Jacobsen and S. R. Keiding, J. Opt. Soc. Am. **B 13**, 2424 (1996)

(11) X.-C. Zhang, B. B. Hu, J. T. Darrow and D. H. Auston, Appl. Phys Lett. **56**, 1011 (1990)

(12) X.-C. Zhang and D. H. Auston, Appl. Phys. **71**, 326 (1992)

(13) C. Waschke, H. Roskos, R. Schwedler, K. Leo, H. Kurz and K. Kohler, Phys. Rev. Lett. **70** 3319 (1993)

(14) W. Sha, A. L. Smith and W. F. Tseng, Phys. Rev. Lett. **74**, 4273 (1995)

(15) B. B. Hu, X. C. Zhang, D. H. Auston, Phys. Rev. Lett. **67**, 2709 (1991)

(16) "Semiconductor Devices: Physics and Technology", M. Sze, Wiley, New York (1985) p. 162&170

(17) Ch. Fattinger and D. Grischkowsky, Appl. Phys. Lett. **54**, 490 (1989)

(18) Y. Cai, I. Brener, J. Lopata, J. Wynn, L. Pfeiffer, J. B. Stark, Q. Wu and X.-C. Zhang and J. F. Federici, Appl. Phys. Lett. **73**, 444 (1998)

(19) F. E. Doany, D. Grischkowsky and C.-C. Chi, Appl. Phys. Lett. **50**, 460 (1987)

(20) M. Vossebürger, H. G. Roskos, F. Wolter, C. Waschke, H. Kurz, K. Hirakawa and K. Yamanaka, J. Opt. Soc. Am. **B 13**, 1045 (1996)

(21) R. P. Auton, Appl. Opt. **6**, 1023 (1967)

(22) Y. Cai, I. Brener, J. Lopata, J. Wynn, L. Pfeiffer and J. Federici, Appl. Phys. Lett. **71** 2076 (1997)

(23) D. Grischkowsky, S. R. Keiding, M. van. Exter and Ch. Fattinger, J. Opt. Soc. Am **B 7** 2006 (1990)

(24) F. Matsushima, H. Odashima, T. Iwasaki, S. Tsunekawa, K. Takagi, J. Molecular Structure **352/353**, 371 (1995)

(25) M. van Exter, Ch. Fattinger and D. Grischhkowsky, Opt. Lett. **14**, 1128 (1989)

(26) M. A. Lampert, Phys. Rev. **103**, 1648 (1956)

(27) S. L. Chuang, S. Schmitt-Rink, B. I. Greene, P. N. Saeta and A. F. J. Levi, Phys. Rev. Lett. **68**, 102 (1992)

(28) W. G. Heitmann and P. M. van den Berg, Can. J. Phys. **53**, 1305 (1975)

(29) N. de B. Baynes, J. Allam, J. R. A. Cleaver, K. Ogawa, I. Ohbu and T. Mishima, *Proc. Int. Symp. GaAs and Related Compounds*, Inst. Phys. Conf. Series No. 136, Chap 5, 337 (1994)

(30) E. H. Böttcher, E. Dröge, D. Bimberg, A. Umbach, H. Engel and M. Collischon IEEE Photonics Tech. Lett. **9**, 809 (1997)

(31) "Semiconductor Devices: Physics and Technology", M. Sze, Wiley, New York (1985), p. 63

(32) S. E. Ralph, S. Perkowitz, N. Katzenellenbogen and D. Grischkowsky, J. Opt. Soc. Am. **B 11**, 2528 (1994)

(33) SiOSi grown at GEC Marconi Materials Technology, Caswell

(34) M. Tani, S. Matsuura, K. Sakai and S. Nakashima, Appl. Opt. **36**, 7853 (1997); M. Tani K. Sakai and H. Mimura, Jap. J. Appl. Phys. Part II -Lett. **36**, L1175 (1997)

(35) J. E. Pedersen, S. R. Keiding, C. B. Sorensen, P. E. Lindelof, W. W. Ruhle and X. Zhou Appl. Phys. **74**, 7022 (1993); H. M. Heiliger, M. Vosseburger, H. G. Roskos, H. Kurz R. Hey and K. Ploog, Appl. Phys. Lett. **69**, 2903 (1996)

(36) "Far-infrared Techniques", M. F. Kimmit, Pion, London (1970), p. 87

(37) A. C. Warren, N. Katzenellenbogen, D. Grischkowsky and J. M. Woodall, Appl. Phys. Lett. **58**, 1512 (1991)

(38) S. E. Ralph and D. Grischkowsky, Appl. Phys. Lett. **60**, 1070 (1992)

(39) A. Bonvalet, J. Nagle, V. Berger, A. Migus, J.-L. Martin and M. Joffre, Phys. Rev. Lett. **76** 4392 (1996)

3 THz Optical Properties of Bulk Semiconductors

3.1 Introduction

Highly doped contact layers are essential to the operation of many electronic and optoelectronic semiconductor devices designed to operate at terahertz frequencies. However, these highly doped layers also lead to undesirable loss and dispersion through free carrier absorption. It is therefore important to be able to predict the far infrared optical properties of such layers in order to optimise the efficiency of existing devices and to aid the design of possible new structures, e.g. THz lasers based on intersubband transitions. Of particular interest are proposals based on the use of highly doped GaAs layers for both charge injection and waveguiding[1].

At low carrier densities, the free electron optical properties of GaAs are reasonably well described within the framework of the Drude model for the conductivity[2]. This semi-classical model provides a simple method of calculating the far infrared optical constants from the carrier concentration and dc mobility. At high carrier densities the strong optical absorption and the low power output of thermal sources makes conventional far infrared transmission spectroscopy in the THz region difficult to perform, even if samples are in the form of thin films. Thus experimental determination of the frequency dependence of the THz conductivity has been difficult. Here, both FIR transmission measurements and the THz Hall effect have been used to verify the use of Drude theory in highly doped GaAs at THz frequencies

3.2 Free Electron Absorption of Doped GaAs

In this section the complex amplitude transmission of THz transients through both n–type and p-type layers has been studied and accurately modelled by assuming a Drude conductivity. The carrier concentrations and mobilities obtained from a fit to the optical data are in good agreement with results from non-optical characterisation methods.

The technique of time domain THz spectroscopy has been used recently to determine the optical constants of moderately doped[3] and high resistivity[4] Si as well as GaAs[5] with a previously unrealisable degree of precision. It has been shown that the Drude model accurately describes the THz conductivity of GaAs for hole densities[5] up to 6×10^{16} cm^{-3} and for electron densities[6] up to 4×10^{16} cm^{-3}, with the latter study performed in reflection mode due to the strong optical absorption. This problem has been circumvented in this work by preparing samples in thin film form, and thus we have been able to apply THz transmission techniques to GaAs with carrier densities between 1×10^{16} cm^{-3} and 2×10^{18} cm^{-3}.

Each epilayer was grown by molecular beam epitaxy (MBE) on high resistivity ($\rho \sim 10^7$ Ωcm) GaAs (100) substrates and doped with either Be (p-type) or Si (n-type). For spectroscopic measurements, two adjacent 5 mm square chips were cleaved from each wafer, one for transmission measurements and the other was wet etched, using a 12 H_2O: 1 HCl: 1 H_2O_2 solution, to remove the doped epilayer in order to provide a reference. In the process a few microns of the substrate were also removed and the propagation of the THz beam through this thickness of air had to be included when calculating the reference transmission. Room temperature carrier densities and mobilities were obtained from four point resistivity and Hall effect measurements. Five p-type layers, with hole densities ranging from 2.4×10^{16} cm^{-3} and 1.8×10^{18} cm^{-3}, and five n-type layers with electron densities between 1.3×10^{16} cm^{-3} and 1.2×10^{18} cm^{-3}, were studied. Table 3.1 presents details of the carrier concentrations, Hall mobilities and epilayer thicknesses[7]. The measured mobilities are typical of high quality epitaxial GaAs films[8]

Sample number	Sample type	Epilayer thickness (μm) error ~ 3%	Carrier density (cm^{-3}) error ~ 5%	Hall mobility (cm^2/Vs) error ~ 5%
1	n	2.50	1.23×10^{16}	6600
2	n	3.21	4.46×10^{16}	6400
3	n	2.29	7.3×10^{16}	5000
4	n	3.87	1.91×10^{17}	4600
5	n	1.93	7.28×10^{17}	3500
6	n	3.95	1.26×10^{18}	2700
7	p	3.07	2.36×10^{16}	420
8	p	2.32	1.03×10^{17}	240
9	p	2.41	3.97×10^{17}	280
10	p	1.93	7.74×10^{17}	190
11	p	1.96	1.77×10^{18}	180

Table 3.1: Sample designations, type, depletion corrected thicknesses, carrier densities and room temperature Hall mobilities of the GaAs samples studied.

A pair of 3.5 cm focal length off-axis parabolic mirrors were used to focus the THz beam through the 4 mm aperture of a sample holder and to recollimate the radiation afterwards. To make the transmission measurements, the sample was placed in the beam waist just behind the aperture and a slow delay line scan was used to obtain the temporal profile of the transmitted transient. The slow delay line offered better temporal precision than the rapid scanning delay, because of quantisation noise in the position measurement, and therefore greater precision in the measurement of the phase of the transmitted transients which is essential in determining the Drude conductivity. To minimise errors due to long term drift in the laser power, ten or more scans were averaged. A maximum delay of 11 ps was used to eliminate time delayed reflections. This resulted in an experimental frequency resolution of

approximately 0.1 THz. Noise on individual scans was below 200 fA r.m.s. compared with typical peak reference currents of 3 nA.

The time domain incident field profiles were Fourier transformed to extract the spectral amplitude and phase information. Figure 3.1 shows the measured amplitude and phase transmission of sample 6 with respect to the corresponding reference. The error bars represent the standard deviation between data sets and the increase in magnitude below 0.3 THz and above 3 THz is as a result of the reduced spectrometer response beyond these frequencies. The relative amplitude transmission has been determined to be ~ 3×10^{-3} between these frequencies, and this corresponds to an error of about ± 5%. This signal to noise ratio, for a sample with a relative power transmission of ~ 3×10^{-3}, demonstrates the effectiveness of the time domain technique in measuring strongly absorbing materials. This 4 μm epilayer was the thickest and most highly doped of the samples with a carrier density of $1.2\times10^{18}cm^{-3}$ and consequently the most absorbing. The relative transmission of the remaining epilayers exceeded 0.2, with a typical error of ±0.01 for frequencies between 0.3 THz and 3 THz. The relative transmission of sample 6 is observed to have a weak frequency dependence, reaching a minimum of about 0.05 at a frequency close to 1.6 THz. In order to model the experimental data, the conductivity of the epilayer was assumed to be Drude-like, which corresponds to the approximation of a single energy independent scattering time[3], τ, which can be related to the dc mobility, μ, by $\mu = e\tau/m^*$. The angular frequency dependence of the complex conductivity, σ(ω), then takes the form

$$\sigma(\omega) = \frac{\sigma_0}{(1 - i\omega\tau)} \qquad (3.1)$$

where

$$\sigma_0 = \frac{Ne^2\tau}{m^*} \qquad (3.2)$$

N is the carrier density and m* the effective carrier mass which varies according to the host material, crystallographic direction (in anisotropic materials)

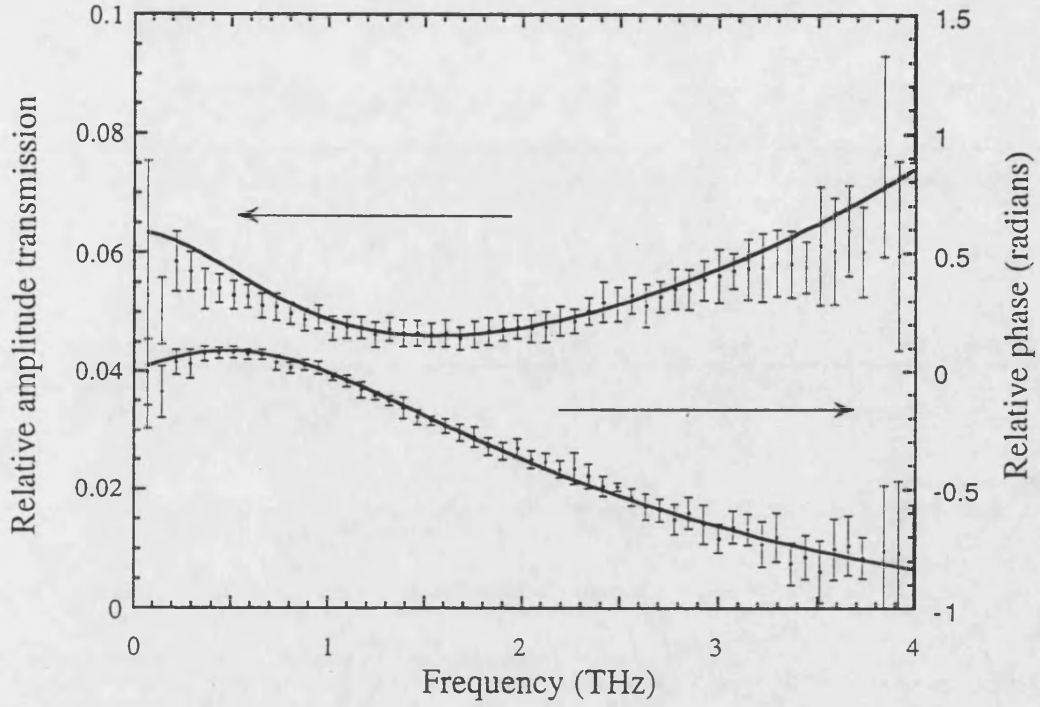

Figure 3.1: THz amplitude and phase transmission, relative to the undoped GaAs substrates, of sample 6, a 3.95 μm thick GaAs film with 1.26×10^{18} electrons cm^{-3}. Points with error bars show experimental data: the solid lines are a Drude model fit.

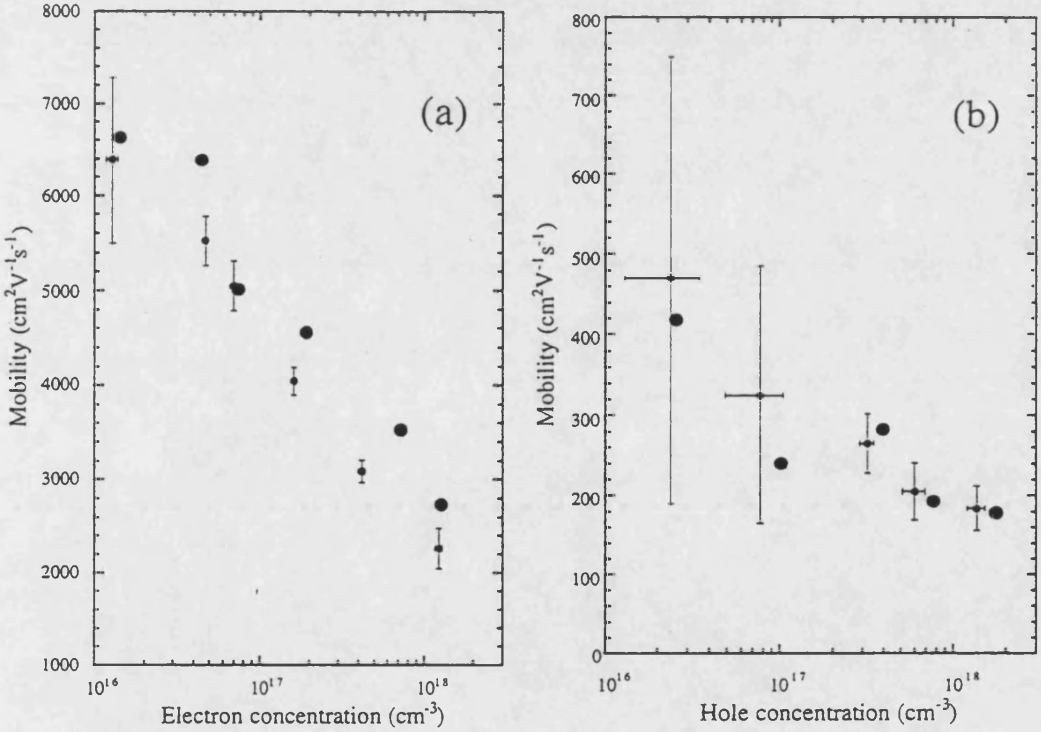

Figure 3.2: Mobility versus carrier density for (a) n-type and (b) p-type GaAs epilayers studied. Solid symbols refer to Hall effect measurements, with the symbol size indicating experimental error. Nearest points with error bars indicate carrier concentrations and mobilities obtained from a Drude fit to the THz transmission data.

and the energy of the charge carrier. The dielectric constant $\varepsilon(\omega)$ is obtained from $\sigma(\omega)$ by

$$\varepsilon(\omega) = \varepsilon_{GaAs} + i\sigma(\omega) / \omega\varepsilon_0 \qquad (3.3)$$

The expression $\varepsilon_{GaAs} = 12.9 + (7.9\times10^{-28})\omega^2$ is used to describe the weak dispersion of the dielectric constant of undoped GaAs associated with the transverse optical phonon at 8.1 THz[4.9]. From equations 3.1-3.3 the complex amplitude transmission of the two layer system is calculated[10] using the refractive indices of the substrate and epilayer, the thickness of the epilayer and the etch depth d_{etch}. The complex amplitude transmission is then divided by the calculated reference transmission to obtain relative amplitude and phase values to compare with experiment. The fitted curves in figure 3.1 show that the model provides a good description of the experimental data. Fits of similar quality were obtained for the other samples studied. The variable parameters, N, τ and d_{etch} were optimised in the fitting procedure. The latter parameter took into account possible slight variations in wafer thickness between sample and reference.

Figure 3.2 displays the calculated mobilities obtained from the scattering time, τ, as functions of the electron and hole densities and compares them with the results of non-optical measurements.

In general the carrier concentrations for the n-type epilayers agree well but the optically determined mobilities underestimate the Hall data by an average of 10%. To determine whether this error was linked to errors in the value of the epilayer thickness, the thickness parameter was varied by up to ±30% in the calculations. Within this range the fitted N was found to increase when the layer thickness was decreased. Conversely the mobility changed by less than 5%, implying the discrepancy is not due to uncertainty in the value of the layer thickness. A previous THz study of n-GaAs[5] with $n = 7.8\times10^{15}cm^{-3}$ found good agreement between optically determined Hall mobilities by assuming the low density, low temperature limit $m^*=0.067\ m_0$, where m_0 is the free electron mass. Band non-parabolicity leads to a dependence of m^* on N[11]. Values used ranged from $0.064\ m_0$ for sample 1 to

0.079 m_0 for sample 6. Including non-parabolicity effects suggests that $m^* = 0.072\ m_0$ should have been used by Katzenellenbogen and Grischkowsky[5], with the result that their THz measurement would underestimate μ by about 10%. It is thus concluded that the optically determined mobility is systematically less than the Hall mobility. This observation is also supported by infrared reflectivity studies of bulk n-GaAs with similar electron concentrations to the epilayers studied here[12]. This underestimate is attributed to the fact that the optical measurement determines the drift mobility, μ_d, which is related to the Hall mobility, μ_H, by the Hall factor[13] $r_H = \mu_H/\mu_d$. The Hall factor accounts for the finite spread of scattering times with carrier energy in a real semiconductor and is defined by $r_H = \langle\tau^2\rangle/\langle\tau\rangle^2$, the magnitude of which depends on the scattering mechanisms involved. For n-GaAs at 300 K, theoretical and experimental r_H values[13] are in the range from 1.0 to 1.2 which is consistent with the mobility ratios observed.

A fixed density of states effective hole mass of 0.34 m_0 was assumed when fitting the THz data for the p-type epilayers[14] (Figure 3.2b). The lower hole mobility gives rise to reduced absorption and larger uncertainties than in the n-layer fits. In the most lightly doped samples (7 and 8) the amplitude transmission exceeded 90% so that considerably increased layer thicknesses would be necessary to obtain appreciable absorption. The agreement between the parameters determined by the optical and transport methods is in general good although the optical method would appear to slightly underestimate the hole density whereas optical and Hall mobilities agree well i.e. $r_H \sim 1$. Similar good agreement was found in a previous THz transmission study on bulk p-GaAs[5] with $p = 6\times10^{16}cm^{-3}$. This agreement is in conflict with recent infrared reflectivity studies on epilayers of highly doped p-GaAs[15] in the frequency range from 6 THz to 30 THz, where fits to the data gave $r_H \sim 2$. Both experimental results are in fact within the range of current theoretical values[14,15] of r_H: $1.25 \le r_H \le 2.3$.

3.3 The THz Hall Effect in a Doped GaAs Epilayer

The Hall effect together with resistance measurements provides a simple method of determining carrier sign, density and mobility. In the previous section the Drude model was verified for highly doped samples at THz frequencies but it is also possible to use the Hall effect in the FIR. The motion of charges within an isotropic homogeneous semiconductor in crossed electric (E) and magnetic fields (B) is well described by

$$\frac{d\underline{p}}{dt} = e\underline{E}(\omega) + \frac{e\underline{p}}{m^*} \times \underline{B} - \frac{\underline{p}}{\tau} \qquad (3.4)$$

where $\underline{p}$ represents the momentum vector. A current is induced in a material containing free charges when it is illuminated with plane polarised FIR radiation via the longitudinal conductivity tensor: $J_x = \sigma_{xx}E_x$. In the presence of a magnetic field, parallel to the direction of the FIR beam, a perpendicular Hall current is also induced through the transverse conductivity tensor: $J_y = \sigma_{yx}E_x$. The Hall effect results in different transmission coefficients for left and right circularly polarised radiation, i.e. the Faraday effect. From equation 3.4 the conductivity tensor elements are given by

$$\sigma_{xx}(\omega) = \frac{\sigma_0(1-i\omega\tau)}{(1-i\omega\tau)^2 + (\omega_c\tau)^2} \qquad (3.5)$$

$$\sigma_{xy}(\omega) = \frac{\sigma_0(\omega_c\tau)}{(1-i\omega\tau)^2 + (\omega_c\tau)^2} \qquad (3.6)$$

where $\omega_c = eB/m^*$, is the cyclotron frequency. Both components of the current radiate in the FIR and the transmission spectra can be used to determine the full conductivity tensor of the sample. Spielman *et al.*[16] have previously applied this technique to $YBa_2Cu_3O_{7-x}$ superconductor and Waleki et al. have attempted to study the THz quantum Hall effect in an GaAs/AlGaAs 2DEG[17]. Again, to test the validity of the Drude model at THz frequencies the carrier density and mobility may be determined

from the conductivity within a semiclassical Drude model and compared with transport measurements. Such measurements have been performed on sample 4 of the n-type epilayers in table 3.1 and the results for the carrier density are in good agreement with transport values in section 3.2, whilst the mobility was determined with less accuracy. In contrast to the complex amplitude transmission method this approach is not as sensitive to the phase of the transmitted radiation and a rapid scanning delay line could be used to reduce errors originating from long term drift of the laser power. The angular rotation of the transmitted THz radiation, which is related to the Hall angle in contact transport methods, was measured. TE and TM were defined with electric vector perpendicular and parallel to the receiver dipole axis. To measure the rotation of the plane polarised THz radiation the post sample polariser was set at 45 degrees clockwise or anticlockwise to the TE plane (labelled +45 and -45 respectively). These polarisations are symmetrical about the receiver dipole axis and account for the inherent polarisation sensitivity of the receiver. The relative TE and TM components were calculated from the sum and difference of the two transmitted polarisations respectively. In figure 3.3 the transmission spectra through the sample at various magnetic fields is shown. There is a clear increase in signal strength for t_{+45} at the expense of t_{-45} with increasing field in figure 3.3. At zero field the hyperhemispherical lens of the receiver was positioned so as to approximately equalise the transmitted amplitudes from both polarisations. Small differences between t_{+45} and t_{-45} were corrected by normalising the +45° spectra at finite magnetic fields to the -45° spectra at zero field such that

$$t_{+45n}(B) = \frac{t_{+45}(B)t_{-45}(0)}{t_{+45}(0)} \qquad (3.7)$$

THz Hall effect measurements have been performed previously in attempts to develop non contact methods of determining semiconductor transport parameters but only at singular frequencies[18,19]. A central assumption of Drude theory is an energy independent momentum relaxation time. Therefore estimating the carrier mobility as a function of frequency is useful in verifying the theory's validity. In order to model the transmission spectra electromagnetic boundary conditions can be applied at the

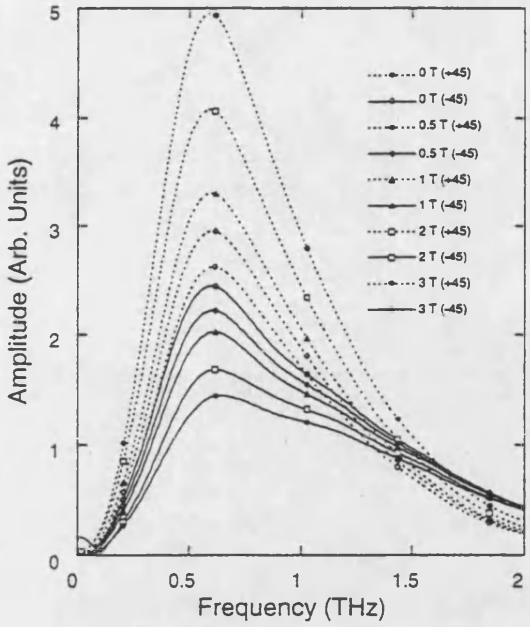

Figure 3.3: Uncorrected transmission spectra sample 4, a 3.87 μm thick GaAs film with 1.91×10^{18} electrons cm^{-3}. Polarising analyser orientation and magnetic fields as indicated

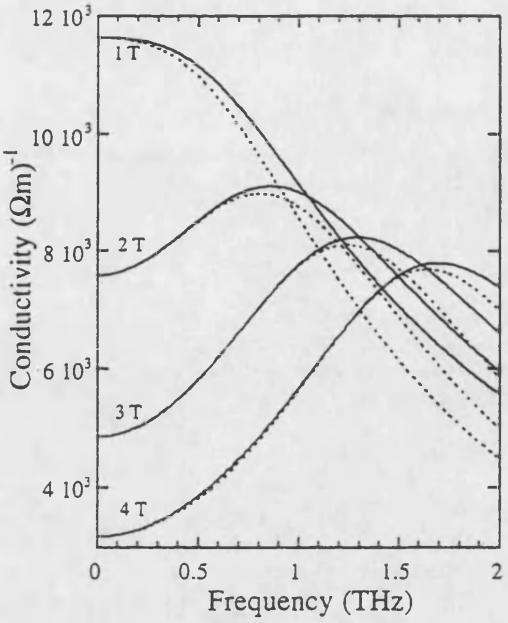

Figure 3.4 Drude predicted values of $|\sigma_{xx}|$ for sample 4, from transport values for carrier density and mobility (solid curves). The dashed curve is calculated from the same parameters taking into account the assumptions in the text.

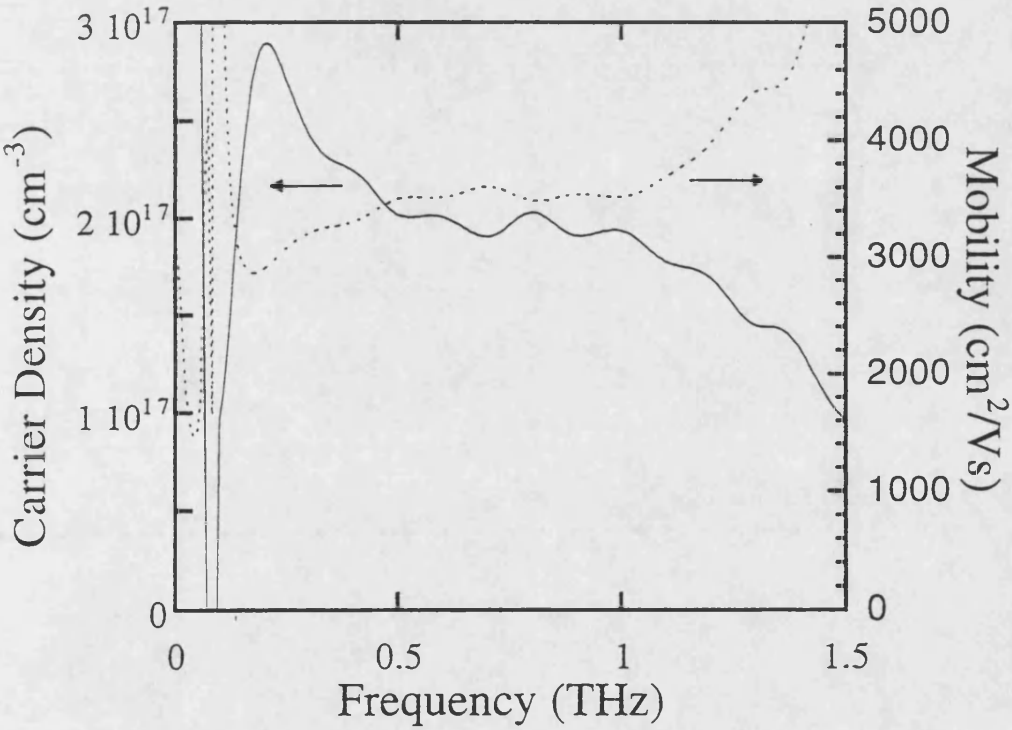

Figure 3.5: Values of carrier density (solid curve) and mobility (dashed curve) for sample 4, obtained from transmission spectra at 3 T. Only the level, central portion of the traces (0.5-1.1 THz) is reliable.

interface to relate the incident ($\underline{E_I}$), reflected ($\underline{E_R}$) and transmitted ($\underline{E_T}$) electric fields, such that:

$$\underline{E}_I + \underline{E}_R = \underline{E}_T \qquad (3.8)$$

and

$$\frac{\underline{B}_I}{\mu_0} - \frac{\underline{B}_R}{\mu_0} - \frac{\underline{B}_T}{\mu_0} = \underline{\underline{\sigma}}(\underline{E}_I + \underline{E}_R)d \qquad (3.9)$$

where the time dependence of the electrical displacement is considered to be negligible, $\underline{\underline{\sigma}}$ represents the conductivity tensor and d is the epilayer thickness. Combining equations 3.8 and 3.9 and using the relation $B = nE\mu_0/Z_0$, where Z_0 is the impedance of free space and n the frequency dependent refractive index of undoped GaAs[4], one obtains expressions for the field transmission coefficients:

$$t_{TM} = \frac{E^{out}(\omega)}{E^{in}(\omega)} = \frac{4ne^{i\theta}}{(n+1)} \frac{\left(1+n+\sigma_{xx}Z_0d\right)}{\left(\left(1+n+\sigma_{xx}Z_0d\right)^2 + \left(\sigma_{xy}Z_0d\right)^2\right)} \qquad (3.10)$$

$$t_{TE} = \frac{E^{out}(\omega)}{E^{in}(\omega)} = \frac{4ne^{i\theta}}{(n+1)} \frac{\sigma_{xy}Z_0d}{\left(\left(1+n+\sigma_{xx}Z_0d\right)^2 + \left(\sigma_{xy}Z_0d\right)^2\right)} \qquad (3.11)$$

E^{out} (E^{in}) refers to the transmitted THz field measured with (without) the sample in place and $\theta(\omega)$ represents the phase shift due to propagation through the substrate. The longitudinal and transverse conductivities can be expressed in terms of the transmission coefficients:

$$\sigma_{xx} = \frac{1}{Z_0 d}\left[\frac{4ne^{i\theta}}{n+1}\frac{t_{45}+t_{-45}}{t_{45}^2+t_{-45}^2} - n - 1\right] \qquad (3.12)$$

$$\sigma_{xy} = \frac{1}{Z_0 d}\left[\frac{4ne^{i\theta}}{n+1}\frac{t_{-45}-t_{45}}{t_{-45}^2+t_{45}^2}\right] \qquad (3.13)$$

To derive σ_{xx} and σ_{xy} both amplitude and phase spectra are required. The phase portion of the data is the most sensitive and errors quickly accumulate in the calculation of equations 3.12 and 3.13. However only $|\sigma_{xx}|$ and $|\sigma_{xy}|$ are required to calculate N and μ, greatly reducing the dependence on the phase portion of the signal. In the case of $|\sigma_{xy}|$ the complex spectrum is only required for the initial solution of the transmissivity denominator and numerator, the subsequent separation of phase and magnitude in the expression being trivial. The subtraction of the factor (n+1) in $|\sigma_{xx}|$ prevents one from making the same simplification, however if the assumption is made that the imaginary portion at this stage of the calculation is negligible one may proceed as before. The price paid for this assumption is a limitation on the accuracy over some values of field and frequency. Using the parameters from the transport data, $|\sigma_{xx}|$ was predicted from equations 3.5 and 3.6 with and without the above assumption for different fields as shown in figure 3.4. The error in $|\sigma_{xx}|$ is < 10% between 0 T and 4 T for frequencies between 0 THz and 2 THz. The best agreement is at ~ 3 T, with an error <0.5 % for frequencies up to 1.3 THz.

Combining equations 3.1 and 3.2 with equations 3.10 and 3.11 expressions for N and μ can be obtained:

$$\mu = \frac{e}{m^*}\left[\left(\omega_c \frac{|\sigma_{xx}|}{|\sigma_{xy}|}\right)^2 - \omega^2\right]^{-1/2} \qquad (3.14)$$

$$N = \frac{|\sigma_{xy}|B}{e}\left[\left(\frac{|\sigma_{xx}|}{|\sigma_{xy}|}\right)^4 + 2\left(\frac{|\sigma_{xx}|}{|\sigma_{xy}|}\right)^2 + 1 - 4\frac{\omega^2}{\omega_c^2}\right]^{1/2} \qquad (3.15)$$

Values of N and μ obtained at 3 T using equations 3.14 and 3.15 are shown in figure 3.5. For frequencies between 0.5 THz and 1.1 THz both μ and N are practically independent of frequency, as expected for the carrier density and an

energy independent relaxation time. Outside these frequencies each trace fails to conform to a single value and is most likely due to reduced spectrometer sensitivity. Above 1.3 THz the error in $|\sigma_{xx}|$ increases with increasing frequency (figure 3.4) and most likely adds to the error in N and μ. There is the possibility that mobility does become sensitive to the frequency of the incident radiation above 1.1 THz although more detailed studies would be required to confirm this. Since the carrier density calculation assumes an energy independent relaxation time this might account also for the estimated values of N above 1.1 THz. Within the flat region the average value of the carrier density and mobility are $1.96\pm0.07\times10^{17}$ cm^{-3} and 3540 ± 40 cm^2/Vs respectively, where the errors represent deviation from the mean. The carrier density is in excellent agreement with the transport data whereas the optically determined mobility is 24% lower.

Previous studies of the THz Hall effect have been performed by Clark[19] and Nuss *et al.*[18] on samples similar to the one used here. Using a CO_2 laser (f = 28.3 THz), Clark found a similar agreement of the transport data with N. Nuss *et al.* however, found N to be ~ 20% lower, employing a similar method to that used here but measuring at only 0.9 THz. The main differences between the latter work and these experiments was the use of a 1.3 T permanent magnet which produced a uniform field over only a rather small region. To obtain zero field data the magnet had to be lifted out of the beam, requiring that the sample be de-mounted.

The discrepancy between the THz Hall mobility and that obtained by the transport data is significantly more than the 10% obtained in section 3.2 by analysing the transmission. The THz Hall effect results give a value of ~ 1.3 for the Hall factor, just outside the theoretical and experimental range[13]: $1.0 \leq r_H \leq 1.2$. Clark's mobility results were similarly within 15±8% of the transport data (r_H ~ 1.1-1.3). The estimates of μ given by Nuss *et al.* were over an order of magnitude lower than the transport data. Such a discrepancy is hard to explain in terms of the Hall factor and is perhaps better explained by the difficult experimental conditions experienced by that

group: the need to dismantle the sample between references and a largely non-uniform magnetic field

Attempts were also made to perform similar measurements on a p-type sample (No. 7 in table 3.1) but the rotation of the plane polarised radiation was too small to be measured. In general a significant rotation requires the product $\omega_c\tau$ to be ≥ 1 (e. g. for the n-type epilayer of sample 4 in a field of 3 T, $\omega_c\tau \sim 1.59$). For sample 7 $\omega_c\tau$ is only ~ 0.13 at 3 T.

3.4 Summary

The complex electric field transmission of several doped GaAs epilayers has been measured at frequencies from ~ 0.2 THz to ~ 3 THz and the optical Hall effect measured on one sample between 0.5 THz to 1.1 THz using the technique of time domain spectroscopy. The Drude model can be used to calculate the complex amplitude transmission with good accuracy for carrier densities up to at least 10^{18} cm^{-3}. In the case of p-type epilayers, the deduced carrier densities and mobilities are in good agreement with values obtained from transport measurements. For n-type samples, the electron density agrees well with transport data, but mobilities are slightly smaller than obtained from Hall data. For the one n-type sample studied using the optical Hall effect, the mobility data underestimates the transport data by ~ 20% although the electron density is in good agreement.

References

(1) A. N. Korotkov, D. V. Averin and K. K. Likharev, Appl. Phys. Lett. **65**, 1865 (1994); Q. Hu and S. C. Feng, Appl. Phys. Lett. **59**, 2923 (1991)

(2) "Optical Characterisation of Semiconductors: Infrared, Raman and Photoluminescence Spectroscopy", S. Perkowitz, Academic Press, London (1995), p. 184

(3) M. van Exter and D. Grischkowsky, Appl. Phys. Lett. **56**, 1694 (1990); T.-I. Jeon and D. Grischkowsky, Phys. Rev. Lett. **78**, 1106 (1997)

(4) D. Grischkowsky, S. Keiding, M. van Exter and Ch. Fattinger, J. Opt. Soc. Am. **B 7**, 2006 (1990)

(5) N. Katzenellenbogen and D. Grischkowsky, Appl. Phys. Lett. **61**, 840 (1992)

(6) T. -I. Jeon and D. Grischkowsky, Appl. Phys. Lett. **72**, 3032 (1998)

(7) "Electrical Characterisation of GaAs Materials and Devices", D. C. Look, Wiley, Chichester (1989), p.45

(8) M. Ilegems in "Technology and Physics of Molecular Beam Epitaxy", ed. E. H. C. Parker Plenum, New York (1985), p.121 and p.131

(9) W. J. Moore and R. T. Holm, Appl. Phys. **80**, 6939 (1996)

(10) "Principles of Optics", 4th edn., M. Born and E. Wolf, Pergamon, Oxford, (1970), p.627

(11) D. M. Szmyd, P. Porro, A. Majerfeld and S. Lagomarsino, J. Appl. Phys. **68**, 2367 (1990)

(12) R. T. Holm, J. W. Gibson and E. D. Palik, Appl. Phys. **48**, 212 (1977)

(13) D. C. Look, C. E. Stutz, J. R. Sizelove and K. R. Evans, Appl. Phys. **80**, 1913 (1996)

(14) R. Fukasawa and S. Perkowitz, Phys. Rev. **B 50**, 14119 (1994)

(15) R. Fukasawa, K. Sakai and S. Perkowitz, Japn. J. Appl. Phys. **36**, 5543 (1997)

(16) S. Spielman, B. Parks, J. Orenstein, D. T. Nemeth, F. Ludwig, J. Clarke, P. Merchant and D. J. Lew, Phys. Rev. Lett **73**, 1537 (1994)

(17) W. J. Walecki, D. Some, V. G. Kozlov and A. V. Nurmikko, Appl. Phys. Lett. **63**, 1809 (1993)

(18) D. M. Mittleman, J. Cunningham, M. C. Nuss, M. Geva, Appl. Phys. Lett. **71**, 16 (1997)

(19) F. W. Clark, Appl. Phys. **75**, 4319 (1994)

4 Cyclotron Resonance in Semiconductor Heterostructures

4.1 Introduction

Cyclotron resonance in the 2DEG inversion layer of a Si MOS transistor was first observed by Abstreiter *et al.* and Allen *et al.* in 1974[1] and in a modulation doped AlGaAs/GaAs heterostructure by Störmer *et al.* in 1979[2]. In this chapter the investigation of coherent cyclotron oscillations in various 2DEG's excited by THz transients is described. Historically, CR has proved to be a powerful tool in the study of semiconductors, providing a method for determining the effective electron mass from the cyclotron frequency and the scattering time from the homogeneous broadening of the resonance.

Electron scattering in pure GaAs and Si at room temperature is dominated by interactions with polar optical phonons. Typical scattering times are of the order of tens of femtoseconds, severely damping coherent processes within the temporal resolution of our spectrometer (~ 500 fs). Since optical phonons require energies of tens of meV, their numbers are greatly reduced below ~ 100 K, giving way to Coulomb scattering by ionised impurities as the dominant process (figure 4.1). For these reasons CR experiments were largely restricted to low temperatures, ~ 5 K, eliminating most phonon scattering contributions, and to carrier transport displaced from scattering centres within 2DEGs in modulation doped quantum wells, grown by MBE.

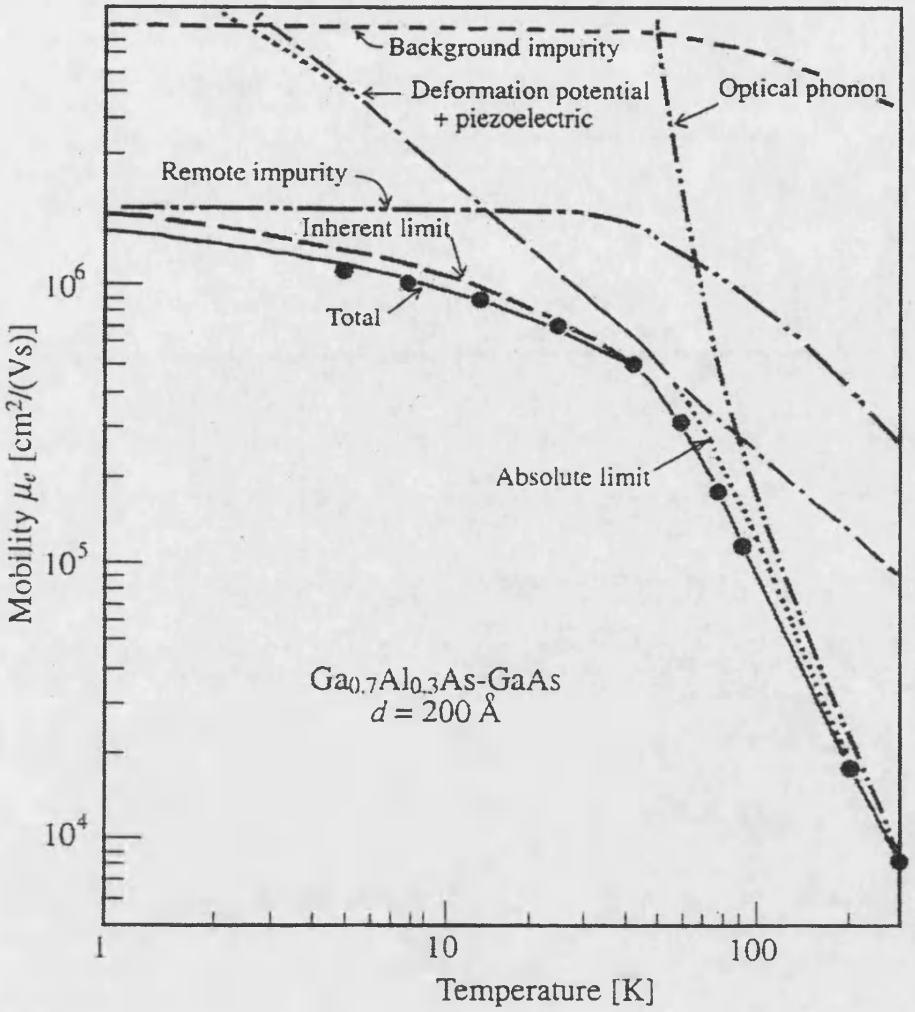

Figure 4.1: Mobility of a two dimensional electron gas in a modulation doped GaAs/$Al_{0.3}Ga_{0.7}As$ heterojunction as a function of temperature. The closed circles indicate experimental results. The various dashed curves are calculated contributions to the mobility from the different scattering mechanisms. The solid curve represents the sum of all those contributions[11].

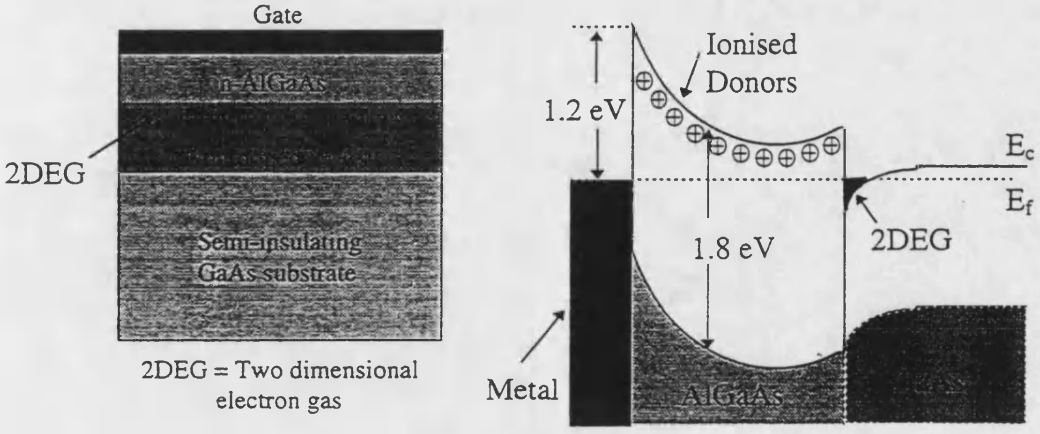

Figure 4.2: A schematic drawing of a modulation doped heterojunction between GaAs and n-$Al_{0.3}Ga_{0.7}As$. E_c and E_f represent, respectively, the conduction band edge and the Fermi energy.

Heterojunctions are grown by highly precise deposition techniques, MBE or metal organic chemical vapour deposition, from two materials with closely matched lattice constants but different bandgaps. This results in abrupt band discontinuities at the interface. The basic concept behind modulation doping, as proposed by Störmer[2], is illustrated in figure 4.2, using GaAs/$Al_xGa_{1-x}As$ as an example. If the $Al_xGa_{1-x}As$ is doped with shallow donors, the Fermi level is shifted from the middle of the bandgap of the $Al_xGa_{1-x}As$ to the donor level. To maintain a constant chemical potential across the heterojunction, electrons flow from the $Al_xGa_{1-x}As$ to the GaAs. The band edges are warped by the resulting potential gradient, confining the electrons in a steep, approximately triangular, potential well in the GaAs at the interface. The well is narrow compared with the Fermi wavelength and electron motion perpendicular to the interface is quantised into well defined, discrete, subbands while parallel transport is relatively unimpeded. This then constitutes a 2DEG separated from the ionised impurities: the modulation doping technique. The approach may be applied equally to quantum wells with $Al_xGa_{1-x}As$ barriers sandwiching a thin GaAs layer resulting in quantised energy levels reminiscent of quantum mechanical text book "particle in a box" examples. In this work CR in modulation doped SiGe/Si and AlGaAs/GaAs heterostructures as a function of magnetic field, temperature and carrier density has been studied.

4.2 GaAs/AlGaAs Heterostructure

The GaAs/$Al_xGa_{1-x}As$ system is a common material choice (figure 4.2), since the lattice constants differ by less than 1%, and its extensive use in the semiconductor industry has lead to very refined growth technology. The bandgap of $Al_xGa_{1-x}As$ (~ 1.8 eV), with less than 40% Al, is direct and larger than that of GaAs (~ 1.5 eV). The difference between the bandgaps is divided into an approximately 60/40 split between the conduction and valence band. Both conduction and valences band edges of the smaller bandgap GaAs lie closer to the Fermi level than they do in the AlGaAs and so the system forms a type I heterojunction.

The sample for these investigations consisted of an MBE grown heterostructure, A1332[3], with two modulation doped GaAs quantum wells each 15 nm wide, separated by a 2.5 nm $Al_{0.3}Ga_{0.7}As$ barrier, figure 4.3, with an average mobility of 8.6×10^5 cm^2/Vs at 1.6 K. A sheet carrier density (N_s) of 8.5×10^{11} cm^{-2} was determined by Shubnikov-deHaas (SdH) measurements[3] of the longitudinal conductivity of an ungated Hall bar test device fabricated from the same wafer. A 5×5 mm^2 thin coating of indium tin oxide was sputtered on to the surface and annealed in forming gas (90% N_2 : 10% H_2) at 400 °C for 4 minutes. This created a semi-transparent, Schottky contact with a sheet resistance of approximately 80 Ω per square at 300 K. Indium was soldered onto the surface of the chip to form source and drain ohmic contacts. The sheet carrier density could be varied between effectively zero and 8.5×10^{11} cm^{-2}. This enabled the application of a modulation technique to isolate the 2DEGs response from the much larger transmitted THz signal. The 2DEG was placed at the focus of the THz spectrometer, at the centre of the split coil superconducting magnet, such that the surface normal was co-linear with the magnetic field and incident FIR radiation. The temperature of the sample was monitored using a RhFe resistor on the sample mount and held at 5 K. The sample was illuminated with above bandgap radiation for ~ 60 s to maximise the sheet carrier density via the persistent photoelectric effect[2].

The time varying electric field of the THz transient incident on the sample induces a time varying current in the 2DEG. The circular motion of the cyclotron orbits leads to sinusoidal current oscillations in the linear polarisation sensitive receiver. The trace of differential THz transmission versus delay, figure 4.4, approximately corresponds to the impulse response of the 2DEG in a perpendicular magnetic field. Unless stated other wise, the 2DEG channel carrier density was modulated between zero and ~ 8.5×10^{11} cm^{-2}.

A perpendicular magnetic field modifies the density of states of a bulk electron gas, reducing the allowed volume of states in k-space from a sphere to a series of Landau cylinders. In two dimensions the allowed states in k-space are already quantised into discs which in a magnetic field become annuli with degeneracy eB/h and separated by energies of $\hbar\omega_c$. Only electrons within $\hbar\omega_c$ of the

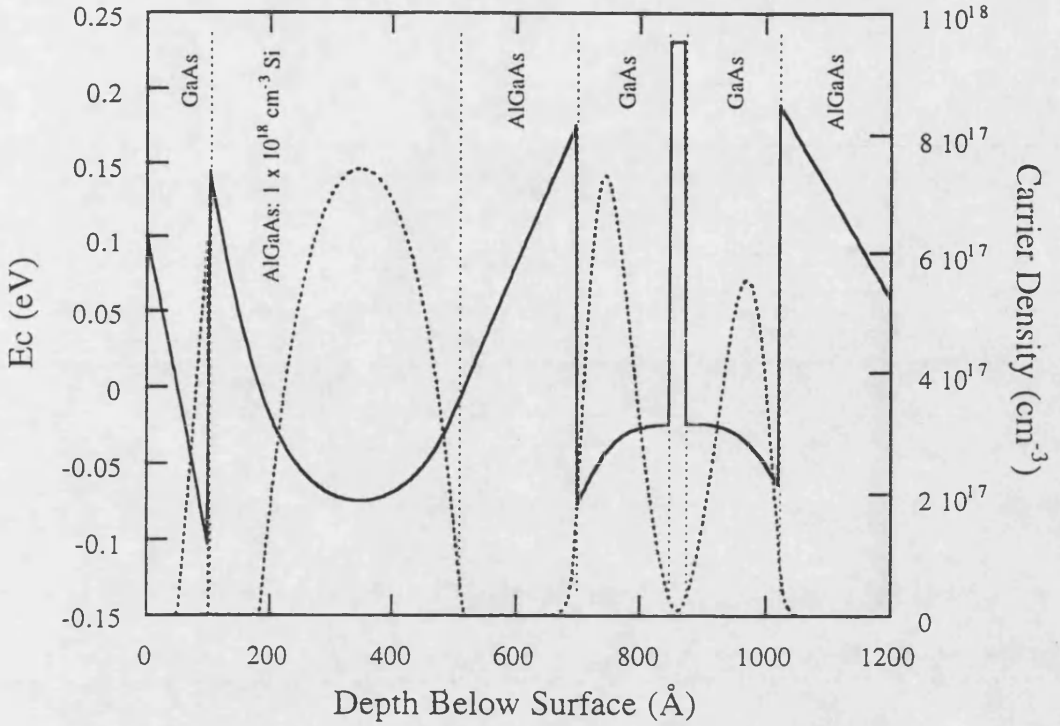

Figure 4.3: Self consistent conduction band diagram of the double quantum well heterostructure A1332, under a forward bias of 1.0 V (solid curve)[40]. The dashed curve shows the carrier density.

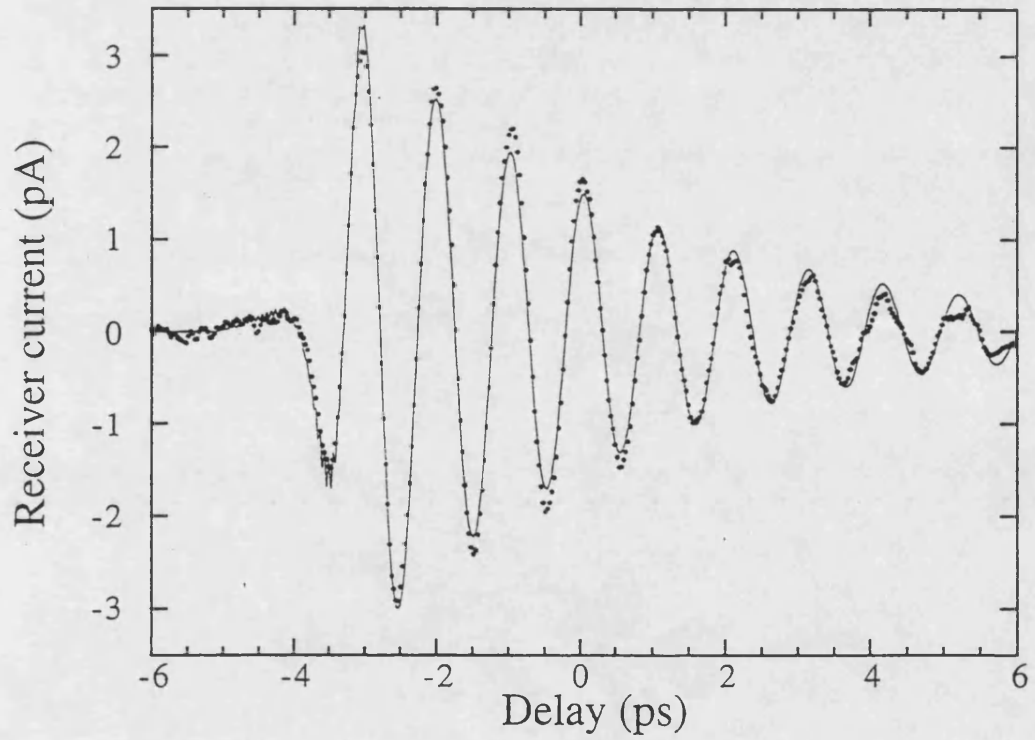

Figure 4.4: Differential THz transmission of a transmitted THz transient through A1332 in a 2.5 T perpendicular magnetic field and at T=5 K. The dots show the experimental data, whilst the solid curve shows a fit to the data of the incident transient convolved with the 2DEG dynamic conductivity.

Fermi level may absorb a FIR photon in order to make the transition to the next Landau level. Cyclotron absorption can also be described using the classical Drude model for the magneto-conductivity providing us with an uncomplicated method for analysis. It is convenient to use the angular expression for the a.c. magnetoconductivity.

$$\sigma(\omega) = \frac{\sigma_0}{1 - i\tau(\omega \pm \omega_c)} \qquad (4.1)$$

where '±' refers to left and right hand circular motion. Since the TDTS detects coherently, the parameter τ is the dephasing time[4], τ_{deph}, i.e. the time between those scattering events which break the phase of the electron system (impurities, phonons, interface roughness etc.). The change in amplitude transmission, with and without carriers, is given approximately by[5]

$$E_{N_s}(\omega) - E_0(\omega) = E_0(\omega)\frac{\sigma(\omega)Z_0}{1 + n + \sigma_g Z_0 + \sigma(\omega)Z_0} \qquad (4.2)$$

where n is the refractive index of GaAs and σ_g is the conductivity of the gate. The absorption resonance appears at $\omega = \omega_c$ and equation 4.2 may be approximated by $\Delta E(\omega) \propto E_0(\omega)\sigma(\omega)$. However, in this approximation τ_{deph} is replaced by an effective dephasing time $\tau^* = \tau_{deph}/(1+\omega_{ps}\tau_{deph})$, where $\omega_{ps} = N_s e^2 Z_0/m^*(1+n+\sigma_g Z_0)$, as a result of the finite number of carriers in the 2DEG[6].

In the time domain equation 4.1 becomes

$$\sigma(t) = \sigma_0 e^{-t/\tau} e^{i\omega_c t} \qquad (4.3)$$

and

$$\Delta E(t) \propto \int_{-\infty}^{t} E_0(t - t')\sigma_0 e^{-t'/\tau^*} e^{i\omega_c t'} dt' \qquad (4.4)$$

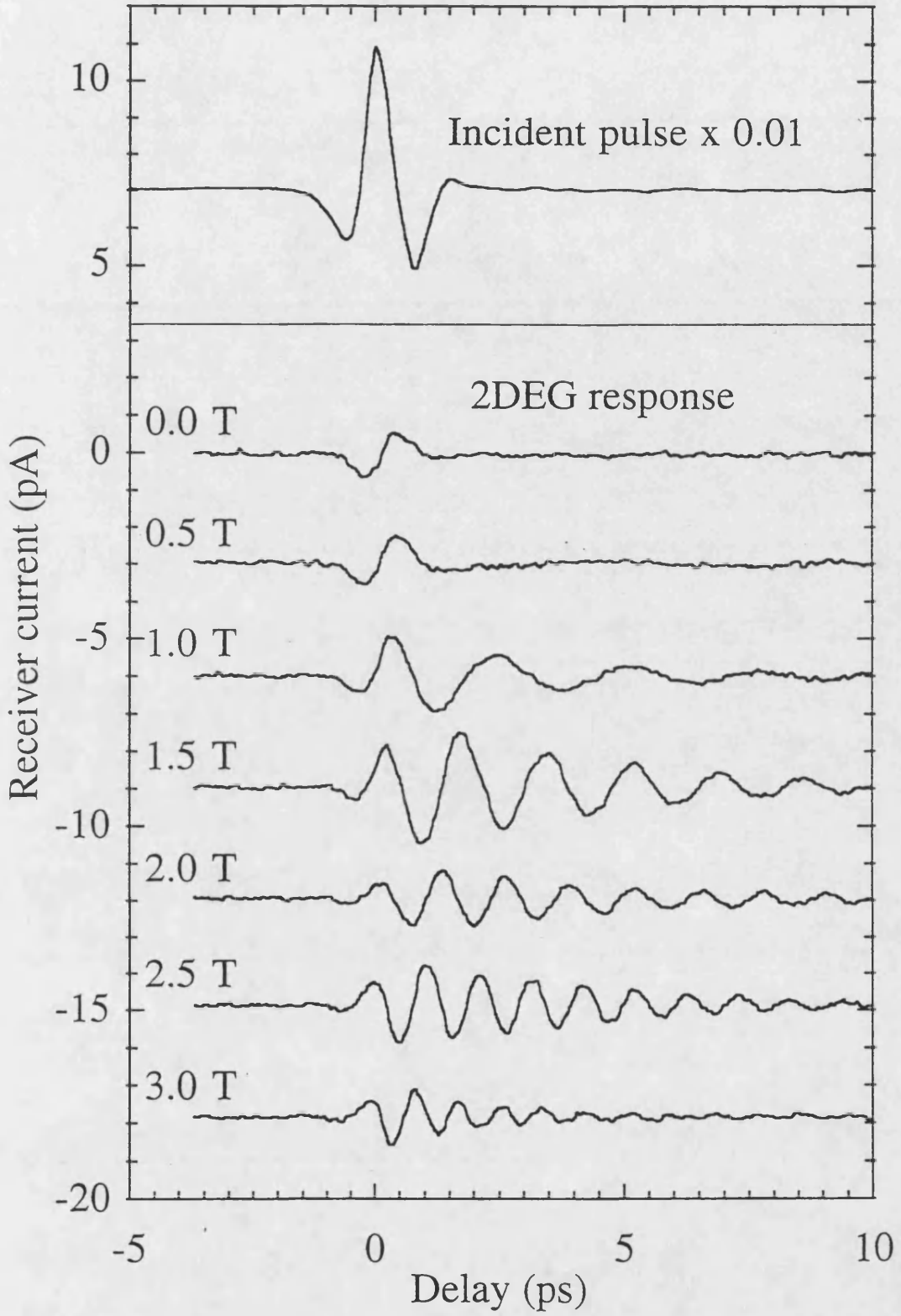

Figure 4.5 Differential THz transmission through A1332 at various magnetic fields. The traces have been offset with respect to one another by 3 nA for clarity. The receiver current produced by the incident transient, without the sample in the beam, is shown for comparison.

A fit of equation 4.4 to the data is indicated by the line in figure 4.4 from which values for the effective dephasing time and cyclotron frequency have been calculated. This fitting procedure can also be performed in the frequency domain by Fourier transforming the traces and applying equation 4.2. The time domain fitting method improves on the frequency domain method only in that it is less sensitive to the truncation necessary to remove temporal reflections.

The evolution of the cyclotron oscillations with magnetic field is shown in figure 4.5 together with the incident pulse. The scattering time of 3.5±0.5 ps of the oscillations was found to be approximately independent of magnetic field (figure 4.6), as might be expected, and equates to a dephasing time ~ 6.5±0.9 ps when corrected for the finite number of carriers. From the field dependence of the cyclotron frequency (figure 4.7) the effective mass, m*, is estimated to be 0.072 ± 10^{-6} m_0, compared with a bulk conduction band edge effective mass of $0.067\, m_0$ at T = 4 K[7]. No attempt has been made to account for subband hybridization of the two wells, however the good degree of fitting of the time domain traces suggests this is not essential at these magnetic fields.

Electron energy levels in the 2DEG are raised slightly above the conduction band by quantum confinement giving rise to a slightly higher effective mass through band non-parabolicity[8]. The measured value of the effective mass of $0.072\ m_0$ is in close agreement with calculations of the in-plane mass of the quantum wells by Ekenberg[8] which neglects band bending.

In comparing τ_{deph} with the momentum relaxation time, τ_{tr} as determined by Van der Pauw four terminal resistance measurements (τ_{tr} ~ 35 ps in A1332), one is reminded that τ_{tr} can be derived from the simplified Boltzmann equation within the relaxation approximation[4].

$$1/\tau_{tr} = \int dk' \, W_{k,k'} \, (1-\cos\theta) \qquad (4.5)$$

where $W_{k,k'}$ is the probability of scattering from state k to k' and θ is the scattering angle. The integral is performed over all values of k' that satisfy energy conservation. The relaxation time approximation (equation 4.5) favours large angle

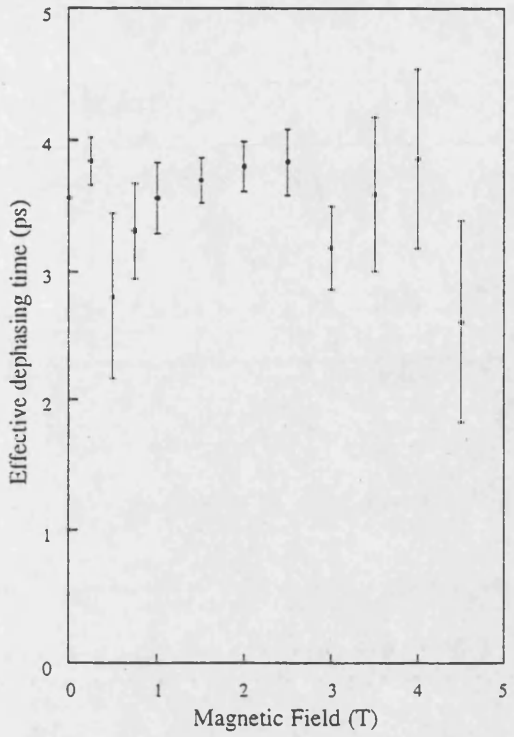

Figure 4.6: Effective dephasing time of the differential transmission through A1332 as determined from fits to the time domain cyclotron traces.

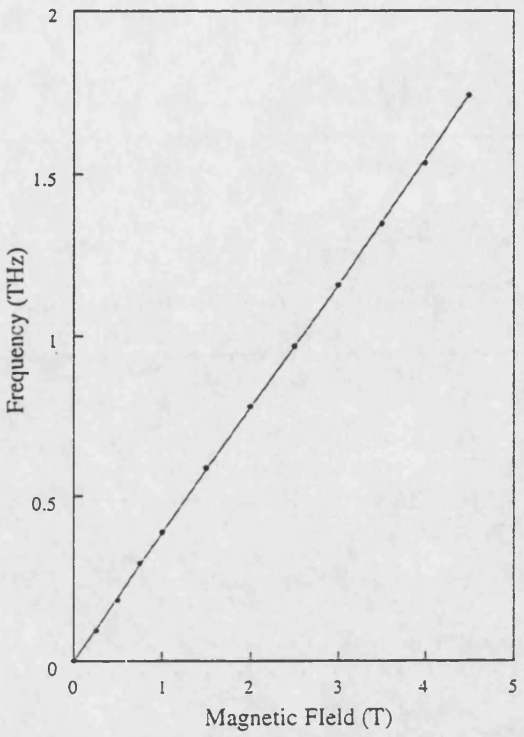

Figure 4.7: Cyclotron frequency of A1332 as determined from fits to the time domain data. The line is a least squares linear fit to the data.

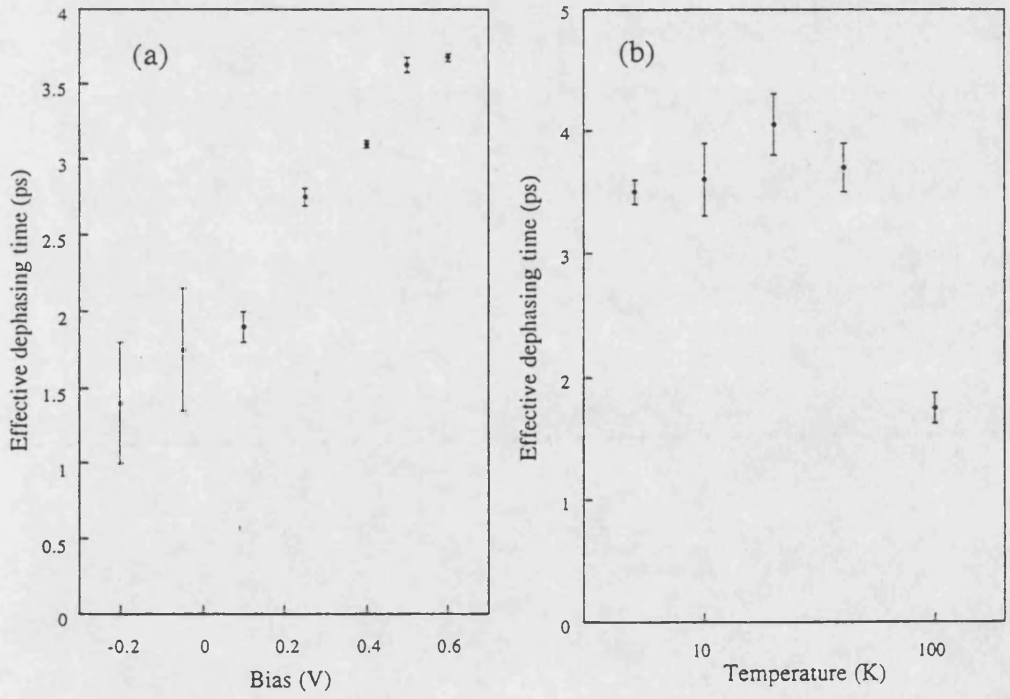

Figure 4.8: Effective dephasing time, determined from fits to the time domain cyclotron data from A1332, as a function of (a) gate bias (T=5 K) and (b) temperature (V_g= 0.6 V) both at B=2 T.

scattering over small angle scattering due to the weighting of the factor (1-cosθ). Thus if the relaxation time approximation is assumed in systems where small-angle scattering dominates, τ_{tr} represents only a fraction of the actual number of collisions as the transport relaxation time is primarily concerned with the charge arriving at a contact and not the nature of the path taken.

With regards to the sensitivity of the TDTS; the temporal regime during and immediately following ultrafast excitation of these systems is the coherent regime in which excitations have retained some definite phase relationship among themselves and with the electromagnetic radiation creating them. The dephasing time, τ_{deph}, is affected by any loss of coherence of the wavefunction, even small perturbations, effectively measuring the entire collision cross section; small and large angle scattering events being counted equally[4]. Thus, for large angle scattering, for instance in heavily doped bulk materials, $\tau_{deph} \sim \tau_{tr}$. In the case of small angle scattering τ_{deph} is expected to be shorter than τ_{tr}, especially for modulation doped heterostructures. Nearly an order of magnitude difference in τ_{deph} and τ_{tr} in A1332 indicates that τ_{deph} is indeed dominated by small angle scattering. However, an arbitrarily small deviation of the electron momentum will not dephase the cyclotron orbit. The smallest angle which will cause dephasing is of order $\theta_c = \pi/2\upsilon$ [9]. Here the filling factor, $\upsilon = N_s h/eB \sim 35/B$ so $\theta_c \sim 0.045B$.

A distinct dependence of the effective dephasing time on gate bias has been observed as shown in figure 4.8a. A field of 2 T was chosen such that the resultant cyclotron frequency, ~ 0.8 THz, lay close to the peak of the receiver's sensitivity. The relationship between bias and carrier density was not determined. Attempts to obtain SdH data from this sample using only the three contacts described above were dominated by a slowly increasing Hall resistance with increasing field. Hence the estimated scattering time could not be correct for the finite number of carriers. The reduction in carrier density might be expected to result in longer scattering times as τ^* approaches τ_{deph}. The decrease in effective dephasing time with decreasing bias is interpreted as a reduction in the ability of the 2DEG to screen the long range Coulomb field of remote ionised donors as it is depleted of carriers[10]. Alternatively, since the primary effect of lowering the gate voltage is to first deplete the well closest

to the surface, an interpretation based on very dissimilar mobilities between the two wells is possible.

Further information on the scattering mechanisms in the 2DEG may be gained from the temperature dependence. Figure 4.1 illustrates the dependence of the major scattering mechanisms on temperature[11]. Figure 4.8b shows the measured scattering times at five separate temperatures. The constant low temperature value of τ^* is indicative of scattering by remotely ionised donors but at higher temperatures this is superseded by LO phonon scattering. So we may conclude that the data is consistent with scattering by remote ionised donors within the AlGaAs layer at low temperatures.

4.3 SiGe/Si Heterostructure

In this section CR results from a remote doped SiGe/Si heterostructure will be discussed. Silicon dominates the electronics industry and the possibility of integrating high mobility modulation doped heterostructures with complementary metal oxide field effect transistors (CMOSFET) has provided impetus for research into these devices. $Si_{1-x}Ge_x$ has a smaller bandgap than Si and forms a type I heterojunction when grown on it. The conduction band offset is very small though (~ 0.02 eV: $0.2<x<0.5$) making it difficult to form a 2DEG[12]. In contrast, a large valence band offset is always achieved and two dimensional hole gases are more easily formed. The lattice constants of Si and Ge differ by 4.5% resulting in a critical thickness of order 100 nm for $Si_{0.8}Ge_{0.2}$ on Si (1% net lattice mismatch)[12]. To overcome this a buffer layer of continuously graded alloy several microns thick, starting with low Ge content ($0 < x < 0.05$) and increasing gradually to the required value ($x \sim 0.3$) is used. In order to form significant 2DEG mobilities (>100,000 cm^2/Vs at 5 K), Si quantum wells are grown on these buffer layers. In this approach the strain between the materials results in a type II heterojunction with both the Si conduction and valence band edges lower in energy (more negative) than in the alloy.

The modulation doped quantum well used here, 6A47915 [13], consisted of a 16 μm strained Si quantum well with a $Si_{0.7}Ge_3$ linearly graded buffer on top of a (100) Si substrate. The sample was grown by UHV chemical vapour deposition with arsenic as the dopant. SdH measurements gave a carrier sheet density of 8.9×10^{11} cm^{-2} and the Hall mobility was determined to be 1700 cm^2/Vs. A cleaved 1 cm square chip of thickness 550 μm was inserted into the spectrometer and backed with a 375 μm thick high resistivity silicon chip (ρ ~ 1.4 kΩcm) to reduce temporal reflections, leading to a spectral resolution of ~ 0.05 THz.

The sample had no gate so that the carrier modulation detection technique could not be employed. Instead the spectrum of each transmitted transient (T_1) was normalised to a reference spectrum (T_0) taken at a separate field such that $T_n = (T_1-T_0)/T_0$. In this way absorption peaks in T_1 that are not present in T_0 will appear as troughs in the normalised spectrum. Conversely absorption peaks in the reference spectra which do not appear in T_1 manifest as field independent peaks in the normalised spectrum. To maximise the clarity of the normalised spectra, the absorption peaks of T_1 and T_0 need to be well separated. Consequently for high field measurements (T_1 (B>2 T)) B = 0 T was chosen for the reference spectrum and B = 5 T for low field measurements. Typically, reference spectra were taken following every other measurement in an attempt to minimise the effects of long term drift in the THz signal due to changes in laser power.

Normalised experimental transmission spectra of the Si/SiGe heterostructure at T = 5 K in perpendicular magnetic fields between 1 T and 5 T are shown in figure 4.9. The cyclotron frequencies and effective dephasing times are shown in figures 4.10 and 4.11 respectively. The effective dephasing time was determined by fitting the magnitude of the complex conductivity (equation 4.1), to the troughs in the amplitude spectrum.

$$|\sigma| = \sigma_0 \sqrt{\frac{1}{1+\tau^2(\omega-\omega_c)^2}} \qquad (4.6)$$

Considering first the frequency, one notes immediately that it does not tend to zero at low fields as expected of an electron in a translationally invariant lattice[14].

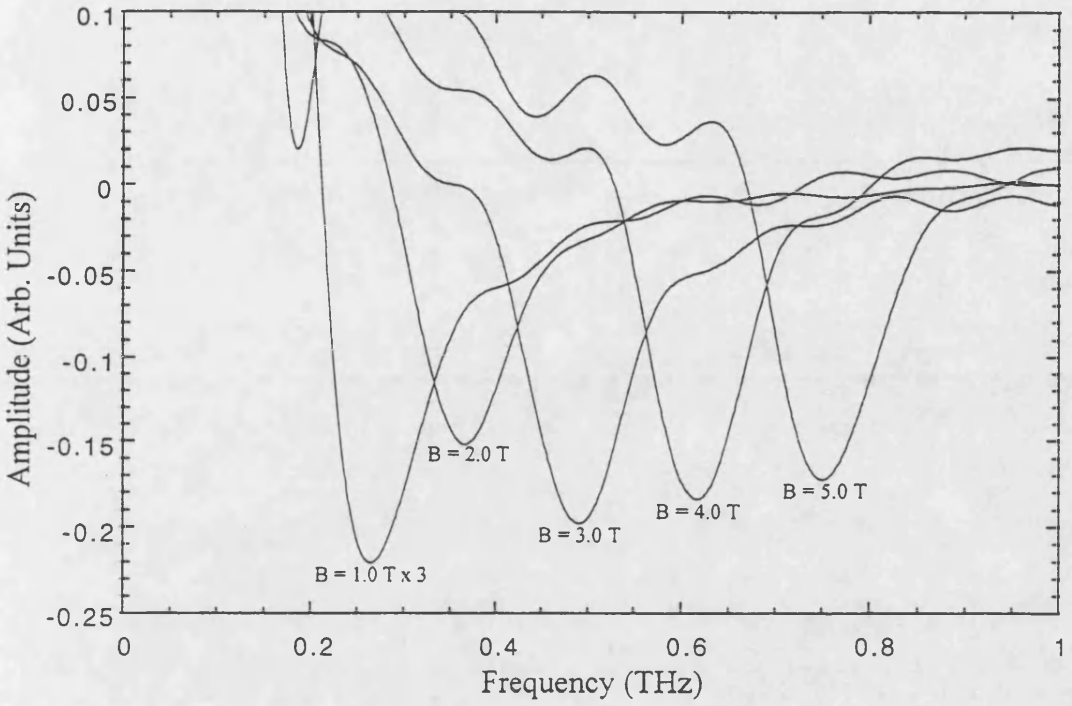

Figure 4.9: Normalised tranmission spectra of 6A47G15 in perpendicular magnetic fields at T=5 K.

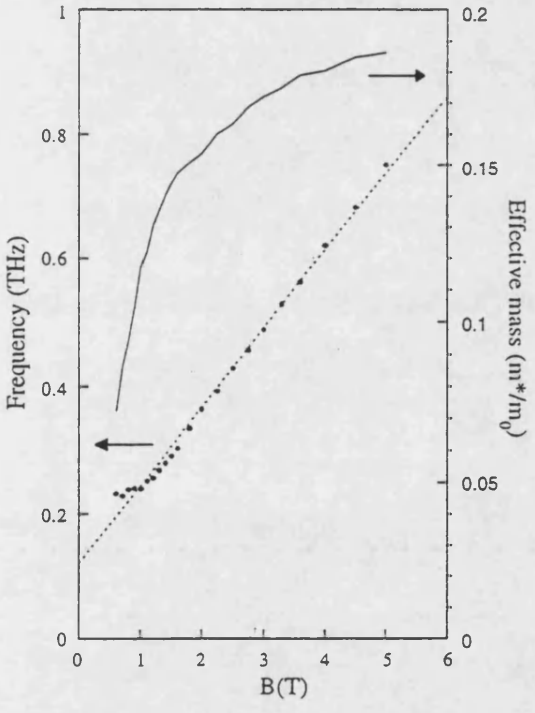

Figure 4.10: Cyclotron peak frequencies (dots) and field dependent effective mass (solid curve) of 6A47G15 as determined from fits to the frequency data. The dashed line is a least squares fit to the data.

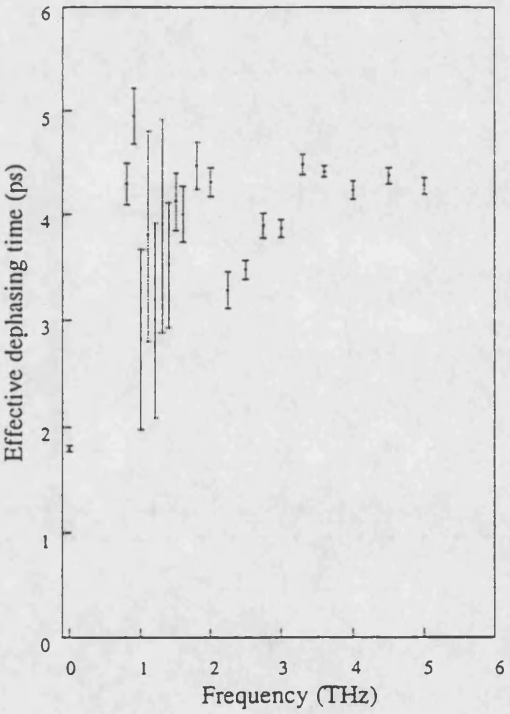

Figure 4.11: Effective dephasing times of 6A47G15 as determined from fits to the frequency data.

Attempts to extract a field invariant cyclotron mass from the data by confining a linear fit through the origin will clearly be in error, but from the slope alone (figure 4.10) a value of $m^* = 0.226 \pm 0.001\ m_0$ is obtained with an intercept of the frequency axis at 0.12 THz. Such mass enhancement has previously been linked to band nonparabolicity. However, investigations of systems with greater confinement and carrier density, both expected to enhance nonparabolic effects[15], have not observed this in Si/SiGe [8]. An error in the angle of the sample to the magnetic field would only make a ± 0.3% difference to the mass and neither explanation can account for the apparent offset. Alternatively, one may assume a field dependent mass, $m^* = eB/\omega_c$, and try to establish it independently for each experimental point (figure 4.10) in which case we obtain a change of nearly 40 % between 5 T to 1 T. From the work of Reiger and Vogl, m^* is estimated to be close to 0.198 m_0[16]. Similar CR effective mass reductions with decreasing magnetic field have been seen in Si MOSFET systems[17] as well as effective masses which decrease with decreasing N_s by as much as 40% between 2×10^{12} cm^{-2} and 5×10^{11} cm^{-2} [18]. Both effects have been attributed to potential fluctuations at the interface which tend to localise the carriers and thus increase ω_c [19].

Other cyclotron anomalies, at low filling factors, such as multiple lines and anomalous line widths have been explained in terms of magnetoplasmons[20], carrier localisation[19] or pinned charge density waves [17]. Although no deliberate lateral confinement exists in our sample, with its low mobility, some form of disorder is expected which may produce carrier localisation. The sample has been grown on a relaxed graded SiGe layer, which leads to significant surface roughness and defect densities of ~ 10^6 cm^{-2} [21]. The strain relaxation of the Si quantum well may also produce threading dislocations in the 2DEG channel.

Carrier localisation in quantum dot and antidot arrays in SiGe and SiMOS devices have been observed to produce a similar effect on the cyclotron frequency as observed in this sample[22,23,24] and Griffin *et al.*[25] have applied this analogy to the interpretation of their results of a similar system. In the quantum dot case, the confinement potential results in a zero field resonance (ω_0) with a double branch structure, the upper (CR-like) branch of which resembles our data whilst the lower

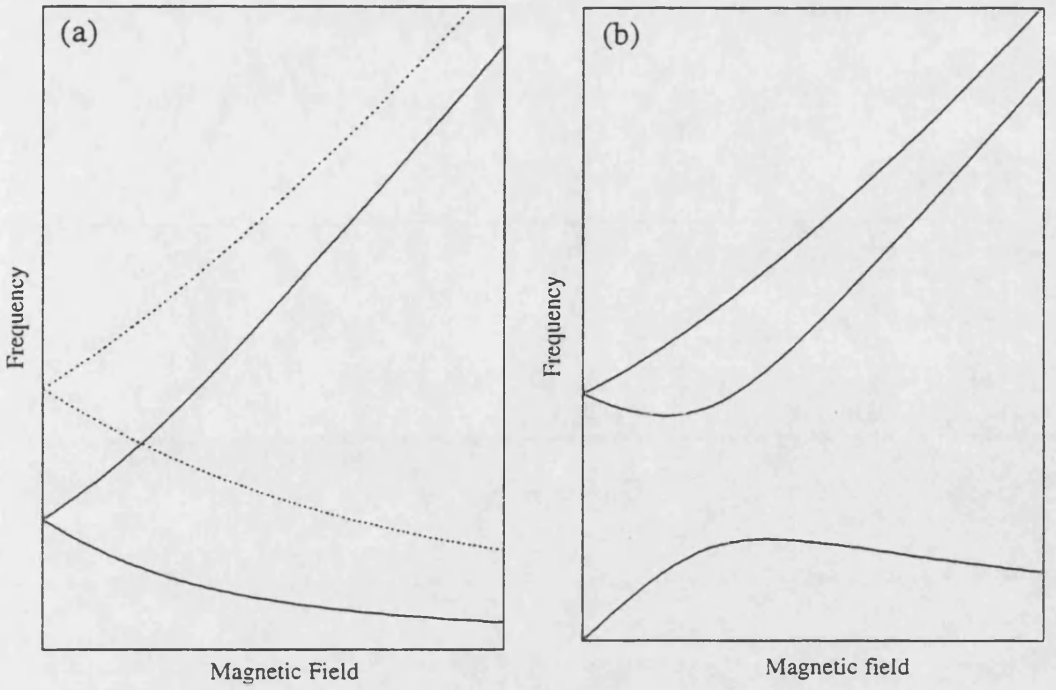

Figure 4.12 Schematic of resonant frequencies versus magnetic field for a (a) quantum dot and (b) antidot system. The dashed curve in (a) shows a higher mode of the quantum dot system

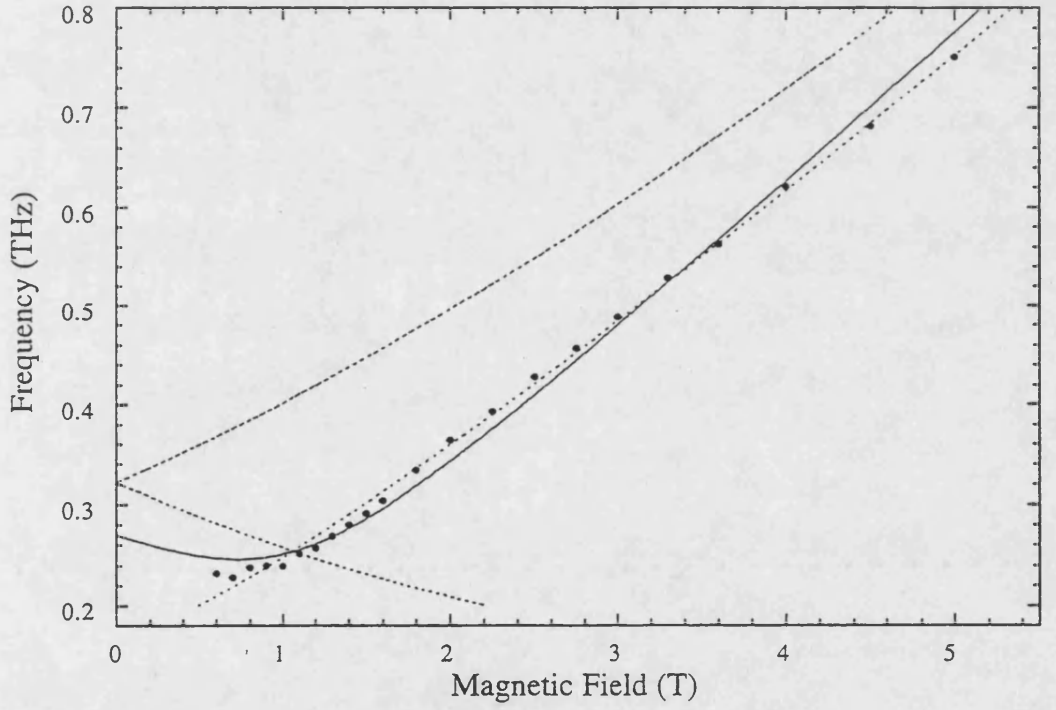

Figure 4.13: Cyclotron resonance frequency (dots) in 6A47G15 as determined from fits to the transmission frequency data. The dashed (solid) curve represents a quantum dot (antidot) model fit to data. The higher lying quantum dot mode predicted from the fit is also shown.

would lie outside the spectrometer's frequency range (figure 4.12a). A semi-classical interpretation can be used to describe figure 4.12a [23]: the zero field ω_0 represents a volume resonance and as the field increases the lower branch describes electron skipping orbits within the circumference of the dot confining potential. The higher branch describes a magnetoplasma oscillation that approaches the CR as the orbit becomes small compared with the size of the dot. For 2D disk like dots with radius r in a medium of effective dielectric constant ε_{eff}, the resonance fields are given by[22]

$$B = \pm m^*(\omega_0^2-\omega^2)/e\omega \qquad (4.7)$$

where

$$\omega_0^2 = N_s e^2/2m^*\varepsilon_{eff}\, r \qquad (4.8)$$

The dotted line in figure 4.13 is a fit of equation 4.7 to the data. Better agreement with the data is found for the quantum dot model than the homogenous model and an effective mass more consistent with theoretical predictions[16] is also obtained (table 4.1). In a strained Si layer, the strain is sufficient to break the six-fold degeneracy found in bulk Si and the ground state is only doubly degenerate. At the experimental temperature and carrier density, all the electrons lie in this lowest valley and thus only the light mass of the lowest valley is measured[26]. This is consistent with the results of Griffin *et al.* who inferred an effective mass of 0.195 m_0. The value for ω_0 allows the radius of the localising potential to be estimated as ~ 5±1 μm.

Model	m* (m_0)	ω_0 (THz)	r (μm)
Quantum Dot	0.196 ± 0.002	0.162 ± 0.005	5 ± 1
Antidot	0.183 ± 0.005	0.271 ± 0.009	16 ± 3

Table 4.1: Results of fitting quantum dot and antidot models to the data

At low fields the fit is not so good and an excessive degree of curvature toward the horizontal axis is apparent, which is not predicted by the quantum dot model. In the magnetoplasma interpretation higher order modes of the zero field

resonance ($2\omega_0$) are possible (figure 4.12a). Anticrossings of these modes have been observed to produce results similar to figure 4.13 [27] but they would not be expected to cross at the correct position in this case.

The far infrared modes of antidot lattices are much less clear than those of quantum dots and are chaotic in nature[28]. Using the effective medium approximation (EMA)[29], the excitation spectrum of an array of antidots can be calculated. This model takes into account the interaction between antidots using classical electrodynamics and does not assume that the antidot array is ordered. The model predicts a zero field resonance from which two modes extend of which the lower branch best resembles the data (figure 4.12b), the upper branch can be very weak and is not always observed even in intentionally created antidot lattices[22,30]. A third lower branch also exists but it is outside the detection range of our spectrometer. Again a classical interpretation can be applied and ω_0 is a plasma mode of the antidot glass. The lower branch describes pseudo classical cyclotron orbits around multiple antidot potentials until the orbits become smaller than the antidot radius. The branch then obtains a shallow negative gradient and describes skipping orbits around the antidot. In contrast, the middle branch begins with a negative gradient but with increasing field goes on to describe pseudo classical cyclotron motion in the gaps between the dots. The highest branch is a magnetoplasmon like mode of the antidot glass. The magnetic dependence of all three branches according to Mikhailov and Volkov[29] is described by

$$B = \frac{\alpha}{\omega} \pm \left(\left(\frac{\alpha}{\omega} \right)^2 - \left(\omega_0^2 - \omega^2 \right) \left(\frac{m^*}{e} \right)^2 \right)^{0.5} \qquad (4.9)$$

where

$$\alpha = \pm \left(\frac{m^* \omega_0^2 (1-2f)}{2e} \right) \qquad (4.10)$$

and

$$\omega_0^2 = 3\pi^2 N_s e^2 / 8 m^* \varepsilon_{eff} r \qquad (4.11)$$

where f represents the antidot space filling factor $f = 1-\pi(r/a)^2$ and a is the average distance between antidots according to Huber *et al.*[34]. The solid line in figure 4.13 represents a fit of equation 4.9 to the data. The value determined for the effective mass (table 4.1) is lower than one might expect but it appears that the low field data is better described by the antidot model. One notes that an excellent fit is not expected as the EMA makes a number of assumptions[31] and can only supply a qualitative model.

An approximately constant value of 4±1 ps is obtained for τ^* over the range 0.5 T to 5 T, figure 4.11, and equates to $\tau_{deph} \sim 6.5\pm1.5$ ps when corrected for the finite number of carriers. There is over an order of magnitude difference between τ_{deph} and the 0.2 ps momentum relaxation time inferred from the d.c. mobility. It was noted in section 4.2 that τ_{deph} is expected to be shorter than τ_{tr} in modulation doped heterostructures. A longer τ_{deph} may be due to large scale inhomegeneities which have greater effect on τ_{tr}. Cyclotron motion probes the material on a length scale of order the cyclotron diameter, D_c[22], where

$$D_c = \frac{\hbar\sqrt{8\pi N_s}}{eB} \qquad (4.12)$$

$D_c \sim 4$ μm at B = 0.5 T which is smaller than the size of the dots, antidots (table 4.1) and the spacing between antidots (from equation 4.10, a ~ 50±10 μm), consistent with the above hypothesis. The long τ_{deph} is not expected to be filling factor related as $\nu \sim 40/B$ and such effects are expected to occur at values much closer to unity[19]. One might also expect both models to exhibit an inhomogeneously shortened dephasing time due to spatial fluctuations in the repulsive potentials. However Merkt[34] argued that Coulomb interaction between the electrons is sufficiently large to apply the generalised Kohn's theorem[32] such that the oscillators are locked in step.

It has been shown that when silicon undergoes a plastic deformation, large densities of acceptor-like (dangling bonds) point defects[33] are produced. Such deformation may occur during growth of the relaxed, graded SiGe layer[21]. These defects could then form repulsive islands[34] and lead to antidot states. Richter *et al.*[35] observed two resonances, in a GaAs/AlGaAs heterojunction selectively doped with repulsive Be scatterers. When doped with Si (attractive scatterers) only the usual CR was observed. Recently Norman *et al.* have observed antidot behaviour in the FIR magneto-transmittance of a Si/SiGe heterojunction similar to that used here which was associated with self organised defects in the relaxed graded-composition buffer layer[36].

4.4 Coherent Control of Cyclotron Oscillations Using Two THz Transients

The idea of controlling physical and chemical processes in matter using the coherence properties of electromagnetic radiation has been of interest ever since lasers became widely available. Recent examples of coherent control in semiconductors include manipulation of THz radiation associated with quantum beats in coupled wells[37], destruction of exciton populations in quantum wells[38] and creation of photocurrents with prescribed magnitude and direction in bulk GaAs[39]. Complete coherent control depends on the use of light pulses which are short compared with phase relaxation times which are typically a few picoseconds or less in semiconductors at low temperature. Until now, therefore, most experiments have involved the coherent control of quantum mechanical systems using light in the visible and near infra-red where ultrafast sources are available. Such experiments have been extended in this work to the far infrared (THz) region of the electromagnetic spectrum using a simple double pulse source of quasi-single cycle THz radiation applied to the excitation of coherent CR from a 2DEG (A1332).

The dual pulse source described in section 2.4 enabled the generation of 2 THz pulses separated by an adjustable time interval. Here the first THz pulse was used to excite cyclotron oscillations in A1332 whilst the second was used to enhance

or suppress these oscillations depending on the relative time delay between the two THz pulses. For this experiment the two laser pulses were point focused and edge illuminated the same side of a CPS transmitter anode with a lateral separation of ~ 30 μm. This produced two THz transients of the same polarity and similar magnitude. The 30 μm separation was necessary to reduce photo-screening effects and prevent the two pulses from interfering. Figure 4.14 displays receiver currents obtained for different delays between the laser pulses with no sample in the beam. With the variable pulse between -8 ps (the greatest measured separation) and -1 ps the amplitude and temporal width of each pulse remains approximately constant. Above -1 ps the pulses begin to overlap and the total amplitude is reduced as the point of zero delay is crossed. As the time delay becomes positive the amplitude of the variable delay pulse grows at the expense of the fixed pulse.

Figure 4.4 shows the receiver current signal from the 2DEG due to a single THz transient in a field of 2.5 T at T=5 K. Signals resulting from double pulse excitation under the same conditions are shown in figure 4.15 where the markers indicate the approximate centres of each exciting pulse. The interpulse separation is increased by 0.27 ps between traces, corresponding to a phase increase in the cyclotron orbit of ~ $\pi/2$. The effect of varying the delay can be seen by considering the latter part of each trace. For delays equivalent to an even integral multiple of π the current induced in the 2DEG by the second pulse reinforces that remaining from the first. For delays equivalent in phase to odd integral multiples of π the induced currents are opposite in polarity and the signal is attenuated. This is more obvious at a separation of 5π than at 7π because the initial signal has decayed more at the larger delay. In a quantum mechanical picture the initial pulse excites electrons into the first vacant Landau level whose population is subsequently enhanced or destroyed by the second pulse.

The relative phase of the traces following the second pulse is seen to vary relatively slowly between delays corresponding to odd integer multiples of the cyclotron orbit phase. In order to quantify this behaviour an exponentially damped cosine wave was fitted to both parts of each trace and the phases were extracted. The difference in phase as a function of delay is shown as points in figure 4.16. This

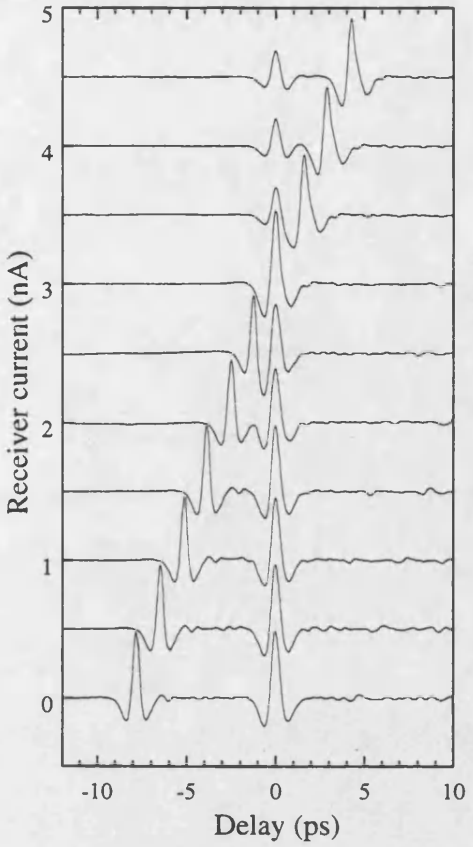

Figure 4.14: Transient receiver currents arising from double pulse excitation of the THz source. The optical excitation pulse separation was altered by 1.33 ps between adjacent traces, which have been vertically displaced by 0.5 nA with respect to each other for clarity.

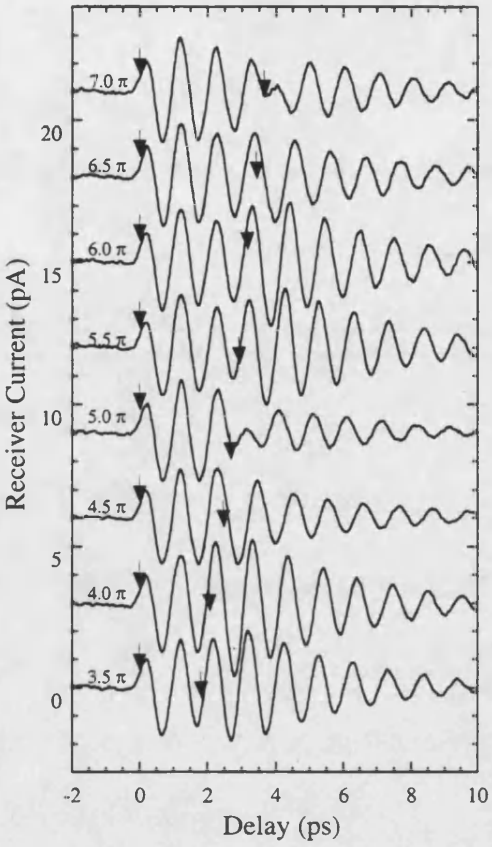

Figure 4.15:Response of the 2DEG to double pulse excitation at times indicated by the marks. Traces are vertically displaced with respect to each other by 4 pA for clarity. Temperature was 5 K and magnetic field was 2.5 T

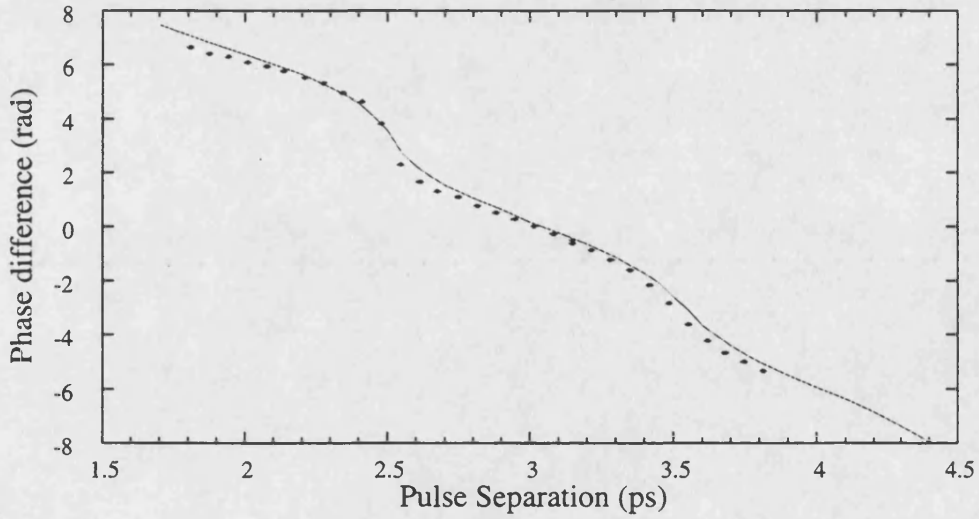

Figure 4.16: Phase differences between cyclotron oscillations following first pulse and that following second pulse excitation as a function of pulse separation. The phases were extracted by fitting exponentially damped cosine waves to both parts of the time domain traces of figure 4.15 (dots) or to fits of the traces using equation 4.3 incorporating the two driving pulses from figure 4.14 in the convolution (lines).

figure also shows the difference frequency calculated by fitting exponentially damped cosines to fits to the time domain traces of figure 4.15, using equation 4.3 and incorporating the two driving pulses from figure 4.14 in the convolution. The quality of agreement further demonstrates the effectiveness of this simple model in predicting the 2DEG behaviour.

4.5 Summary

Cyclotron resonance has been studied in AlGaAs/GaAs and Si/SiGe quantum wells as a function of magnetic field, carrier density and temperature. The electron effective dephasing time in the GaAs quantum wells decreases with decreasing carrier density and is thought to be due to a reduction in its ability to screen scattering by remote impurity potentials. This has been determined to be the primary scattering mechanism at low temperatures. The CR data from the Si/SiGe quantum well sample approaches a non-zero offset at zero field and displays an extended scattering time when compared with transport data. The results may be explained by the existence of antidot like states. To allow further understanding improved low field measurements using low frequency antenna pairs and a gated device need to be performed. Finally the dual pulse source has been used to impulsively drive and coherently control cyclotron oscillations in a 2DEG. This is believed to be the first demonstration of coherent control of an intraband process.

References:

(1) G. Abstreiter, P. Kneschaurek, J. P. Kotthaus and J. F. Koch, Phys. Rev. Lett. **32** 104 (1974); S. J. Allen, Jr., D. C. Tsui and J. V. Dalton, Phys. Rev. Lett. **32**, 107 (1974)

(2) H. L. Störmer, R. Dingle, A. C. Gossard, W. Wiegmann and M. D. Sturge Solid State Commun. **29**, 705 (1979)

(3) A1332 grown and characterised at Cavendish Laboratory

(4) J. P. Harrang, R. J. Higgins, R. K. Goodall, P. R. Jay, M. Laviron and P. Delescluse, Phys. Rev. **B 32**, 8126 (1985)

(5) K. W. Chiu, T. K. Lee and J. J. Quinn, Surf. Sci **58**, 182 (1976)

(6) R. J. Nicholas in "Handbook on Semiconductors", completely revised edition Ed. M. Balkanski, Elsevier, Amsterdam (1994), p.385

(7) Modular Series on Solid State Devices, Robert F. Pierret, Ed. Gerold W. Neudeck, Vol 6, Advanced Semiconductor Fundamentals, Addison-Wesley Publishing Company, Reading, Massachusetts (1987), p.84

(8) U. Ekenberg, Phys. Rev. B 40, 7714 (1989)

(9) D. W. Terwilliger and R. J. Higgins, Phys. Rev. **B7**, 667 (1973)

(10) D. Some and A. V. Nurmikko, Appl. Phys. Lett. **65**, 3377 (1994)

(11) "Fundamentals of Semiconductors", Peter Y. Yu and Manuel Cardona Springer-Verlag, Berlin (1996), p. 214

(12) E. A. Fitzgerald, Annual Review of Materials Science 25, 417 (1995); "Low-Dimensional Semiconductors," M. J. Kelly, Clarendon Press, Oxford (1995) p. 331

(13) 6A47915 grown and characterised by DERA at Malvern

(14) L. Brey, N. F. Johnson and B. I. Halperin, Phys. Rev. **B 40**, 647 (1989)

(15) N. Griffin, D. D. Arnone, D. J. Paul, M. Pepper, D. J. Robbins A. C. Churchill, J. M. Fernandez,, J. Vac. Sci. and Tech. **B 16**, 1655 (1998)

(16) "Electronic-band parameters in strained $Si_{1-x}Ge_x$ alloys on $Si_{1-y}Ge_y$ substrates" M. M. Reiger and P. Vogl, Phys. Rev. **B 48**, 14276 (1993)

(17) B. A. Wilson, S. J. Allen, Jr. and D. C. Tsui, Phys. Rev. Lett. **44**, 479 (1980)

(18) J. P. Kotthaus, G. Abstreiter, J. F. Koch and R. Ranvaud, Phys. Rev. Lett. **134** 151 (1975)

(19) J.-P. Cheng and B. D. McCombe, Phys. Rev. **B 44**, 3070 (1991)

(20) Z. Sclesinger, S. J. Allen, J. C. M Hwang, P. M. Platzman and N. Tzoar, Phys. Rev. **B 30**, 435 (1984)

(21) E. A. Fitzgerald and S. B. Samavedam, Thin Solid Films **294**, 3 (1997)

(22) K. Kern, D. Heitmann, P. Grambow, Y. H. Zhang and K. Ploog, Phys. Rev. Lett. **66**, 1618 (1990)

(23) D. Heitmann and J. P. Kotthaus, Phys. Today **46**, 56 (1993)

(24) A. Huber, I. Jejina, H. Lorenz, J. P. Kotthaus, S. Bakker and T. M. Klapwijk Semicon. Sci. Technol. **10**, 365 (1995)

(25) N. Griffin, D. D. Arnone, D. J. Paul, M. Pepper, D. J. Robbins and A. C. Churchill, Solid State Elec. **42**, 1159 (1998)

(26) S. Q. Murphy, Z. Schlesinger, S. F. Nelson, J. O. Chu and B. S. Meyerson Appl. Phys. Lett. **63**, 222 (1993)

(27) D. Heitmann in "Physics of Nanostructures", Ed. J. H. Davies and A. R. Long IOP publishing Ltd., Bristol, England (1992), p 249; W. Hansen in "Physics of Nanostructures", Ed. J. H. Davies and A. R. Long, IOP publishing Ltd. Bristol, England (1992), p 284

(28) A. Lorke, Surf. Science **263**, 307 (1992)

(29) S. A. Mikhailov and V. A. Volkov, Phys. Rev. **B 52**, 17260 (1995)

(30) K. Bollweg, T. Kurth, D. Heitmann, V. Gudmundsson, E. Vasiliadou P. Grambow and K. Eberl, Phys. Rev. Lett. **76**, 2774 (1996)

(31) The EMA assumes a frequency independent interantidot interaction, abrupt density profile, macroscopic conductivity and an activation energy $\hbar\omega_c$.

(32) Walter Kohn, Phys. Rev. **123**, 1242 (1961)

(33) L. C. Kimering and J. R. Patel, Appl. Phys. Lett. **34**, 73 (1979)

(34) U. Merkt, Phys. Rev. Lett. **76**, 1134 (1996)

(35) J. Richter, H. Sigg, K. v. Klitzing and K. Ploog, Phys. Rev. **B 39**, 6268 (1989)

(36) C. E. Norman, N. Griffin, D. D. Arnone, D. J. Paul, M. Pepper, B. Gallas J.M. Fernandez, Solid State Phenomena **63-4**, 25 (1998)

(37) P. C. M. Planken, I. Brener, M. C. Nuss, M. S. C. Luo and S. L. Chuang Phys. Rev. **B 48**, 4903 (1993)

(38) A. P. Heberle, J. J. Baumberg and K. Köhler, Phys. Rev. Lett. **75**, 2598 (1995)

(39) A. Hache, Y. Kostoulas, R. Atanasov, J. L. P. Hughes, J. E. Sipe and H. M. van Driel Phys. Rev. Lett. **78**, 306 (1997)

(40) Self consistent Poisson/Schrödinger band calculations performed by Dr. Steve Andrews University of Bath

5 Coherent Plasmons

5.1 Introduction

In this chapter inter and intraband excitation of coherent plasmons in a GaAs/AlGaAs 2DEG is discussed. Above bandgap 70 fs pulses from a Ti:Sapphire laser provided the interband excitation whilst the intraband excitation is provided by THz transients. Coupling of light to the plasmons was achieved with 8 and 5 μm period surface gratings for the intra and interband measurements respectively. The chapter begins with the intraband investigations, a description of the sample and experimental setup followed by investigations of the plasmon dephasing time and frequency as a function of carrier density and magnetic field. Interband excitation was investigated as a function of pump fluence and energy.

The optical and electronic properties of the collective plasmon modes of two dimensional electron systems have received much attention both experimentally and theoretically[1-5]. Interest is spurred by the potential for utilising nonlinear properties of plasma oscillations[6] as FIR sources, detectors, amplifiers, mixers and frequency multipliers[7-10] as well as for high speed electronics[11]. The frequencies of these modes are determined by the sheet carrier density and can be tuned electrically by applying a bias voltage to an overlaid gate. Two dimensional plasmons in solid state systems were first observed in silicon metal oxide systems in transmission measurements[12], where the plasmon frequency typically lies in the FIR. Two dimensional plasmons[13] and magnetoplasmons[14] have been observed in GaAs/AlGaAs heterostructures using

CW absorption techniques and more recently the coherent emission of plasmons from a 2DEG using interband excitation has been observed in the time domain[15].

5.2 Intraband Measurements

5.2.1 Experimental Details

The sample of these investigations consisted of an MBE grown $GaAs/Al_{0.3}Ga_{0.7}As$ single heterojunction, A1690[16], (figure 5.1a) with a nominal carrier density of 2.8×10^{11} cm^{-2} (6×10^{11} cm^{-2}) without (with) illumination and a mobility of 6.15×10^{5} cm^2/Vs (1.40×10^{6} cm^2/Vs) at a temperature of 5 K. The mobility corresponds to a momentum relaxation time of ~ 25 ps (~ 60 ps). A 9 mm by 5 mm Hall bar was isolated by chemically etching and Au/Ge/Ni ohmic contacts made. A 5 mm square of 5 nm thick NiCr was evaporated on to the surface of the chip to act as a semitransparent gate (figure 5.1b). To couple the 2D plasmons to light a 110 nm thick grating of Au/NiCr with 8 μm period and aspect ratio (metal/period) of 0.5 was microfabricated on the surface of the sample Hall bar on top of the NiCr gate. With the NiCr in place the plasma frequency (~ 0.1 THz) was too low to be detected by the TDTS. Subsequently the NiCr gate was largely removed with concentrated hydrochloric acid to increase the frequency of the coupled 2D plasmon by reducing the screening. The electron micrograph of the Hall bar surface (figure 5.1c) indicates that the majority of the NiCr has been removed, although sufficient coverage remains to modulate the carrier density of the whole 2DEG. In an attempt to reduce temporal reflections, a 0.64 mm backing piece of semi-insulating GaAs was held in optical contact with the 0.43 mm thick sample with an intervening layer of paraffin oil. The combined optical thickness allows larger delays and spectral resolution of 0.04 THz, though some residual effect of the reflection from the interface remained.

The heterojunction was investigated in a transmission geometry with the sample maintained at a temperature of 5 K, in the bore of a split coil superconducting magnet. Once at 5 K the sample was illuminated with above bandgap radiation for

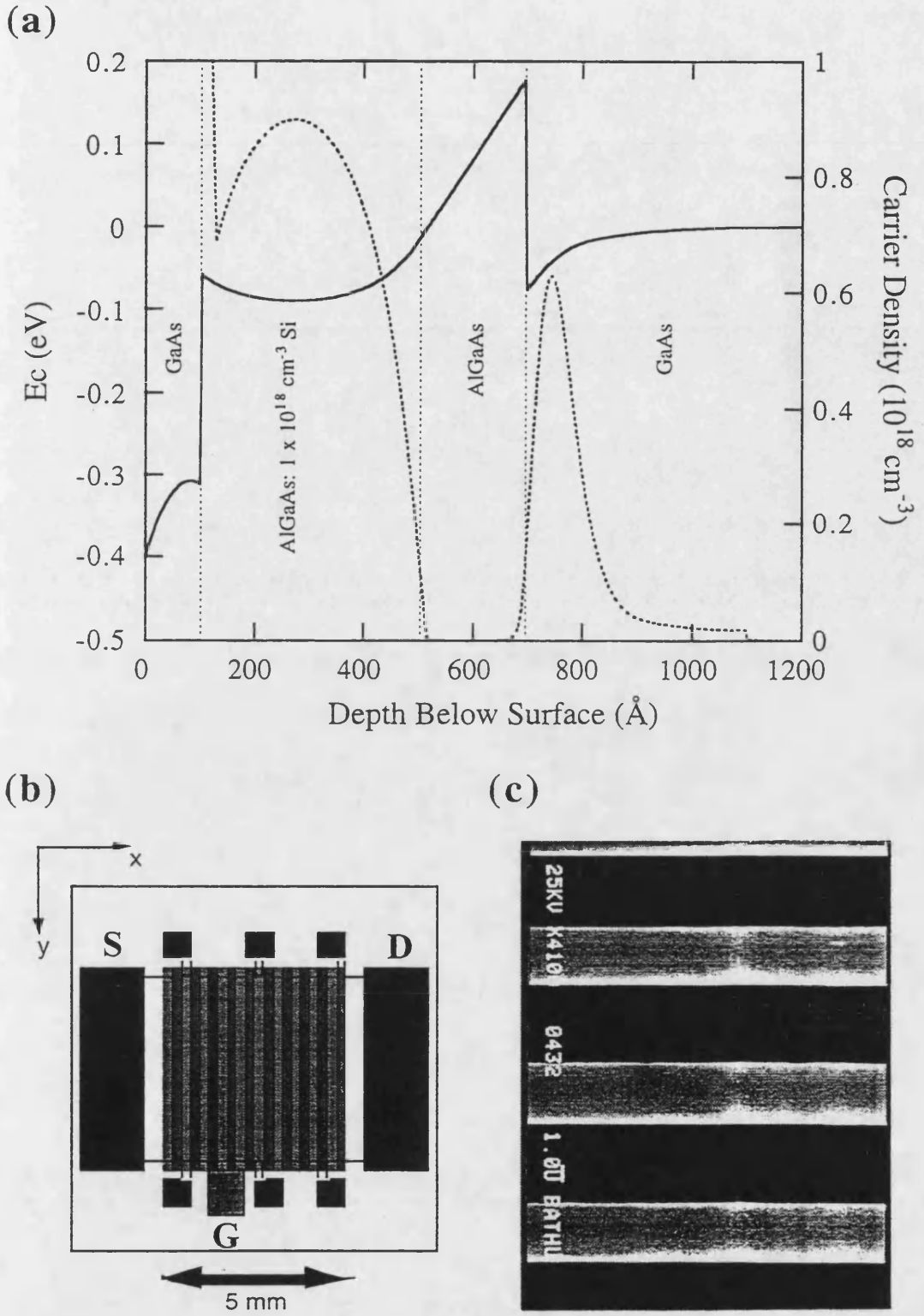

Figure 5.1: (a) Self consistent conduction band calculation of A1690, under a forward SG bias of 1.0 V [44]. The dashed curve follows the predicted carrier density distribution. (b) Schematic diagram of the test device: black marks ohmic contacts whilst grey indicates the grating/gate structure (not to scale). (c) An electron micrograph of the Hall bar surface. Light areas are the grating metal; there is no evidence of significant residual metal between the grating fingers (see text).

~ 60 s to ensure the maximum number of free carriers through the persistent photoelectric effect[17]. The frequencies for the intraband excitations of our sample were expected to be close to the low frequency limit of the spectrometer (~ 0.1 THz) and it was necessary to optimise the spectrometer for these low frequencies. The silicon on sapphire receiver used an 80 μm dipole antenna to give a large low frequency response[18]. The transmitter consisted of a bow tie shaped antenna microfabricated on SI GaAs. The laser was focused to a 5 μm spot on the point tip of the positive electrode for maximal signal strength[19]. A typical bias of 80 V was applied between the tips of the structure resulting in a photocurrent of 1.3 mA. This transmitter design has been found to provide more power at lower frequencies (0.1-0.5 THz) than the more common coplanar stripline (section 2.2.3). Without a sample in the beam the transmitter/receiver combination resulted in a peak receiver current of 13 nA with a peak response at 0.39 THz and 10% amplitude points at 0.12 THz and 0.94 THz.

The grating was employed as a gate in order to modulate the 2DEG carrier density and allows phase sensitive detection to be employed to isolate signals from the 2DEG from the much larger transmitted THz transient. SdH measurements at various biases revealed only a single carrier density, indicating minimal spatial modulation of the carrier density. A typical plot of ρ_{xx} with inverse magnetic field at 0.25 V forward gate bias is shown in figure 5.2. The apparent beating in the trace is a result of the spin-splitting of Landau levels. The inset in figure 5.2 displays the carrier density deduced from the SdH measurements as a function of bias.

In order to ascertain the origin of the modulated traces with respect to bias, the THz transmitted spectrum, without synchronous detection, was taken at +0.4 V and -0.3 V. Each trace was then Fourier transformed and the difference spectrum calculated ($t_{0.4V}(f)$-$t_{-0.3V}(f)$). In this way absorption peaks in $t_{0.4V}(f)$ that were not present in $t_{-0.3V}(f)$ appear as troughs in the difference spectrum, conversely absorption peaks in $t_{-0.3V}(f)$ which do not appear in $t_{0.4V}(f)$ manifest as peaks. The difference spectrum (figure 5.3) displays a trough at ~ 0.21 THz: absorption by the fundamental

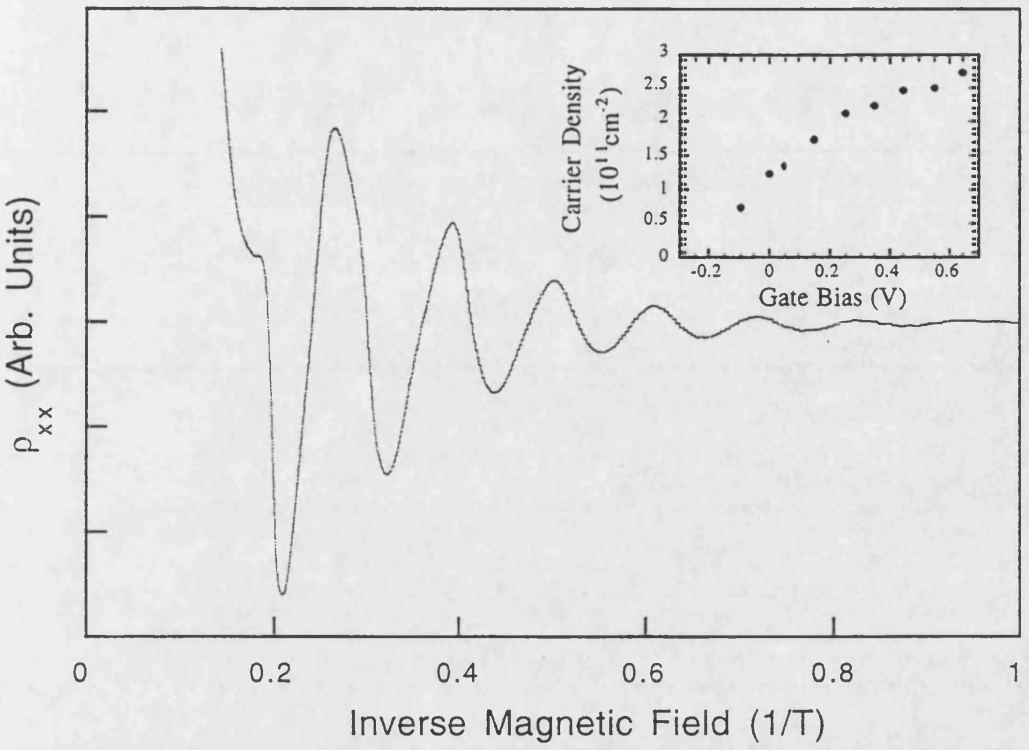

Figure 5.2: A typical plot of ρ_{xx} against inverse magnetic field (0.25 V forward gate bias). Inset shows the calculated sheet carrier density.

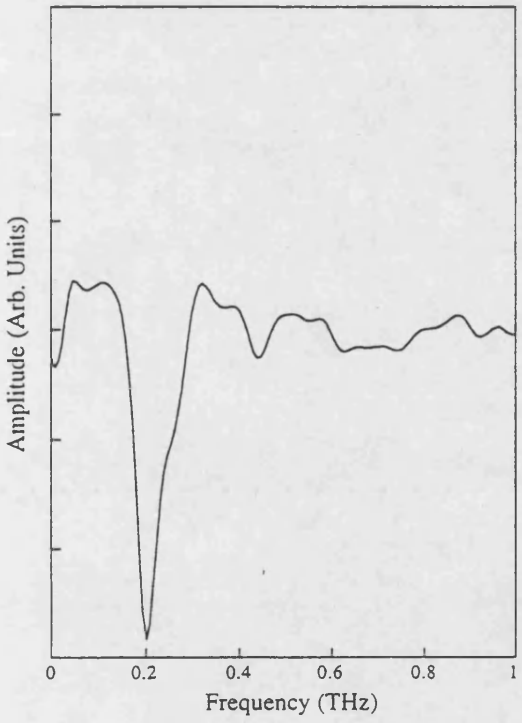

Figure 5.3: Difference of spectra for gate biases -0.3 V and +0.4 V at T=5 K.

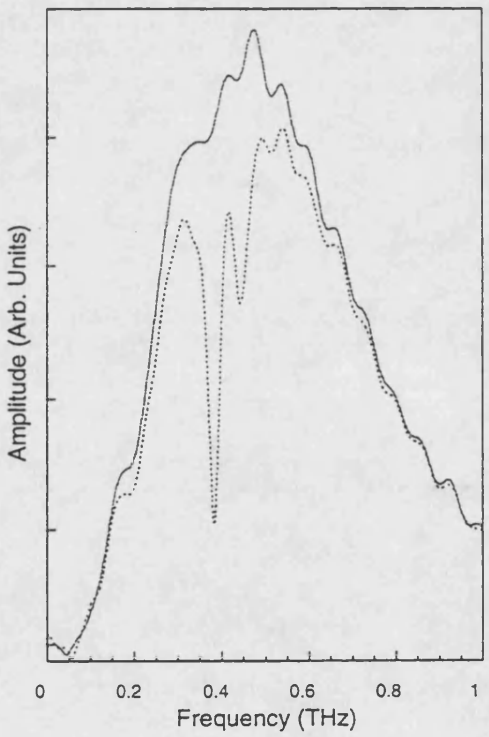

Figure 5.4: Transmitted spectra with gate biases of -0.5 V (solid curve) and +0.9 V (dashed curve) in a 1 T perpendicular magnetic field at T=5 K.

2D plasmon mode. There are no clear positive peaks above the noise in the difference spectrum.

The zero magnetic field plasmon oscillations were too weak to detect without modulation techniques. However, a field of 1 T was sufficient to shift the plasmon frequency to 0.46 THz, where the spectrometer sensitivity is doubled. This permitted direct detection and confirmation that the signal came from the forward bias state (maximum N_s) of the device. Figure 5.4 shows the Fourier transform of the directly detected signal in both forward and reverse bias. The lower frequency trough in figure 5.4 corresponds to cyclotron absorption and the higher frequency trough to the cyclotron shifted plasmon absorption. The reverse bias spectrum is similar to the transmission at 0 T, displaying only reflections and water vapour absorption lines. By applying an appropriate negative bias to the gate (~ -0.3 V), it was therefore possible to fully deplete the 2DEG of carriers or fix the carrier density at a selected level below the maximum.

The first calculation of two dimensional plasmon dispersion was performed by Stern[20] within the random phase approximation. In the long wavelength limit and neglecting retardation the dispersion is given by

$$\omega_{2Dp}^2 = \frac{N_s e^2}{2\varepsilon_0 \bar{\varepsilon} m^*} k_p \qquad (5.1)$$

Here ω_{2Dp} is the 2D plasmon angular frequency, k_p the plasmon wave vector in the plane of the 2DEG, $\bar{\varepsilon}$ is an effective dielectric constant which includes the screening effects of adjacent layers. This description assumes that only one subband is occupied[4] which has been experimentally verified for our sample by SdH

measurements. The dispersion relation of equation 5.1 apparently intersects the light line, $\omega = \bar{\varepsilon}^{-1/2} ck$, at

$$k_p = \frac{N_s e^2}{2\varepsilon_0 \bar{\varepsilon}^2 m^* c^2} \qquad (5.2)$$

Stern[20] showed that when retardation effects are taken into account, the plasmon dispersion curve and the light line never intersect. Thus no frequency exists at which the plasmon wave vector is equal to that of freely propagating radiation and consequently a 2D plasmon cannot couple directly to light.

To overcome this lack of coupling a method of changing the wavevector of free space radiation is required so as to match the plasmon dispersion. To this end, prisms[21] and, more commonly, metallic grating couplers[12] have been employed. The metal strips of the grating are perpendicular to the incident field, which has a uniform E_x component only. Screening of the incident field by the strips results in near field spatial modulation of the wavefront. Fourier components with wavevector $k_x n$ can couple with two dimensional plasmons if they satisfy the dispersion relation and $k_x = n\pi/a$, where a is the grating periodicity and n an integer. The electric field component perpendicular to the surface (E_z) in the near field can also be important for intersubband excitation, although these energies are not experimentally accessible to the present THz beam. The electric field of the n_{th} Fourier components decay as $e^{-nk_x z}$ from the surface of the grating for $k_x >> \omega/c$ thus the distance of the 2DEG from the grating, d, should be small compared with the periodicity ($dn/a < 0.1$) for the maximum strength of higher frequency components. For this sample d = 70 nm resulting in electric fields at the 2DEG 95% and 90 % of their values at the grating for the n = 1 and n = 2 Fourier components respectively. An effective dielectric constant $\bar{\varepsilon}$ allows for the presence both of different media on either side of the 2DEG and of a metallic structure, the grating coupler, in close proximity to the plasmon excitation. The electric field of the plasmon is screened by the grating and thus influences the plasmon frequency. For periodic grating structures no simple algebraic expression exists but $\bar{\varepsilon}$ has been calculated for the cases of a continuous,

perfectly conducting gate[22] ($\bar{\varepsilon}_{screened}$, equation 5.3) and for no surface metallisation[23] ($\bar{\varepsilon}_{unscreened}$, equation 5.4).

$$\bar{\varepsilon}_{screened} = \frac{\varepsilon_1 + \varepsilon_2 \coth\left(k_x^n d\right)}{2} \qquad (5.3)$$

$$\bar{\varepsilon}_{unscreened} = \frac{\varepsilon_1 + \varepsilon_2 \tanh\left(k_x^n d\right)}{2} \qquad (5.4)$$

In equations 5.3 and 5.4, $\varepsilon_1 = 11.7$ is the relative dielectric constant of the AlGaAs which separates the 2DEG from the gate and $\varepsilon_2 = 12.4$ is that of the GaAs on the other side of the 2DEG. The two expressions predict plasmon frequencies of 0.10 THz and 0.43 THz respectively for our sample. Equation 5.3 is commonly used to predict plasmon frequencies of grating coupled structures with semitransparent gates whereas equation 5.4 is applicable to observations without a grating, e.g. prism coupling and Raman spectroscopy. Only half the surface is covered by the metal grating so that one expects the 2D plasmon frequency of this system to be between the screened and exposed limits of equations 5.3 and 5.4. The exact value is complicated by the coincidence of the periodic screening of the grating and the spatial period of the plasmon. This results in a splitting of the plasmon into a high and low frequency mode, with standing charge density oscillations symmetric and antisymmetric about the centre of the grating apertures respectively[24]. These splittings appear as gaps in the dispersion at multiples of the grating wavevector but the upper frequency mode is only weakly radiative and not always observed. The difference in frequency reflects the relative grating effectiveness in screening electric fields beneath the metal. These splittings have been experimentally observed in the 2D plasmon dispersion of grating covered samples by Raman spectroscopy, which is not confined to the wavevectors of the grating[25]. Although rigorous models utilising scattering matrix formalisms have been developed[26] no simple formula exists to calculate the frequencies of the 2D plasmons. Hence we have not attempted to predict the frequencies in our sample. Models which use the Fourier expansion of conductivity terms to describe the gratings FIR properties also exist[27]. However these

can only cope with weak modulations of the conductivity, as opposed to the extremes of a real grating, and fail to predict any splitting of the 2D plasmon mode with a grating aspect ratio of 0.5 [28].

5.2.2 Carrier Density Dependence

Figure 5.5 shows typical plots of differential THz transmission at various carrier densities. The trace consists of an initial single cycle like transient followed by oscillations which decay with time. Up to 4 oscillations are visible enabling the determination of their frequencies with reasonable accuracy. Although the oscillations continue beyond 18 ps it was necessary to terminate the trace here due to a large temporal reflection. The inset in figure 5.5 shows the trace of the transmitted THz transient. The temporal reflection, approximately 10 ps after the initial transient, is much weaker in this trace. This is because the process of carrier density modulation causes the magnitude of the reflection to be raised to the power of the number of passes through the 2DEG such that:

$$E_T = E_0 t_{2DEG} \qquad (5.5)$$

$$E_R = E_0 \left(\frac{1-n}{1+n}\right)^2 t_{2DEG}{}^3 \qquad (5.6)$$

where E_0, E_T and E_R are the electric fields transmitted through the sample only, through the sample and 2DEG and through sample and 2DEG on reflection respectively. The amplitude transmittance of the 2DEG is t_{2DEG} and n is the refractive index of the substrate. The low frequency of the 2D plasmon prevents the time windowing of the reflection as it would leave only one and a half oscillations from which to determine the frequency, reducing the spectral resolution close to the frequency of the 2D plasmons themselves. The Fourier transforms (FTs) of the traces in figure 5.5 are shown in figure 5.6. The time domain traces were Hanning windowed to reduce spurious structure added to the FT by the necessary truncation of

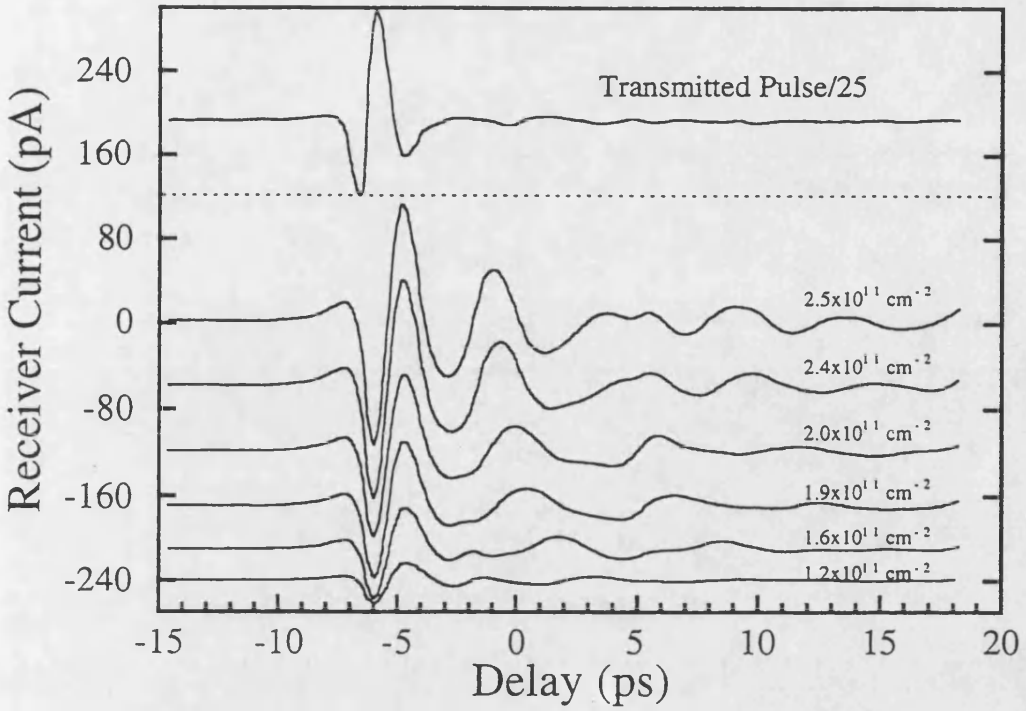

Figure 5.5: Differential THz transmission through A1690 at various carrier densities. The traces have been offset to aid clarity. The receiver current produced by the transmitted transient is also shown.

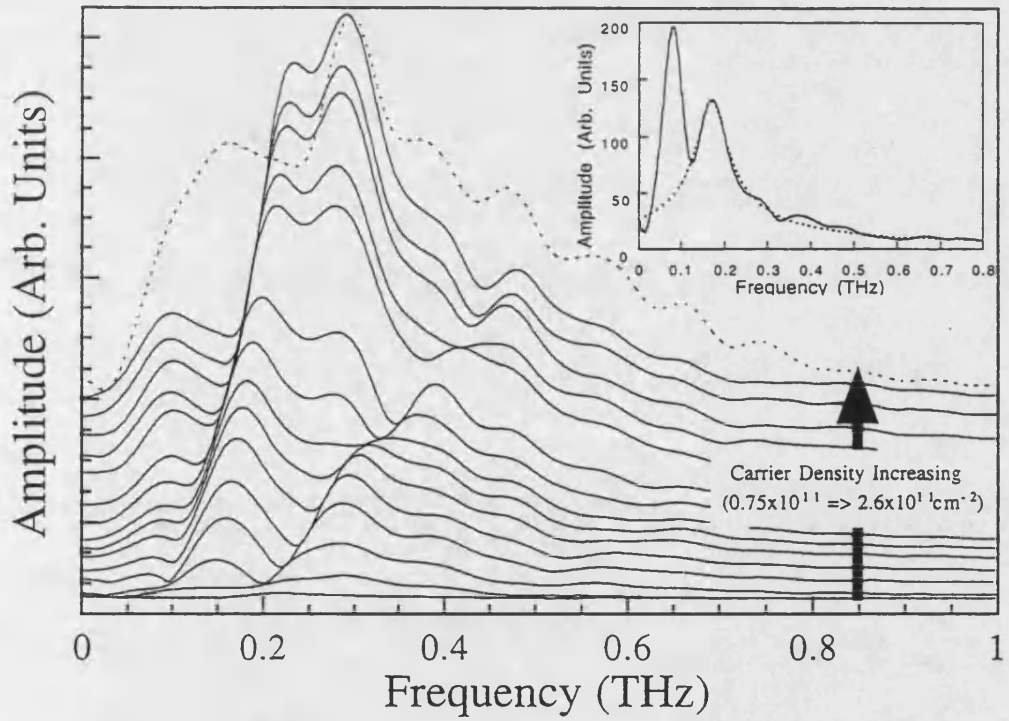

Figure 5.6: Fourier transforms of the time domain data (figure 5.5), offset to aid clarity (solid curves). The dashed curve shows similar measurements made without the grating coupler in place. Inset is shown a typical Fourier transform of the time domain data (N_s ~ 1.9×10^{11} cm^{-2}), divided by the transmitted THz spectrum to remove instrumental effects (solid curve). The dashed curve is a fit of equation 4.6 to the peak associated with the fundamental 2D plasmon.

the traces. This windowing did not significantly affect the linewidth of peaks in the FT. The dotted line at the top of figure 5.6 shows the differential transmission through A1690 under the same conditions but with a semitransparent NiCr gate instead of a grating coupler in place and is used as a reference to identify common features. Peaks of the grating coupled spectra which do not move with changing bias are similar to those of the dotted reference line and arise from temporal reflections and an unidentified resonance at ~ 0.29 THz. The two peaks which do move with bias are identified as the fundamental and first harmonic modes of the 2D plasmon. The frequencies of these modes are shown as a function of carrier density in figure 5.7. Fits to the data are also shown, assuming the dispersion given by equation 5.1 along with predicted dispersions for the fully screened (equation 5.3) and unscreened (equation 5.4) cases. Both fundamental and harmonic frequencies lie in between the two extremes of screening. The fits give values of 23.1 and 15.1 for $\bar{\varepsilon}$ of the fundamental and first harmonic modes respectively. The fit overestimates the frequency at high carrier densities and under estimates at low carrier densities. This probably reflects experimental errors, although charged impurity[29] and interface roughness[30] scattering can lower the plasmon frequency at lower densities.

Equation 4.6 was fitted to the peaks of the plasmon spectra (inset figure 5.6) to obtain the effective dephasing times, shown in Figure 5.8. From ~ 7 ps at $N_s \sim 1.2\times10^{11}$ cm^{-2}, τ^* decreases to ~ 5 ps at 2.0×10^{11} cm^{-2} before rising to ~ 6 ps at 2.6×10^{11} cm^{-2}. The interference fringes and unidentified resonance in figure 5.6 make determination of the 2D plasmon τ^* difficult and are responsible for the large error bars at high and low carrier densities. The measured τ^* cannot be corrected for the finite carrier density as the conductivity of the grating gate is unknown. A fit of the effective dephasing time, $\tau^* = \tau_{deph}/(1+\omega_{ps}\tau_{deph})$ (section 4.2), to the data is shown in figure 5.8 assuming a constant τ_{deph}. The fit crosses the majority of the error bars and gives values of ~ 8.5±1.6 ps and ~ 0.246 Hz cm^2 for the true dephasing time, τ_{deph}, and ω_{ps}/N_s respectively. The estimated value of ω_{ps}/N_s is close to the value of 0.320 Hz cm^2 expected for a surface with no gate. The dip at $N_s \sim 2.0\times10^{11}$ cm^{-2} represents a marked deviation from the fit but its origin is unknown. However, similar dependencies in inversion layers of Si MOSFET's have been observed in

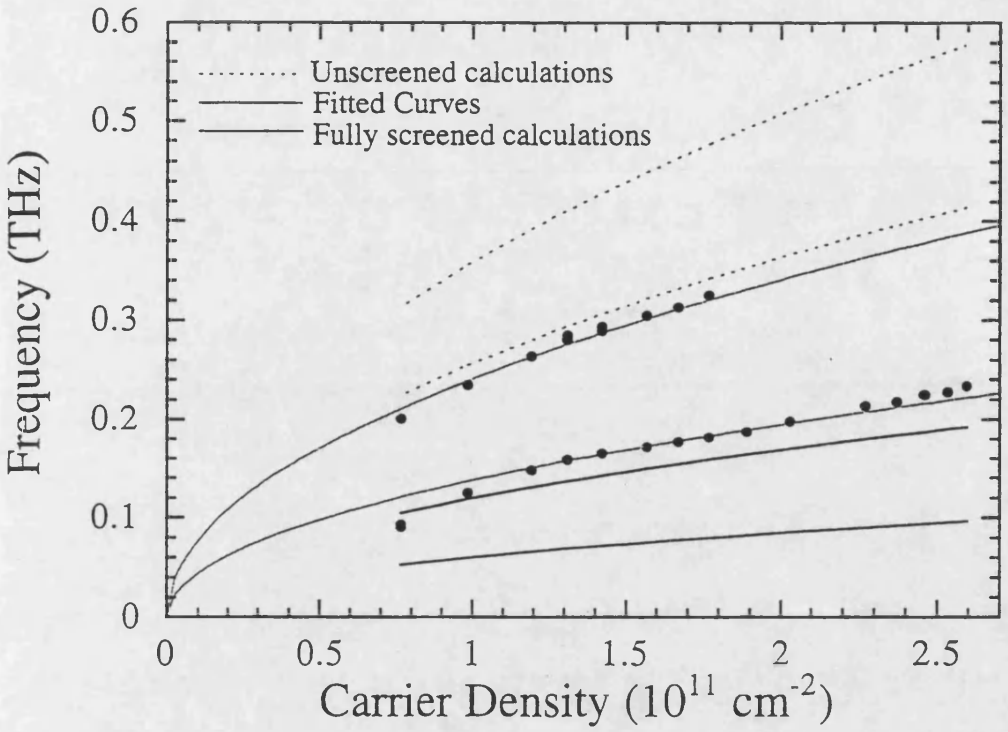

Figure 5.7: Peak positions from figure 5.6, which move with bias (points). Fits to the data assuming the plasmon dispersion given by equation 5.1 together with predicted dispersions assuming a bare and fully metalised surface are also shown (lines).

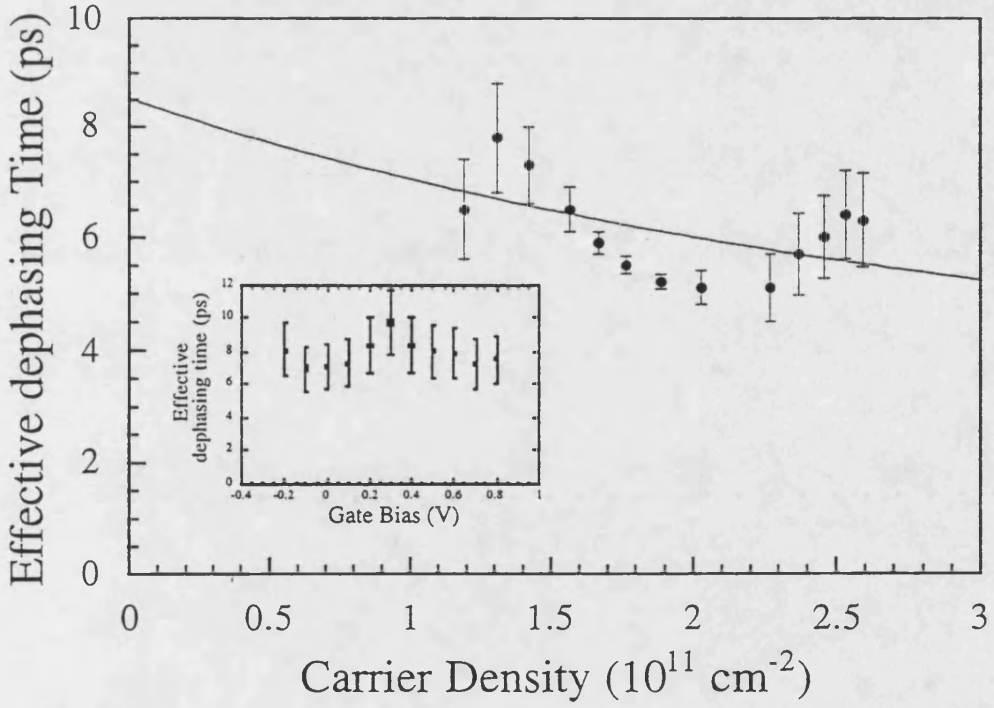

Figure 5.8: Plasmon effective dephasing times of A1690 as a function of carrier density obtained from fits to the data. The line shows a fit to the data assuming a constant dephasing time and taking the finite number of carriers into account. The inset shows cyclotron effective dephasing times of a second sample from the same wafer with a gate but no grating coupler

CR[31] and 2D plasmon[12] experiments and discussed at length by Gold[30]. Landau damping, the decay of plasmons into electron hole excitations, may also be able to explain some of the dependence[32]. The inset of figure 5.8 shows fitted τ^* from CR differential THz transmission of a different sample of A1690 at B = 2 T with a semitransparent NiCr gate instead of a grating coupler. The dependence of carrier density with gate bias was not determined for this sample but the maximum ($\sim 6\times10^{11}$ cm^{-2}) might be expected to correspond 0.8 V gate bias with minimum carrier density at ~ -0.3 V. It is difficult to establish whether the trends in the main figure are repeated inset due to the error bars, but τ^* inset appears fairly constant. Thus the trends in the main figure 5.8 may be confined to the plasmon/grating system.

5.2.3 Magnetic Field Dependence

In a perpendicular magnetic field the plasmon resonance is shifted in frequency becoming the so-called plasma-shifted cyclotron resonance or magnetoplasmon (MP). The effect of a magnetic field, in the range 0 T to 1 T, figure 5.9 is shown. A general increase in frequency with magnetic field is evident as is a beating between two closely spaced frequencies at higher fields. An approximate doubling in the signal strength of the differential transmission, between 0 T and 1 T, is also apparent. This increase is confined to the cyclotron resonance and magnetoplasmon. The unidentified resonance is apparently unaffected by the application of a moderate magnetic field. If the full magnetoconductivity tensor is substituted into the expression for the dielectric constant of the 2DEG, poles, corresponding to the plasmon frequencies, occur at[33]

$$\omega_{mp}^2 = \omega_c^2 + \omega_p^2 \qquad (5.9)$$

where ω_{mp}, ω_c and ω_p are the MP, cyclotron resonance and zero field plasmon frequencies respectively. Experimentally the MP evolves from the 2D plasmon's zero field value and asymptotically approaches ω_c with increasing field in reasonable

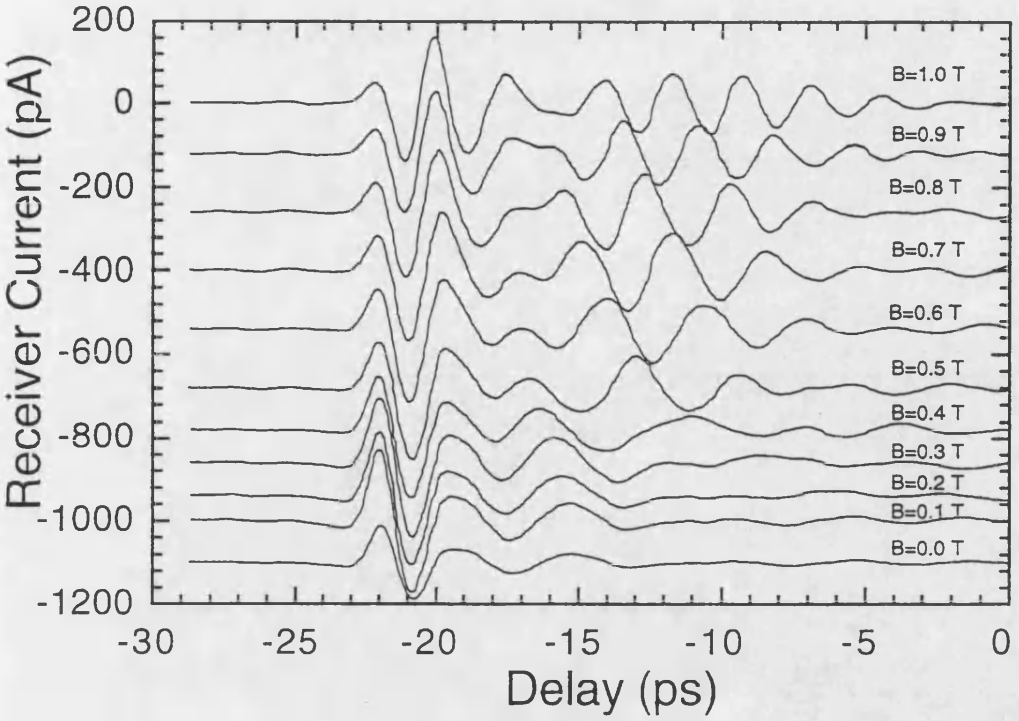

Figure 5.9: Differential THz transmission through A1690 at various magnetic fields. The traces have been offset with respect to each other for the sakes of clarity.

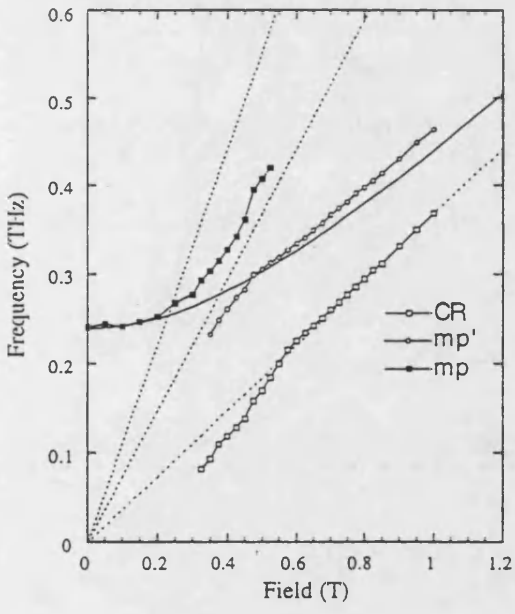

Figure 5.10: Plasma frequencies in A1690. Dashed curves show predicted cyclotron harmonics, solid curve shows predicted position magnetoplasmon frequencies

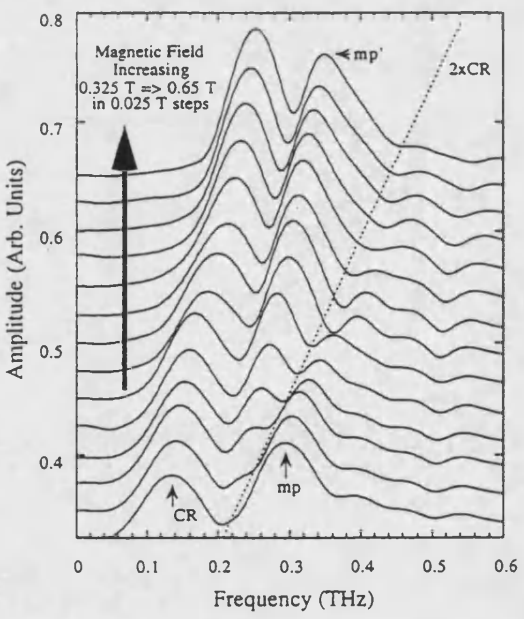

Figure 5.11: Fourier transforms of the time domain data of figure 5.9. The dashed line shows the predicted position of the cyclotron resonance first harmonic

agreement with the Drude derived equation 5.9 [13]. The position of the resonance obtained by Fourier transforming the Hanning windowed time domain traces is shown in figure 5.10, together with predictions of equation 5.9. The FTs have been divided by the FT of the transmitted THz pulse to remove instrumental effects. The lowest line is the CR peak position which increases in frequency with magnetic field as does the MP peak. A 0.25 THz splitting of the MP is visible at ~ 0.4 T. Figure 5.11 shows a close up of the FT in this region. From the spectra it can be seen that the lower frequency mode (mp') gradually gains in oscillator strength at the expense of the higher frequency mode (mp) until it becomes dominant at ~ 0.425 T (figure 5.12a). We see here the interaction of the MP with the CR harmonic ($2\omega_c$), known as a Bernstein mode[34]. Although such transitions are normally forbidden a breaking of the system's symmetry by the grating coupler can relax the $\Delta n = \pm 1$ selection rule for Landau level transitions. If the MP resonant frequency is close to the frequency of a Bernstein mode, the dynamic spatial modulation of the plasma wave disturbs the lateral potential in the 2DEG allowing transitions with $\Delta n = \pm 2,3,....$ This coupling is seen in the anti-crossing behaviour of the MPs near the CR first harmonic ($\omega_p(B) \sim (2\omega_c)$) [14]. The calculated $2\omega_c$ frequency, shown by the dashed line in figure 5.11, assumes an effective mass of 0.076 and the MP frequency is calculated from its zero field value. The nonlocal corrections responsible for the coupling, in Ando's interpretation[35], are proportional to the parameter $(k_p v_f/\omega_c)^2$, where v_f is the Fermi velocity. Assuming an effective mass of 0.076 m_0, this yields a value for the parameter of 0.023 at 0.425 T for this system. Although the splitting increases with $(k_p v_f/\omega_c)^2$ [14], the full field dependence is not a simple function of this parameter and the reader is referred to the original work for greater detail. For a more quantitative analysis of the splitting one may define a figure of merit measured at minimum separation between the two frequencies[4,34]:

$$\frac{\Delta\omega_m^2}{\omega_{mp}^2} = \frac{2\left(\omega_{mp'}^2 - \omega_{mp}^2\right)}{\left(\omega_{mp'}^2 + \omega_{mp}^2\right)} \qquad (5.10)$$

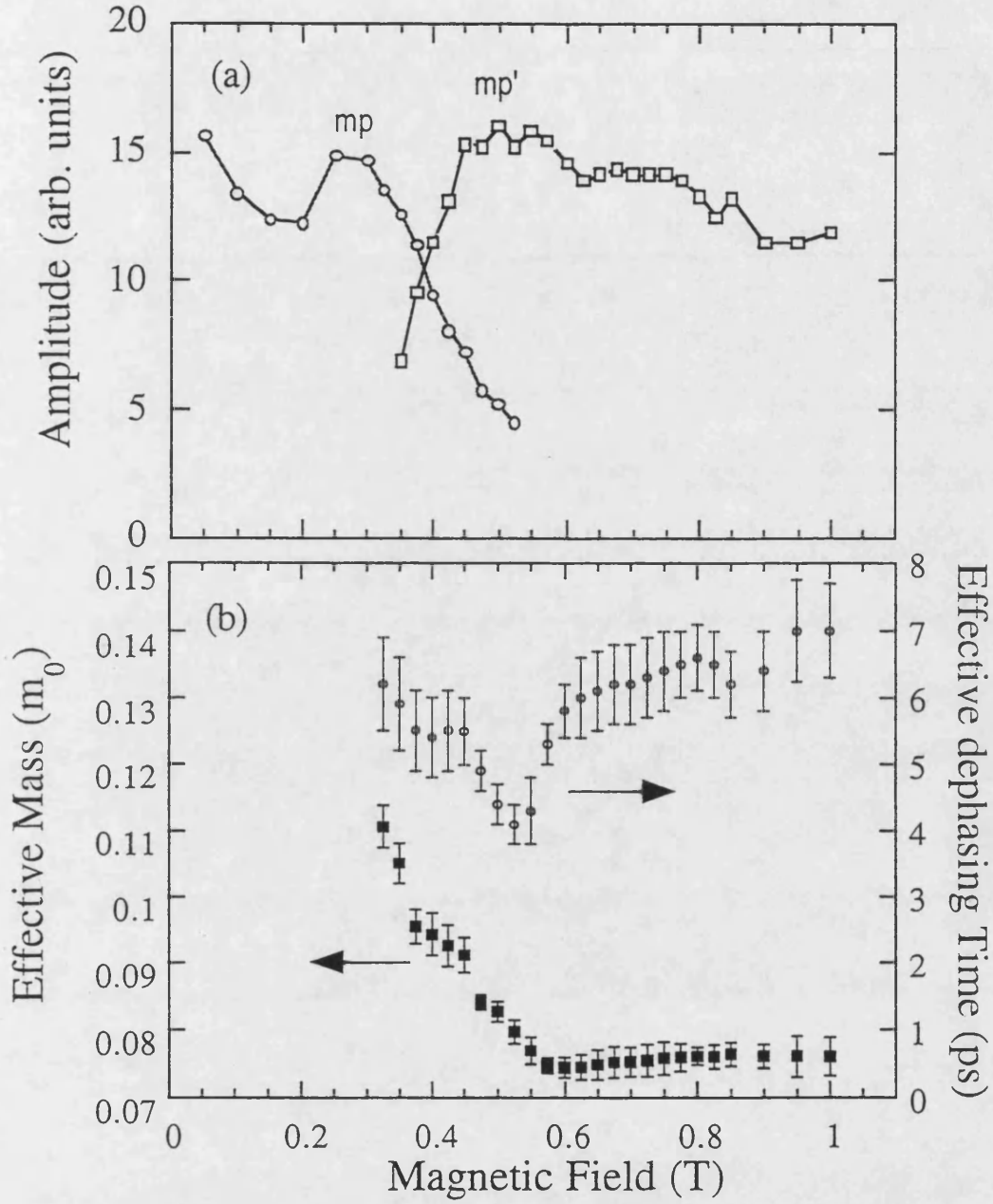

Figure 5.12: (a) Peak amplitude of the two modes of the Bernstein splitting (mp and mp') as a function of magnetic field, the lines are a guide to the eye. (b) The effective dephasing time and effective mass determined by fits to the data.

From figure 5.10 a value of $\Delta\omega_{mp}^2/\omega_{mp}^2 = 0.223$ at 0.425 T, the minimum separation between the two peaks, is obtained. In general, the agreement between equation 5.9 and experiment is good (with the exception of the Bernstein splitting) although the values tend to be underestimated at higher fields. An anomalous kink in the CR is apparent close to 0.5 T in figure 5.10. This is accompanied by a broadening of the CR peak just visible in figure 5.11. The derived effective mass (assuming $\omega_c = eB/m^*$) and effective dephasing time, determined by fitting equation 4.6 to the peaks of the figure 11, is plotted against magnetic field in figure 5.12b. At higher fields τ^* is fairly constant at ~ 6±0.9 ps but at ~ 0.6 T there is the beginning of a downward trend with decreasing field, τ^* has a minimum value of ~ 4 ps at ~ 0.55 T and rises with further decreasing field, approaching the high field value. Below 0.325 T the CR peak was not reliably resolved. The effective mass has a constant high field value of ~ 0.076 m_0, but increases with decreasing field near the field for minimum τ^* reaching ~ 0.110 m_0 at 0.325 T. Comparing figures 5.12a and 5.12b, it can be seen that the extremities of the Bernstein splitting almost coincide with the maximum of m^* and minimum of τ^* and also appear to mark the boundaries where these two anomalies overlap. If both anomalies were to be interpreted as an unresolved splitting of the CR then the field of minimum τ^* would appear to define the maximum of the splitting and a crossover point of the different modes. The high field mode corresponds to the classical CR and yields an in-plane effective mass of 0.076±0.001 m_0 but the low field, low frequency mode remains unidentified. Whether the frequency reaches 0 THz before 0 T or approaches the origin is unknown and out of the range of the spectrometer.

Broadening of the CR, similar to that seen here, accompanied by a splitting, has been observed in FIR transmission experiments on an AlGaAs/GaAs 2DEG in the presence of a lateral superlattice potential[36]. This was generated by applying a bias to a grid metal gate on the sample surface but the anomaly was not seen in samples from the same wafer without a grid gate[37]. Zhoa *et al.*[37] identified a correlation between the ratio of a/d, linked to the strength of plasmon absorption, and the magnitude of the CR broadening and splitting. In that work a/d ranged from 2.6

to 20 compared with 114 for this work, implying a greater splitting/broadening should be seen in our sample, although no definite splitting was observed. Further no such anomaly was observed at all by Bangert *et al.* [38] in similar FIR transmission measurements of a grating coupled 2DEG with a/d ~ 8.

Additionally, similar effective mass and linewidth anomalies to those in figure 5.12b have been observed previously by Schlesinger[39] in GaAs/AlGaAs 2DEGs without a grating. It was suggested that they are from an interaction with an unseen MP. Zhoa *et al.* interpreted their own and Schlesinger's results as a breakdown of Kohn's theorem[40] due to the periodic metal grating and defects in the heterostructure respectively. A depressed cyclotron frequency at fields below the anomaly was also seen by Zhoa *et al.*.

As a final possibility we consider anomalies in FIR transmission when the cyclotron diameter, D_c (see section 4.3), is equal to the period of the grating[41] but at the field of the anomaly (~ 0.5 T) D_c = 2 μm, 4 times less than the period. Comparative measurements without a grating coupler have not been made and thus it is uncertain whether the splitting is due to the presence of the grating or not. However, we believe it to be distinct from those observations of CR frequency and linewidth deviation which are linked to much lower filling factors and mobilities than in the present work[42].

5.3 Interband Measurements

The coherent interband excitation of the 2D plasmons was explored to complement the intraband investigations. Previously Vossebürger *et al.* have used 100 fs pulses of above bandgap radiation from a Ti:Sapphire laser to coherently excite 2D plasmons in an AlGaAs/GaAs heterostructure in the emission geometry[15]. They used a 3 μm period metal grating coupler without a continuous metal overlayer and observed oscillations at frequency of 0.5 THz. Ultrafast thermalisation and screening induced current surges were proposed as the excitation mechanisms

In this work a second sample was fabricated from A1690 with a 5 μm period grating coupler and unity mark space ratio. A shorter periodicity was chosen to shift

the 2D plasmon frequency to a more sensitive part of the spectrometer's response thus increasing the signal strength. This sample possessed no electrical contacts and was not chemically etched. The sample was investigated in the emission geometry and coherently excited with 70 fs pulses of above bandgap radiation from the Ti:Sapphire laser, horizontally polarised orthogonal to the grating coupler. The specular geometry introduces a slight asymmetry into the excitation profile with respect to the grating coupler such that the fields from counter propagating plasma oscillations do not cancel each other out[26]. To improve the signal to noise ratio the excitation beam was chopped with an acousto-optic modulator and synchronous detection used. Lateral modulation of the carrier density was expected as a result of illumination of the opaque grating in addition to the screening modulation. With constant illumination the 2DEG sheet carrier density is expected to be ~ 4.5×10^{11} cm^{-2} and the calculated frequencies for the screened and unscreened limits are then 0.21 THz and 0.68 THz respectively.

Figure 5.13 shows a typical trace with 450 mW excitation at 765 nm and a 1 mm focal spot size. The trace consists of a single cycle like transient followed by 8 oscillations, which decay with time. The initial transient is associated with the instantaneous creation of polarised photo-carriers (equation 2.2) and is followed by oscillations associated with coherent 2D plasmons. The plasma dephasing time is 6±0.6 ps, locating the source of the oscillations in the high mobility 2DEG and not from plasmons in the bulk. The inset of figure 5.13 is an FT of the time domain trace and shows the frequency to peak at 0.40 THz. Using equation 5.1 this gives $\bar{\varepsilon}$ ~ 12.4 for the 5 μm grid sample. The emission frequency and dephasing time were found to remain constant as a function of excitation energy and average power from 745 nm to 815 nm and from 450 mW to 13 mW. The FT peak magnitudes however increase linearly with power and excess energy above the bandgap over this range (figure 5.14). Below the bandgap no radiated transient is observed

The frequency of the 2D plasmon is not expected to be greatly influenced by the carrier density photoinjected into the accumulation layer, ~ 3×10^{9} cm^{-2}, as it is two orders of magnitude less than that of the 2DEG. The dephasing time displays no signs of screening by the photo-injected carriers.

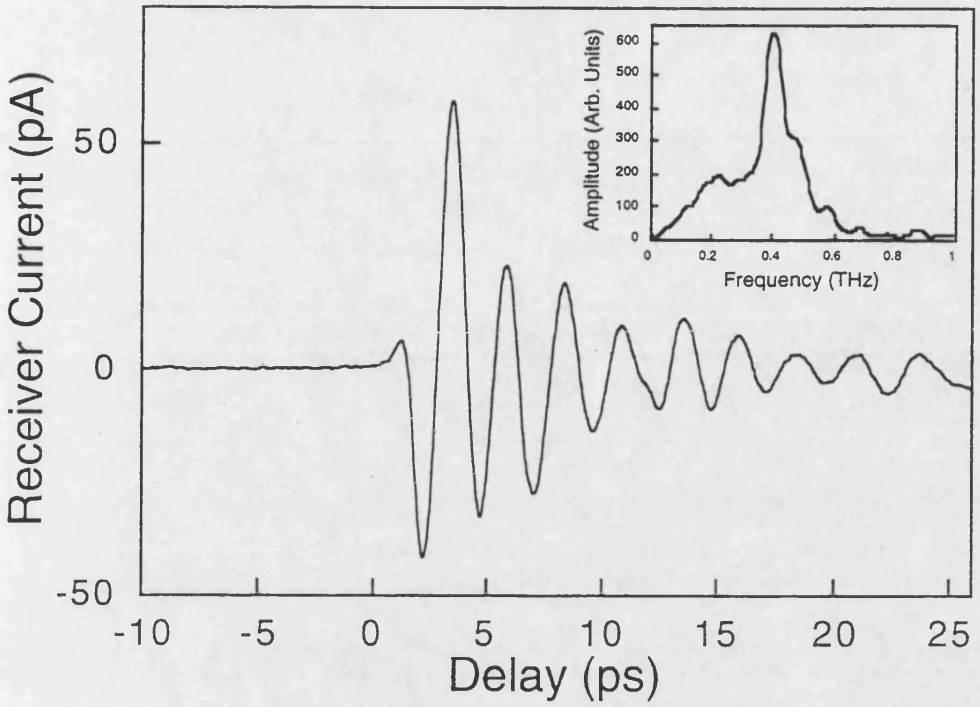

Figure 5.13: Time domain receiver current from A1690 following 450 mW excitation by a 70 fs, 765 nm laser pulse. The Fourier transform of the trace is shown in the inset.

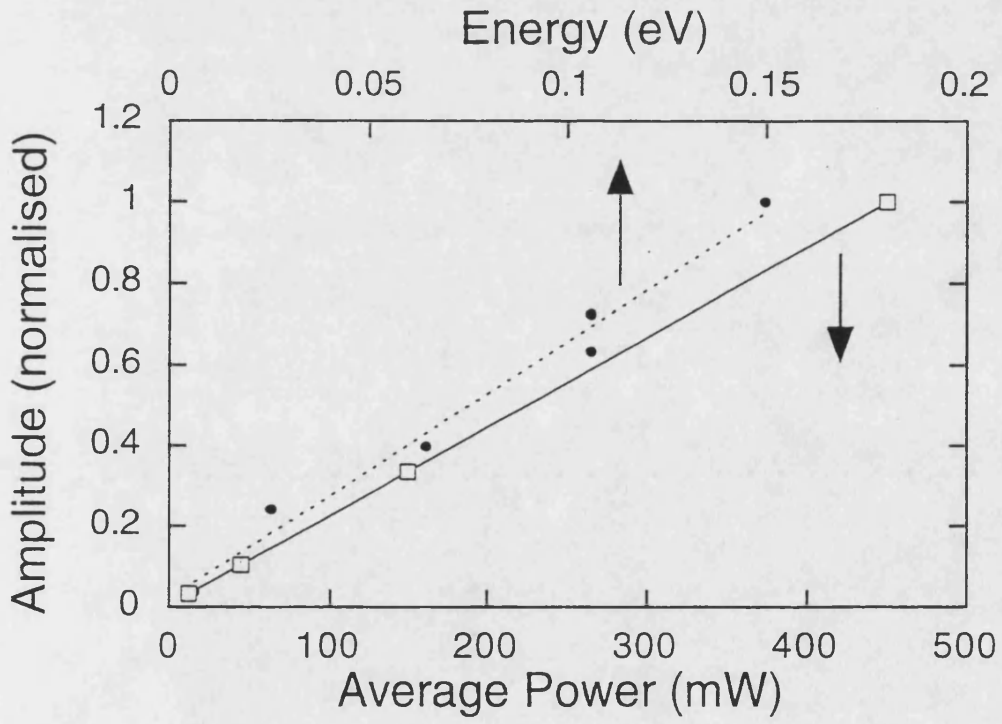

Figure 5.14: Fourier transform peak amplitudes as a function of laser power and excess energy above the bandgap.

The power of the radiation emitted from a coherent ensemble of dipoles is expected to depend quadratically on the number of co-operatively emitting dipoles (which is proportional to the number of excited radiative plasmons)[43] Hence the THz amplitude should exhibit a linear dependence on the pump power (superraddiance), as is indeed observed in the experiment. This is contrary to the saturation in amplitude observed by Vossebürger *et al.* [15] at nearly a fifth of the maximum power density used here and is not presently understood. However, the linear dependence of the amplitude on excess energy above the band gap is in agreement with their hypothesis that the oscillations are as a result of a rapid thermalisation of the 2DEG by the photo-injected carriers. This does not exclude the current surge hypothesis but would presumably require the number of photons absorbed to be proportional to the excess photon energy above the band gap.

5.4 Summary

Two dimensional plasmons have been studied in an AlGaAs/GaAs heterostructure as a function of carrier density and magnetic field and by inter as well as intra band excitation. The carrier density dependence revealed a frequency in agreement with the dispersion relation derived by Stern. The dephasing time dependence is similar to that seen in Si:MOSFET inversion layers[12,31], as a result of impurity scattering and interface roughness[30]. With the application of a magnetic field the fundamental magnetoplasmon and Bernstein splitting were resolved as was a unexplained broadening of the cyclotron resonance. Interband excitation displayed no signs of screening by the photo-injected carriers. The signal strength increases linearly with excess energy above the bandgap and can be explained either by rapid thermalisation of the 2DEG or current surges by the photo-injected carriers. The latter hypothesis requires the number of photons absorbed to be proportional to the excess photon energy above the band gap.

References

(1) T. Ando, A. B. Fowler and F. Stern, Rev. Mod. Phys. **54**, 437 (1982); D. Heitmann in "Physics of Nanostructures", Ed. J. H. Davies and A. R. Long IOP publishing Ltd., Bristol, England (1992), p 242; R. J. Nicholas in "Handbook on Semiconductors", completely revised edition Ed. M. Balkanski, Elsevier, Amsterdam (1994), p.385

(2) E. Batke, D. Heitmann and C. W. Tu, Phys Rev **B 34**, 6951 (1986)

(3) T. N. Theis, J. P. Kotthaus and J. P. Stiles, Solid State Commun. **35**, 875 (1980)

(4) D. Heitmann, Surf. Sci. **170**, 332 (1986)

(5) A. V. Chaplik Surf. Sci. **Rep 5**, 289 (1985)

(6) P. Bakshi and K. Kempa, Superlattices and Microstructures **17**, 363 (1995)

(7) K. Hirakawa, K. Yamanaka, M. Grayson and D. C. Tsui, Appl. Phys. Lett. **67**, 2326 (1995)

(8) Michael Dyakonov and Michael Shur, Phys. Rev. **B 71**, 2465 (1993)

(9) Michael Dyakonov and Michael Shur, Appl. Phys. Lett. **67**, 1137 (1995)

(10) Michael Dyakonov and Michael Shur, IEEE TRANSACTIONS ON ELECTRON DEVICES **43**, 1640 (1996)

(11) P. Marks, New Scientist **2124**, 34 (1998)

(12) S. J. Allen, Jr., D. C. Tsui and R. A. Logan, Phys. Rev. Lett. **38**, 980 (1977)

(13) T. N. Theis, J. P. Kotthaus and P. J. Stiles, Solid State Commun. **24**, 273 (1977)

(14) E. Batke, D. Heitmann, J. P. Kotthaus and K. Ploog, Phys. Rev. Lett. **54**, 2367 (1985)

(15) M. Vossebürger, H. G. Roskos, F. Wolter, C. Waschke, H. Kurz, K. Hirakawa and K. Yamanaka, J. Opt. Soc. Am. **B 13**, 1045 (1996)

(16) A1690 grown and characterized at Cavendish Laboratory

(17) H. L. Störmer, R. Dingle, A. C. Gossard, W. Wiegmann and M. D. Sturge Solid State Commun. **29**, 705 (1979)

(18) P. Uhd Jepsen, R. H. Jacobsen and S. R. Keiding, J. Opt. Soc. Am. **B 13**, 2424 (1996)

(19) N. Katzenellenbogen and D. Grischkowsky, Appl. Phys. Lett. **58**, 222 (1991)

(20) F. Stern, Phys. Rev. Lett. **18**, 546 (1967)

(21) "Introduction to surface and superlattice excitations", M. G. Cottam and D. R. Tilley Cambridge University Press, Cambridge (1989), p. 218

(22) A. V. Chaplik, Soviet Phys. JETP **35**, 395 (1972)

(23) N. Okisu, Y. Sambe and T. Kobayashi, Appl. Phys. Lett. **48**, 776 (1986)

(24) R. E. Tyson, D. E. Bangert and H. P. Hughes, Appl. Phys. **76**, 5909 (1994)

(25) L. C. O' Súilleabháin, H. P. Hughes, D. Bangert, A. C. Churchill, M. P. Grimshaw D. A. Ritchie and G. A. C. Jones, Phys. Rev. **B50**, 14161 (1994)

(26) C. D. Ager and H. P. Hughes, Phys. Rev. **B 44**, 13452 (1991); O. R. Matov, O. V. Polischuk and V. V. Popov, International Journal of Infrared and Millimeter Waves **14**, 1455 (1993); R. E. Tyson, D. E. Bangert and H. P. Hughes, Appl. Phys. Lett. **76**, 5909 (1994)

(27) see for example M. V. Krasheninninkov and A. V. Chaplik, Sov. Phys. JETP **61**, 75 (1985)

(28) C.D. Ager, R. J. Wilkinson and H. P. Hughes, Appl. Phys. **71**, 1322 (1991)

(29) G. F. Giuliani and J. J. Quinn, Phys Rev **B 29**, 2321 (1984)

(30) A. Gold, Phys. Rev. **B 32**, 4014 (1985)

(31) G. Abstreiter, J. P. Kotthaus, J. F. Koch and G. Dorda, Phys Rev **B 14**, 2480 (1976)

(32) A. Gold, Phys. Rev. **B 41**, 3608 (1990)

(33) T. N. Theis, Surf. Sci. **98**, 515 (1980)

(34) I. B. Bernstein, Phys Rev. **109**, 10 (1958)

(35) T. Ando, Solid State Commun. **27**, 895 (1978)

(36) C. T. Liu, K. Nakamura, D. C. Tsui, K. Ismail, D. A. Antoniadis and H. I. Smith, Surf. Sci. **228**, 527, (1990)

(37) Y. Zhao, D. C. Tsui, M. B. Santos, M. Shayegan, R. A. Ghanbari, D. A. Antoniadis and H. I. Smith, Phys Rev **B 51**, 13174 (1995)

(38) D. E. Bangert, R. J. Stuart, H. P. Hughes, D. A. Ritchies and J. E. F. Frost, Semicond. Sci. Technol. **11**, 352 (1996)

(39) Z. Sclesinger, S. J. Allen, J. C. M Hwang, P. M. Platzman and N. Tzoar, Phys. Rev. **B 30** 435 (1984)

(40) Walter Kohn, Phys Rev. **123**, 1242 (1961)

(41) J. P. Kotthaus in "Granular Nanoelectronics", Ed. D. K. Ferry ,Plenum Press, New York (1991), p. 85

(42) J.-P. Cheng and B. D. McCombe, Phys. Rev. **B 44**, 3070 (1991)

(43) R. H. Dicke, Phys. Rev. **93**, 99 (1953)

(44) Self consistent Poisson/Schrödinger band calculations performed by Dr. Steve Andrews University of Bath

6 Conclusions

Various aspects of THz time domain spectroscopy have been investigated. The body of this work has dealt with the spectrometer itself and impulsive excitation of various intraband modes of semiconductor charge carriers by THz transients.

An increase in spectrometer sensitivity of two orders of magnitude (1995-2000) has been described. Investigations have shown that the strength of THz transients emitted from edge illuminated striplines on semi insulating GaAs depend strongly on the polarisation of the excitation beam, with contrast between orthogonal polarisations increasing with illuminated intensity. Silicon-on-sapphire dipole receivers also show a strong dependence of the sensitivity on the excitation polarisation. An explanation based on the initial distribution of photocarriers has been proposed in both cases. The excitation of transmitters with pointed anodes results in an increase in amplitude, but at the expense of bandwidth. However, the use of appropriate excitation beam polarisation together with a distributed line focus of the transmitter allows the creation of THz beams with up to 30 μW of power without any reduction in spectral bandwidth.

The bandwidths of a coplanar stripline (CPS) transmitter and dipole receiver have been characterised with a single chip dual pulse source THz interferometer. Pairs of THz transients were generated from a single coplanar stripline emitter, their separation being determined by the spacing of the near infrared femtosecond laser pulses used to excite the transmitter. A new type of transmitter was developed for this purpose which was less susceptible to crosstalk between the pulses compared with the common CPS design. Average THz powers of ~ 10 μW were measured compared with 30 nW previously reported for a CPS interferometer. The radiated

spectrum was found to overlap with the receiver response although their spectra peaks were separated by ~ 0.8 THz.

The ability to predict far infrared optical constants from transport measurements has been investigated. The complex electric field transmission of several doped GaAs epilayers has been measured at frequencies from ~ 0.2 THz to ~ 3 THz and the optical Hall effect measured on one sample between 0.5 THz to 1.1 THz using the technique of time domain spectroscopy. The Drude model can be used to calculate the complex amplitude transmission with good accuracy for carrier densities up to at least 10^{18} cm^{-3}. In the case of p-type epilayers, the deduced carrier densities and mobilities are in good agreement with values obtained from transport measurements. For n-type samples, the electron density agrees well with transport data, but mobilities are slightly smaller than obtained from Hall data. For the one n-type sample studied using the optical Hall effect, the mobility data underestimates the transport data by ~ 20% although the electron density is in good agreement.

Cyclotron absorption measurements has been made in AlGaAs/GaAs and Si/SiGe quantum wells as a function of magnetic field, carrier density and temperature. The electron dephasing time in the GaAs quantum wells decreases with decreasing carrier density and is thought to be due to a reduction in its ability to screen scattering by remote impurity potentials. This has been determined to be the primary scattering mechanism at low temperatures. The cyclotron resonance data from the Si/SiGe quantum well sample approaches a non-zero offset at zero field and displays an extended scattering time when compared with transport data. The results may be explained by the existence of antidot like states. In addition the dual pulse source has been used to impulsively drive and coherently control cyclotron oscillations in a two dimensional electron gas (2DEG). This is believed to be the first demonstration of coherent control of an intraband process.

Finally two dimensional plasmons have been studied in an AlGaAs/GaAs heterostructure as a function of carrier density and magnetic field and by inter as well as intra band excitation. The carrier density dependence revealed a frequency in agreement with the dispersion relation derived by Stern. The dephasing time dependence is similar to that seen in Si:MOSFET inversion layers, as a result of

impurity scattering and interface roughness. With the application of a magnetic field the fundamental magnetoplasmon and Bernstein splitting were resolved as was a unexplained broadening of the cyclotron resonance. Interband excitation displayed no signs of screening by the photo-injected carriers. The signal strength increases linearly with excess energy above the bandgap and can be explained either by rapid thermalisation of the 2DEG or current surges by the photo-injected carriers. The latter hypothesis requires the number of photons absorbed to be proportional to the excess photon energy above the band gap.

A number of extensions to this work are proposed: It is believed that considerably better performance of the THz interferometer would be obtained by using the 4 electrode transmitter in conjunction with a faster detector and rapidly scanned delay. More detailed THz Hall studies need to be performed on the remaining n-type samples and to determine if the electron mobility becomes sensitive to the frequency of the incident radiation above 1.1 THz. Considering the Si/SiGe cyclotron resonance studies; improved low field measurements using low frequency antenna pairs and a gated device need to be performed to allow further understanding. The two dimensional plasmon investigations require complementary cyclotron resonance measurements on 2DEGs, without grating couplers, as functions of carrier density and magnetic field. Additionally higher plasmon frequencies (higher carrier concentrations or shorter period gratings) and samples without unidentified resonances are sought to increase the signal to noise ratio of these measurements. Finally the absorption coefficient as a function of excitation frequency needs to be determined to identify the driving mechanism behind the interband excited plasmons.